European Organization for Nuclear Research, Geneva, Switzerland

University of Hamburg, Germany

Diploma Thesis

Tune Resonance Phenomena in the SPS and related Machine Protection

Tobias Baer

supervised by:

Dr. Jörg Wenninger (CERN, Geneva)
Prof. Dr. Eckhard Elsen (University of Hamburg and DESY, Hamburg)

July 29, 2010

Abstract

The Super Proton Synchrotron (SPS) at CERN, with a peak energy of 450 GeV, is at the top of the LHC preaccelerator complex. SPS is at present the accelerator with the largest stored beam energy worldwide of up to 2.5 MJ.

In 2008, a fast equipment failure led to an uncontrolled loss of a high intensity beam at an integer tune resonance, which resulted in major damage of a main dipole. Experimental studies and simulations provide clear understanding of the beam dynamics at different SPS tune resonances, that can lead to a complete beam loss in as little as 3 turns.

Dedicated experiments of fast failures of the main power converters reveal that the current interlock systems are much too slow for an adequate machine protection.

A new position interlock system, which is currently in the commissioning phase, will counteract the vulnerability of the SPS.

Zusammenfassung

Das Super Proton Synchrotron (SPS) am CERN mit einer Spitzenenergie von 450 GeV ist der größte LHC Vorbeschleuniger. Zur Zeit ist das SPS der Beschleuniger mit der größten gespeicherten Strahlenergie weltweit von bis zu 2.5 MJ.
2008 hat ein schneller Betriebsfehler zum unkontrollierten Verlust eines Hochintensitätsstrahls an einer Resonanz mit ganzzahligem Q-Wert geführt. Als Folge wurde ein Hauptdipolmagnet massiv beschädigt. Experimentelle Untersuchungen und Simulationen liefern ein klares Verständnis der Strahldynamik an verschiedenen optischen Resonanzen, die im SPS innerhalb von 3 Umläufen zu einem kompletten Strahlverlust führen können.
Experimente mit schnellen Fehlern der Hauptstromversorgung zeigen, dass die bestehenden Sicherheitssysteme viel zu langsam sind, um eine angemessene Maschinensicherheit zu gewährleisten.
Um die Anfälligkeit des SPS für die Folgen schneller Betriebsfehler zu unterbinden, wurde ein neues strahlpositionsbasiertes Sicherheitssystem entwickelt, das sich momentan in der Inbetriebnahmephase befindet.

Acknowledgments

This work was developed in close collaboration with many colleagues. I am very grateful for the help, advice and support of everybody who contributed to the project and made this work possible.

First and foremost, I wish to express my most sincere gratitude to my supervisor at CERN, Jörg Wenninger. He gave me the freedom and support to carry out own ideas and helped with many wise advices, suggestions and his incredible competence. His guidance and supervision was outstanding.

I extend my gratitude to my supervisor from the University of Hamburg, Eckhard Elsen. His comprehensive and thorough view led to especially valuable discussions, suggestions and feedback. I am particularly thankful for his support of my personal and professional development and the training opportunities he made possible. I cannot imagine a better constellation of supervision.

The person I spent most of my time at CERN with, is my office mate and friend Kajetan Fuchsberger. Many fundamental ideas came up during the uncountable discussions we had. I am grateful for his advices on good software development that significantly improved my programming skills.

Special thanks are dedicated to my colleagues Berta Araujo Meleiro and Thierry Bogey. The close collaboration with them during the commissioning of the new SPS position interlock system was very fruitful and straightforward. In this respect, also the aid, guidance and support of Jean-Jacques Savioz, Lars Jensen and Rhodri Jones are remarkable.

I would also like to thank Rüdiger Schmidt for his general support in many aspects and Ralph Steinhagen for several fruitful discussions. My friend Matthias Scholz simplified my start at CERN and in Geneva a lot, for which I am also very grateful. I wish him all the best for his Ph.D. thesis at DESY, Hamburg.

Last but not least, I wish to express special gratitude to my family for their support with words and deeds under all circumstances.

Contents

1. Introduction

The *European Organization for Nuclear Research*, CERN[1] is located near Geneva, Switzerland on the French/Swiss border. CERN was founded in 1954 with four main missions: To perform fundamental research, to advance the frontiers of technology, to improve scientific collaboration and to educate new scientists. The convention [1, II.1.] states:

> "The Organization shall provide for collaboration among European States in nuclear research of a pure scientific and fundamental character [...]. The Organization shall have no concern with work for military requirements and the results of its experimental and theoretical work shall be published or otherwise made generally available."

Today, CERN is the largest laboratory for particle physics worldwide. 20 states are member of the organization. Over 11.000 employees and scientists from 85 countries work and do research at CERN.

1.1. SPS and the CERN Accelerator Complex

CERN is known to host the 27 km long *Large Hadron Collider* (LHC). But apart from that, various other accelerators are in operation at CERN with their own physics programs and as part of the LHC preaccelerator chain.

1.1.1. The CERN Accelerator Complex

In the LHC accelerator chain, protons and ions are accelerated up to 3.5 TeV beam energy (cf. Fig. 1.1). The proton injector chain starts with the linear accelerator *LINAC 2* that accelerates particles up to 50 MeV. In a next step the *PS Booster* accelerates the protons up to 1.4 GeV. In the *Proton Synchrotron* (PS) protons from the PS Booster and ions from the *Low Energy Ion Ring* (Leir) are accelerated up to 26 GeV. At this energy the particles are injected into the *Super Proton Synchrotron*

[1] from French: **C**onseil **E**uropéen pour la **R**echerche **N**ucléaire.

(SPS) which has a top energy of 450 GeV. Via the two transfer lines *TI2* and *TI8*, with a total length of about 6 km, the particles are injected into the LHC that provides hadron collisions at four interaction points with center-of-mass energies of up to 7 TeV since March 30, 2010. An energy of up to 14 TeV is planned to be reached from 2013 onwards.

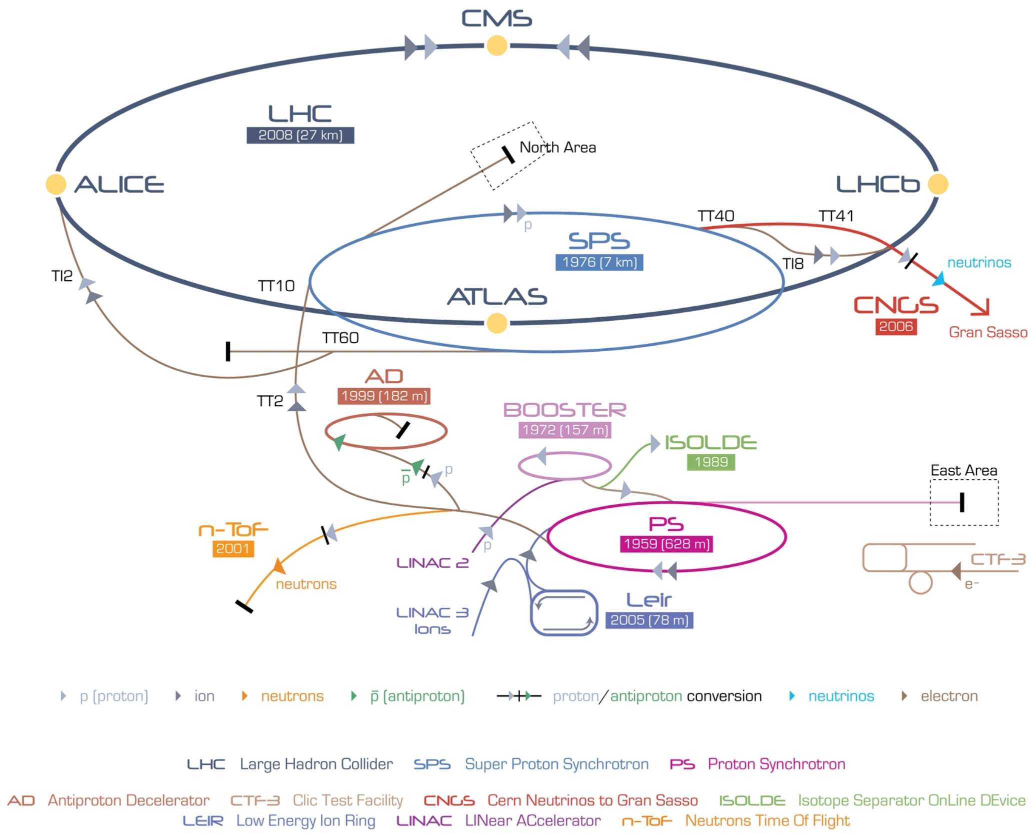

Figure 1.1.: Overview of the CERN accelerator complex.

1.1.2. The Super Proton Synchrotron

The SPS is at the top of the LHC preaccelerator complex. It is a normal conducting accelerator and was fully commissioned in 1976. The SPS served as accelerator for protons, antiprotons, electrons, positrons and heavy ions. Particularly noteworthy are the proton-antiproton collisions in the SPS between 1981 and 1989 (at this time the accelerator was called Sp$\bar{p}$S) that led to the discovery of the W and Z-bosons and the Nobel Prize for Carlo Rubbia and Simon van der Meer in 1984. Today, SPS serves as high intensity, high energy proton and ion accelerator for various experiments and for the LHC.

SPS Experiments

One of the major SPS experiments is the *CERN Neutrinos to Gran Sasso* (CNGS) project. Since 2006, high intensity proton beams with an energy of 400 GeV are brought into collision with a fixed carbon target to produce pions and kaons. These mesons decay to muons and muon-type neutrinos. The muon-type neutrino beam is sent 730 km through the earth to the *OPERA*[2] detector in the Gran Sasso underground laboratory, Italy. Especially the appearance of tau-type neutrinos is of interest to improve the understanding of neutrino oscillations. The OPERA collaboration announced the detection of the first candidate tau neutrino event on May 31, 2010 [2].
Moreover, as part of its fixed target program, the SPS provides different hadron and lepton beams to many experiments. A constant flux can be maintained for a time interval of ≈ 1 s. For example, since 2002 the *COMPASS*[3] experiment uses muon and hadron beams to study the structure and spectrum of hadrons.

The Accelerator

The SPS has a length of 6912 m and is situated in a depth of $23 - 65$ m underground. It consists of six similar arcs of 1028 m length each and six 128 m long straight sections (LSS) in between, resulting in a sixfold machine superperiodicity[4] (cf. Fig. 1.2). Dedicated functions are assigned to the long straight sections:

- **LSS1:** Injection of particles coming from the PS via the TT10 transfer line and beam dump.
- **LSS2:** Slow extraction to fixed target experiments via TT20 transfer line.
- **LSS3:** Particle acceleration.
- **LSS4:** Fast extraction via TT40 transfer line to CNGS target and to LHC point 8 (beam 2) via TI8 transfer line.
- **LSS5:** Transverse beam scraping.
- **LSS6:** Fast extraction to LHC point 2 (beam 1) via TI2 transfer line.

[2]from: **O**scillation **P**roject with **E**mulsion-t**r**acking **A**pparatus.
[3]from: **Co**mmon **M**uon **P**roton **A**pparatus for **S**tructure and **S**pectroscopy.
[4]Periodic substructures of an accelerator are called superperiods.

Each sextant consists of 18 FODO cells[5] with eight dipole magnets per cell in the arcs (cf. Fig. 1.3). Close to the quadrupole magnets, higher order magnets (sextupoles, octupoles), orbit corrector magnets, and beam instrumentation devices like beam position monitors (BPMs) or beam loss monitors (BLMs) are installed.
The acceleration is mainly done by 4 traveling-wave cavities operating at 200 MHz. An additional system of 2 cavities operating at 800 MHz is used to counteract coupled-bunch instabilities via Landau damping [4, p. 123].

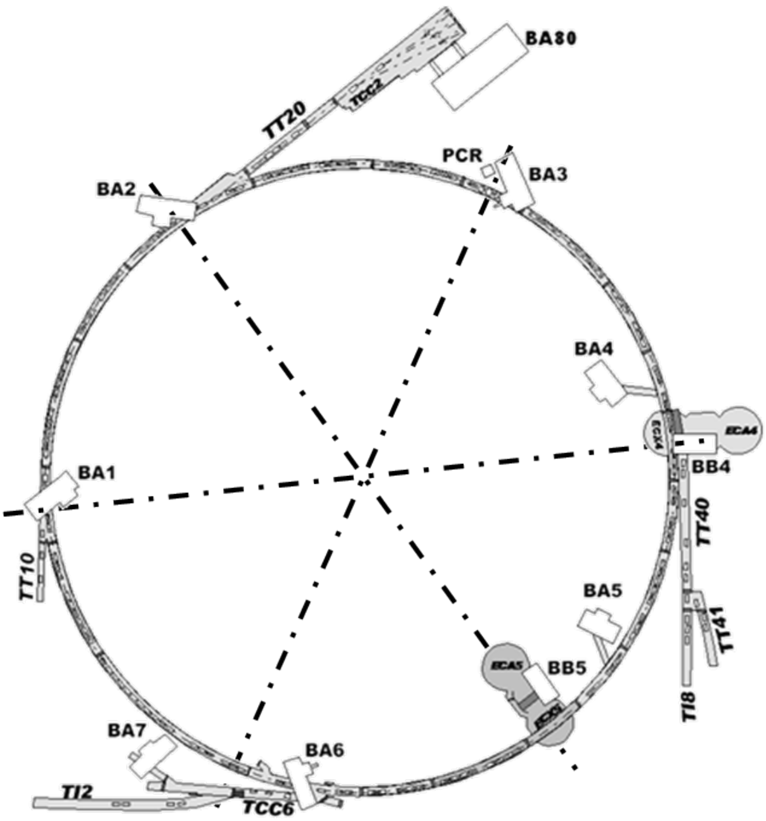

Figure 1.2.: Schematic sketch of the SPS.

The operation of the SPS is very flexible and designed to provide the different users with the required beam properties. It is organized in user dependent operating cycles with a typical length between 6 s for CNGS and 15.6 s for fixed target beam. About six cycles are combined to a constantly repeated supercycle with a usual length of $40 - 50$ s.

[5] A FODO cell describes a periodic structure of transverse focusing accelerator elements. Focusing (F) and defocusing (D) quadrupole magnets are arranged in a periodic way, to achieve transverse beam stability according to the strong focusing principle [3, p. 53].

Figure 1.3.: View inside the SPS tunnel. Dipole magnets are painted red, quadrupole magnets are blue.

1.2. The 2008 SPS Incident

On June 27$^{\text{th}}$, 2008, a beam incident happened in the SPS: A high intensity CNGS beam at 400 GeV with a stored beam energy of about 2.1 MJ became unstable and was lost. The vacuum chamber of the main bending magnet MBB.12530 was punctured in the vertical plane (cf. Fig. 1.4) and the magnet had to be replaced [5].

The incident was caused by a freeze of the *Master Timing Generator* (MTG) during the cycle, due to an ultra-high priority process blocking the CPU of the MTG server. The absence of the extraction timing events inhibited the beam extraction and the beam stayed in the machine after acceleration. At the end of the cycle the magnets were ramped down which resulted in an unintended tune shift towards the $Q_V = 26$ integer tune resonance. The beam became unstable and was lost in the vertical plane.
An analysis of the data from the beam loss monitoring system revealed that the beam was lost in less than 20 ms which is the time resolution of the system (cf. section 2.3.2). The beam loss pattern is characterized by a very broad spatial distribution of the beam losses with small peak beam losses (cf. Fig. 1.5). Only at one BLM the beam losses exceeded the threshold of 50 mGy.

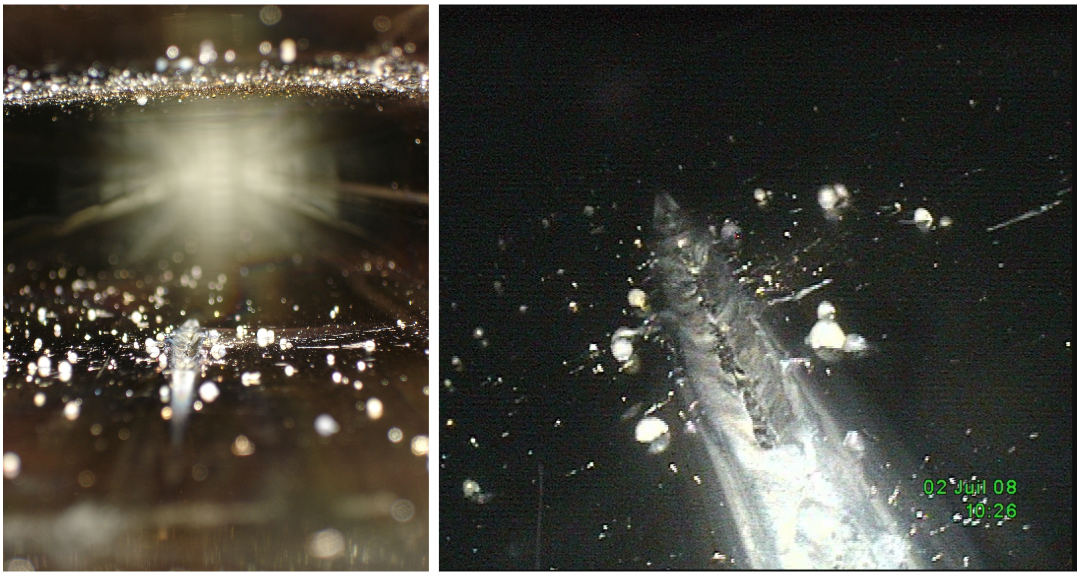

(a) (b)

Figure 1.4.: Beam pipe of the main bending magnet MBB.12530 after the impact of a 2.1 MJ beam. Over a length of about 10 cm the vacuum chamber is punctured. Metal droplets contaminate the beam pipe.

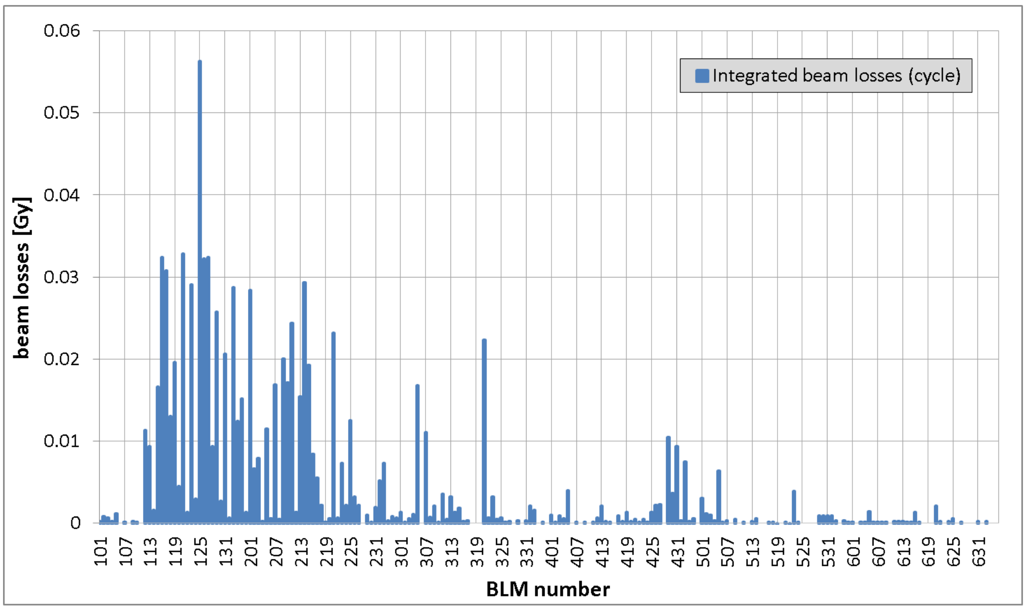

Figure 1.5.: Integrated beam losses of the whole cycle of the incident. The BLM thresholds are typically $30 - 50\,\mathrm{mGy}/20\,\mathrm{ms}$.

1.3. Outline

The incident points out a vulnerability of the SPS to fast beam losses and the challenge of machine protection against tune resonances. A theoretical approach to transverse beam dynamics and tune resonances is given in chapter 2. In the view of this, the machine protection system of the SPS and interesting complementary protection approaches are described.
Comprehensive experimental studies and simulations were made to understand the beam dynamics at different SPS tune resonances. In chapter 3 the results on relevant tune resonance phenomena are presented and the corresponding beam loss pattern are discussed.
Against this background, the machine protection systems of SPS and LHC were reviewed. In chapter 4 the results of crucial tests are summarized and vulnerabilities of the systems are pointed out.
A new fast position interlock system based on a new position acquisition hardware is installed in the SPS to counteract the vulnerability. The whole system (including a new extraction interlock) is explained in chapter 5. Problems encountered during the first commissioning phase and necessary modifications are discussed.
A final discussion and statements on projected SPS upgrade scenarios are given in chapter 6. The approach, the methodology and the results of the thesis work are reflected in chapter 7.

2. Optical Resonances and Related Machine Protection

During the 2008 incident, a fast decrease of the tune led to a beam loss at the $Q_V = 26$ integer tune resonance. This chapter gives an introduction to the relevant transverse beam dynamics in a linear approximation and explains the theory of optical resonances. Against this background, the machine protection system of the SPS is described and relevant machine protection concepts are introduced.

2.1. Transverse Beam Dynamics

For the description of the particle trajectory in an accelerator a co-moving coordinate system is used (cf. Fig. 2.1). It is defined with respect to the *design orbit* that describes the closed trajectory of an ideal particle in the ideal machine under design conditions[1]. The transverse axis that is parallel to the accelerator plane is defined as x-axis or as horizontal axis. The y-axis or vertical axis is perpendicular to the accelerator plane.

2.1.1. Linear Equations of Motion

In a particle accelerator, the transverse motion is dominated by magnetic fields. Their influence on the momentum $\mathbf{p}$ of a particle with charge q is given by the Lorentz force:

$$\dot{\mathbf{p}} = q \cdot (\mathbf{v} \times \mathbf{B}) \tag{2.1}$$

with $\mathbf{B}$ being the magnetic field vector and $\mathbf{v}$ the particle velocity. For $\mathbf{B} \perp \mathbf{p}$ the equilibrium of Lorentz force and centrifugal force leads to the definition of the *beam rigidity* [6, p. 82]:

$$B\rho = \frac{p}{q} \tag{2.2}$$

[1] It is distinguished between the static *design orbit* and the *closed orbit* that describes the closed trajectory of an ideal particle in the real accelerator. The closed orbit is dynamic and depends amongst others on the machine settings.

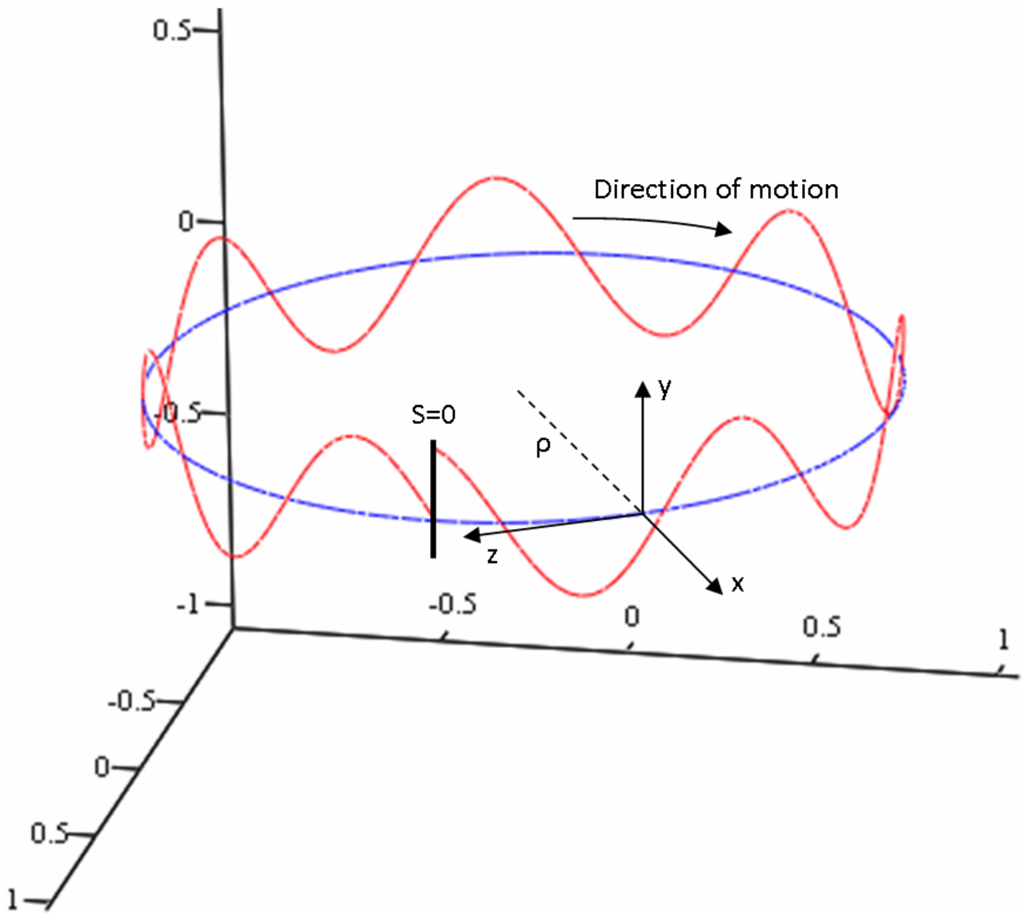

Figure 2.1.: The trajectory of an ideal particle (blue) and the trajectory of a particle oscillating in the vertical plane (red) in a global coordinate system. A co-moving coordinate system is also drawn.

with ρ being the bending radius, $B = |\mathbf{B}|$ and $p = |\mathbf{p}|$.
By keeping only the leading terms in linear approximation, Eq. 2.1 can be rewritten as a differential equation of motion[2]:

$$\begin{aligned} x''(s) + k_x(s)\,x(s) &= \frac{1}{\rho(s)}\frac{\Delta p}{p} \\ y''(s) + k_y(s)\,y(s) &= 0 \end{aligned} \tag{2.3}$$

with the momentum offset $\frac{\Delta p}{p}$ and s being the longitudinal position. k_x and k_y are related to the strength[3] $K(s)$ of the quadrupolar fields:

$$\begin{aligned} k_x &= \frac{1}{\rho^2} - K(s) = \frac{1}{\rho^2} + \frac{1}{B\rho}\frac{\partial B_y}{\partial x} \\ k_y &= K(s) = -\frac{1}{B\rho}\frac{\partial B_y}{\partial x} \end{aligned} \tag{2.4}$$

[2]cf. for example [3, p. 126 ff.] or [7, p. 46 ff.] for a more detailed introduction.
[3]The sign of the quadrupole strength is arbitrary. Here K is chosen to be < 0 for focusing quadrupoles.

Note that the equations of motion (cf. Eq. 2.3) are uncoupled for horizontal and vertical plane, i.e. the movements in horizontal and vertical plane are independent. Thus, both planes can be treated separately[4].

For $\frac{\Delta p}{p} = 0$ the equations of motion (cf. Eq. 2.3) are Hill-type differential equations[5]. By using *Floquet's Theorem* the general solution can be found:

$$x(s) = \sqrt{\epsilon\beta}\cos\left[\psi(s) - \psi(s_0)\right] \tag{2.5}$$

with ϵ and $\psi(s_0)$ being the initial conditions. β is the periodic *betatron* or *beta function* which is per definition always positive and in a regular FODO lattice (cf. section 1.1.2) maximal at focusing quadrupole magnets and minimal at defocusing quadrupole magnets. $\psi(s)$ is the *betatron phase* of the oscillation and depends on the beta function:

$$\psi(s) = \int_{s_0=0}^{s} \frac{d\bar{s}}{\beta(\bar{s})} \tag{2.6}$$

with $s_0 = 0$ an arbitrary but fixed longitudinal position of the accelerator. Figure 2.2 shows the betatron function and the betatron phase in a regular FODO structure in the SPS.
The *emittance* ϵ is relevant for the amplitude $\sqrt{\epsilon\beta}$ of the oscillation. It usually decreases during acceleration which is why often the *normalized emittance* $\epsilon^{n,1\sigma} = \epsilon\beta_r\gamma_r$ is used[6]. For a multi-particle beam, a Gaussian particle distribution is frequently assumed. The standard deviation $\sigma = \sqrt{\epsilon\beta}$ is referred to as transverse beam size.

2.1.2. Betatron Oscillation, Tune and Chromaticity

Equation 2.5 shows that the particle trajectory has oscillatory behaviour. The oscillations are called *betatron oscillations*, since they were first observed in betatron accelerators [9]. Figure 2.1 shows the trajectory of a particle oscillating in the vertical plane around the closed orbit.
The number of betatron oscillations per revolution is called *tune*[7]. Equation 2.6 leads to the following relation between tune Q and beta function:

$$Q = \frac{1}{2\pi}\left[\psi(s+C) - \psi(s)\right] = \frac{1}{2\pi}\oint_{s}^{s+C} \frac{d\bar{s}}{\beta(\bar{s})} \tag{2.7}$$

[4] The following discussion will focus on the horizontal plane, unless indicated otherwise.

[5] The Hill's equation is a homogeneous differential equation of second order without first order derivatives. It was first studied by the astronomer G. Hill to find a solution to the three-body problem [8].

[6] $\beta_r = \frac{v}{c}$ and $\gamma_r = \frac{1}{\sqrt{1-\beta_r^2}}$ are the functions known from the theory of relativity. For LHC-type beam $\epsilon_{H/V}^{n,1\sigma} = 3.5\mu m \cdot rad$.

[7] The blue particle in Fig. 2.1 makes 7.2 vertical betatron oscillations per turn. Thus, it has a vertical tune of $Q_V = 7.2$

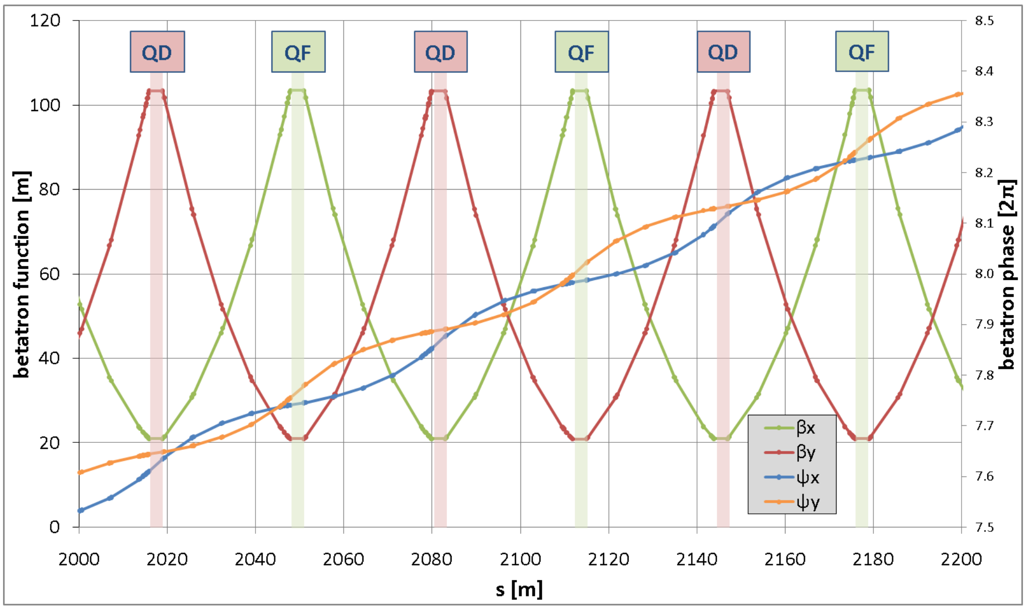

Figure 2.2.: Betatron function and betatron phase for the regular FODO structure of the SPS.

with C being the circumference of the accelerator ($C = 6912\,\mathrm{m}$ for the SPS).

Combining Eq. 2.4 and Eq. 2.2 shows that the strength $K(s)$ of quadrupolar fields is inversely proportional to the particle momentum. This results in a momentum dependency of the tune. In a linear approximation, the chromaticity ξ is defined as the proportionality factor between momentum offset and tune change:

$$\Delta Q = \xi \cdot \frac{\Delta p}{p}. \tag{2.8}$$

In the SPS, the natural chromaticity due to quadrupole fields is ≈ -33 (for both planes). In order to reduce the *tune spread*[8] and to avoid head-tail instabilities [7, p. 120 ff.], sextupole magnets are used to correct the negative natural chromaticity (cf. section 3.1.4).

Table 2.1 summarizes some of the most important optics parameter of the SPS.

2.2. Optical Resonances

The optics of an accelerator can lead to resonant and diverging beam dynamics (*optical resonance*). Even small field imperfections (within the error margin) of real accelerators can lead to crucial effects. The effect of these field errors can add-up over consecutive revolutions for particular tune values (in this respect the term *tune*

[8] The *tune spread* defines the band-width of the different tune values of the particles in a beam.

	Injection	Flat Top
Momentum (LHC)	26 GeV/c	450 GeV/c
Momentum (CNGS, FT)	14 GeV/c	400 GeV/c
Tune (LHC)	26.13/26.18 (H/V)	
Tune (CNGS, FT)	26.58/26.61 (H/V)	
Beta function at QF	103/21 m (H/V)	
Beta function at QD	21/103 m (H/V)	
$\epsilon_{H/V}^{n,1\sigma}$ (LHC)	$\approx 3.5\,\mu$m · rad	
$\epsilon_{H/V}^{n,1\sigma}$ (CNGS, FT)	$\approx 5-6\,\mu$m · rad	
σ at QF (LHC)	$\approx 3.6/1.6$ mm (H/V)	$\approx 0.9/0.4$ mm (H/V)
σ at QF (CNGS, FT)	$\approx 6.4/2.9$ mm (H/V)	$\approx 1.2/0.5$ mm (H/V)

Table 2.1.: Relevant machine and beam parameters of the SPS for CNGS-type beam, fixed target beam (FT), and LHC-type beam.

resonance is also used). Generally, a $2n$-polar field error leads to a resonance when $n\,Q$ is an integer. In two dimensions, the general resonance condition for the tune is

$$m\,Q_H + n\,Q_V = p, \quad m, n, p \in \mathbb{Z} \tag{2.9}$$

with Q_H and Q_V being horizontal and vertical tune. $|m| + |n|$ is the order of the resonance, lower order resonances are usually more pronounced. Tunes and resonances are often displayed in a tune diagram (cf. Fig. 2.3 for nominal LHC-type beam).

Tune resonances are not discrete but have a certain width called *stop band width*. It depends on beam parameters, like the tune spread, as well as on machine parameters that define the width of the underlying tune resonance phenomena (cf. chapter 3). Some of the most important reasons for tune resonances and their impact on the beam dynamics are introduced in the following sections.

2.2.1. Dipolar Fields or Dispersion Resonance

Optical resonances are not only due to field errors, also the main fields can lead to diverging behaviour. As indicated by Eq. 2.3, dipolar fields modify the trajectory of particles with a momentum deviation $\frac{\Delta p}{p}$. A linear ansatz can be made for the solution of the inhomogenious equation:

$$x(s) = x_0(s) + D_x(s) \cdot \frac{\Delta p}{p} \tag{2.10}$$

with $D_x(s)$ being the horizontal dispersion function and x_0 being the solution to the homogeneous Hill's equation (cf. Eq. 2.5). By considering the periodic boundary

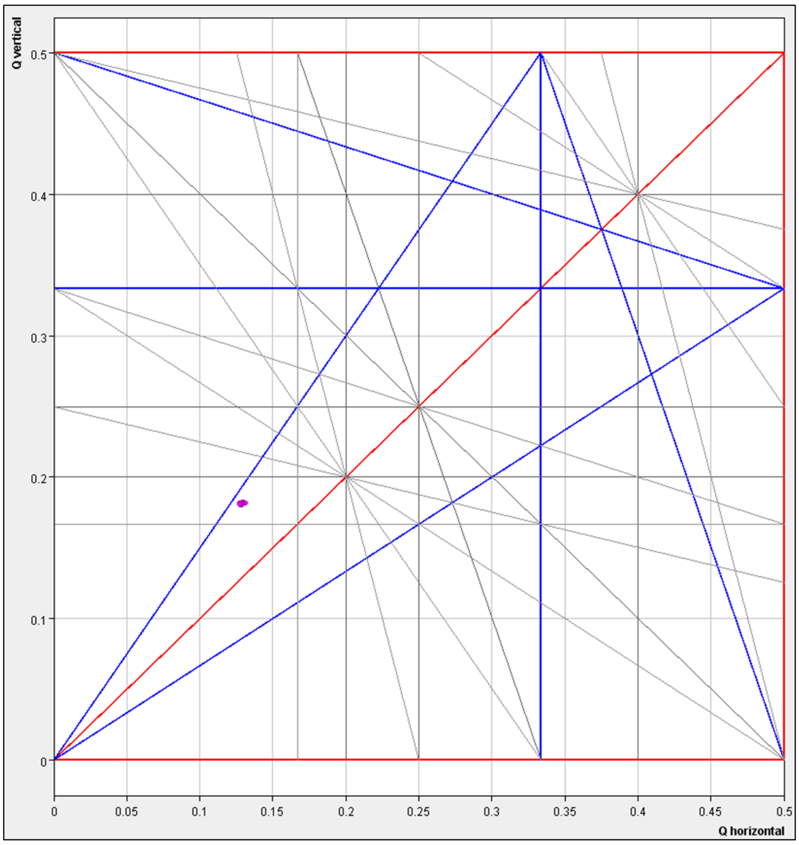

Figure 2.3.: Tune diagram for LHC-type beam. The pink dots represent various tune measurements during the whole cycle. The straight lines indicate tune resonances. Only the fractional part of the tunes is given.
Measurement conditions: cycle: MD1, beam energy: $26 - 450\,\text{GeV}$, bunch intensity: $6 \cdot 10^9$ protons, 12 bunches.

conditions, the dispersion function can be calculated to be [3, p. 264 ff.]:

$$D(s) = \frac{\sqrt{\beta(s)}}{2\sin(\pi Q)} \oint_{s_0}^{s_0+C} \frac{1}{\rho(\bar{s})} \sqrt{\beta(\bar{s})} \cos\left[\psi(\bar{s}) - \psi(s) - \pi Q\right] d\bar{s}. \tag{2.11}$$

This important equation shows that the dispersion is an integrated effect of all bending fields. The $\frac{1}{\sin(\pi Q)}$ proportionality indicates that integer tune values lead to a diverging dispersion and thus to diverging transverse particle positions and related beam losses.

2.2.2. Dipolar Field Errors or Closed Orbit Distortion

A real accelerator has imperfect dipolar field components which are of different origins:

- Misalignments Δx of quadrupole magnets result in dipolar field components which are given by $\Delta B_y = (\partial B_y/\partial x)\Delta x$ (*feed-down*). In large accelerators this is usually the most important source of dipolar field errors [3, p. 292].
- The closed orbit in general differs from the design orbit which results in an off-center trajectory even in a well aligned quadrupole. Similarly to the first point, the beam is effected by an additional dipolar field.
- Imperfections in the construction of higher order magnets or deviations in the strength of dipole magnets lead to dipolar magnetic field errors.

Such a dipolar field error leads to a small additional angular kick[9]. As illustrated by Fig. 2.4, for integer tune values, the kicks of consecutive revolutions are in phase and add-up. This results in a diverging oscillation of the closed orbit. In general, there are many different dipolar field errors in the accelerator that lead to a *closed orbit distortion*. Under consideration of the periodic boundary conditions, the displacement of the closed orbit can be calculated to be:

$$\Delta x_{CO}(s) = \frac{\sqrt{\beta(s)}}{2\sin(\pi Q)} \oint_{s_0}^{s_0+C} F(\bar{s}) \sqrt{\beta(\bar{s})} \cos\left[\psi(\bar{s}) - \psi(s) - \pi Q\right] d\bar{s} \tag{2.12}$$

with $F(s)$ being the error function that contains all the angular kicks from dipolar field errors [3, p. 289 ff.]. Note that the description of the closed orbit displacement (cf. Eq. 2.12) is very similar to the description of the dispersion (cf. Eq. 2.11). Thus, also the closed orbit distortion is resonant for integer tune values.

A resonant closed orbit distortion is a very dangerous beam loss scenario, since the transverse beam position may increase very fast, until it reaches the aperture,

[9] In a thin approximation, i.e. the accelerator elements have zero length, the effect of a dipolar field is described as a discrete change of the angular direction of the particle motion, called kick.

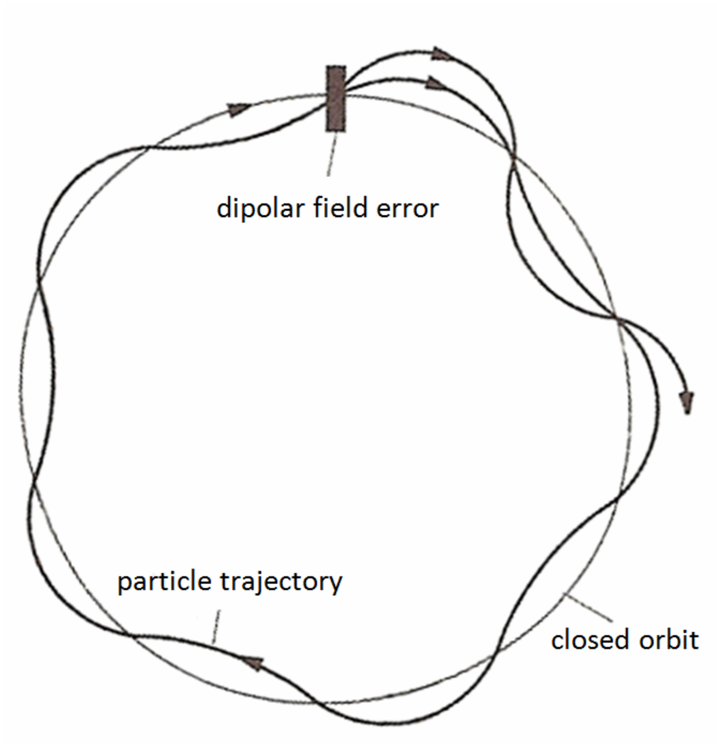

Figure 2.4.: Closed orbit distortion by a dipolar field error for an integer tune. The orbit increases with every turn. [7, p. 106]

while the beam size stays small. It results in very localized beam losses with high local energy deposition.

2.2.3. Quadrupolar Field Errors or Beta Beating

Quadrupolar field errors are represented by a change of the quadrupole strength $\delta K(s)$. They result in local variations of the beta function called *beta beating*[10]. Like calculated in [3, p. 294], it is given by

$$\frac{\Delta\beta(s)}{\beta(s)} = \frac{1}{2\sin(2\pi Q)} \oint_{s_0}^{s_0+C} \delta K(\bar{s})\beta(\bar{s})\cos 2\left[\psi(\bar{s}) - \psi(s) - \pi Q\right] d\bar{s}. \tag{2.13}$$

Unlike Eq. 2.11 and Eq. 2.12, Eq. 2.13 is resonant for integer and half integer tune values. This is due to the spatial anti-symmetry of the quadrupolar field which leads also for a 180° betatron phase advance (= phase advance between two consecutive turns for a half integer tune) to an increasing effect.

Especially a resonant beta beating and dispersion lead to various other tune resonance phenomena, like a resonant chromaticity (cf. section 3.1.4) and *momentum*

[10] Additionally, the change of the quadrupole strength shifts the tune by $\Delta Q = \frac{1}{4\pi} \oint_s^{s+C} \delta K(\bar{s})\beta(\bar{s})d\bar{s}$.

compaction factor[11]. Hence, in particular integer tune resonances are characterized by a large variety of tune resonance phenomena.

2.3. SPS Machine Protection

The SPS is at present the accelerator with the highest stored beam energy worldwide of up to 2.5 MJ [10, p. 5]. To protect the accelerator from beam induced damage, the complex machine protection system measures and monitors critical parameters and settings. This is done on three levels by the hardware based *Beam Interlock System* and *Extraction Interlock Systems* and by the *Software Interlock System.*

2.3.1. Beam Dump System

To remove the beam safely from the SPS without damaging the machine, the beam is dumped in the vertical direction on one of the internal beam dump blocks TIDH and TIDV. For energies below 37 GeV the beam is dumped on TIDH, for energies above 105 GeV on TIDV[12]. The rise time of the two vertical dump kickers is $250 - 300$ ns ($\approx 1/80$ turn). To distribute the high beam energy over a large volume of the absorber block, three horizontal kickers provide a damped half-sine sweep with a rise time of $\approx 25\,\mu$s (≈ 1 turn) [11].

2.3.2. Beam Interlock System

The trigger signals of the interlock devices are sent to the beam dump system via standardized *Beam Interlock Controller* (BIC) modules. The six BICs of the SPS ring (one per access point) are linked together by a *Beam Permit Loop.* If the state of one of the connected input signals turns to *FALSE* an emergency beam dump is triggered[13]. The intrinsic reaction time of the beam interlock system is a few μs ($<< 1$ turn).
Some of the most important interlock systems are described in the following sections.

[11] A momentum offset $\frac{\Delta p}{p}$ leads to a relative change of the longitudinal length of the closed orbit $\frac{\Delta C}{C_0}$ with the momentum compaction factor α_P as proportionality factor: $\frac{\Delta C}{C_0} = \alpha_P \frac{\Delta p}{p}$. The momentum compaction factor strongly depends on the dispersion [3, p. 267]: $\alpha_p = \frac{1}{C_0} \oint_{s_0}^{s_0+C} \frac{1}{\rho(\bar{s})} D(\bar{s}) d\bar{s}$.

[12] In the intermediate region the beam is spread over both absorber blocks. Only emergency beam dumps are allowed in this region, otherwise also programmed beam dumps are possible.

[13] Some of the connected input channels are *maskable*, i.e. they can be deactivated (=*masked*).

Beam Loss Monitors

In the SPS, about 300 beam loss monitors (BLMs), based on ionization chambers, constantly monitor the beam losses. Three types of BLMs are used:

- **Ring type BLMs (BLRING)** are installed in the SPS ring and in the north transfer line (TT20). The software processing of the signals determines the slow reaction time of $\approx 20\,\mathrm{ms}$ ($= 870\,\mathrm{turns}$).
- **Extraction type BLMs (BLD)** are installed in the extraction regions of LSS1, LSS2, LSS4 and LSS6. The signal processing is done in the hardware with a reaction time of $\approx 1\,\mu\mathrm{s}$.
- **Transfer line BLMs (BLMI)** are installed in the transfer lines TT40, TT41, TT60, TI2 and TI8. They react after the extraction and can only prevent further extractions.

For the ring-type BLMs a beam dump signal is sent if the threshold of usually $30 - 50\,\mathrm{mGy}/20\,\mathrm{ms}$ is exceeded by at least two BLMs.

Analog Fast Position Interlock

An analog fast position interlock is protecting the SPS against fast changes of the horizontal beam position. The two horizontal pickups BPH.120 and BPH.122 close to LSS1 with 87° betatron phase difference are used for a coverage of the full phase space. A beam dump signal is sent, if the measured position at one pickup exceeds 30 mm. The interlock is limited to high intensity beams (above 10^{12} protons). The response time is 2 turns [11].

The fact that the system is limited to the horizontal plane and does not provide any operational flexibility or post mortem data makes it outdated compared to the overall SPS machine protection system.

Power Converter Interlock

A surveillance of the main SPS power converters (dipoles, quadrupoles, sextupoles) is done on two levels ([11], [12]):

- The power converter provides a slow state signal. If this state in not *ON*, a beam dump signal is sent.
- A fast internal interlock system detects power losses, electrical perturbations or converter failures. The reaction time is several ms (cf. section 4.2).

2.3.3. Extraction Interlock Systems

Prior to a beam extraction to the TT40 and TT60 transfer line, various interlock conditions like vacuum, beam losses or beam position are checked. In total 11 BICs in two independent *Extraction Interlock Systems* for TT40 and TT60 process the interlock signals and can inhibit the extraction. In contrast to the beam interlock system, *masked* input channels are only deactivated for low beam intensities (below 10^{12} protons). For high intensity beams, masked interlock devices are automatically activated.

Special operational limitations are given by the beam position interlock. In total 13 pickups are read out 50 ms before the extraction to ensure that the beam position at the extraction bumps is within the acceptance of the septum magnets [4, p. 173]. The tolerance is set to $\pm 2-3$ mm. For the acquisition, the normal *MOPOS* hardware is used [13]. *MOPOS* relies on the right selection of one out of seven BPM gain factors, depending on the beam intensity. As a result, the gain factors need to be manually adjusted with every change of the beam intensity. During the cycle it is not possible to work with other gain factors without causing an extraction inhibit. Furthermore, the timing of the acquisition chain must be manually gated on the beam.
These limitations make a replacement of the system desirable.

2.3.4. Software Interlock System

A flexible software package provides additional security on top of the hardware based interlock systems. The *Software Interlock System* (SIS) monitors about 1000 parameters, states and settings at the end of each SPS cycle [14]. It is connected to the Beam Interlock System as well as to the Extraction Interlock Systems on the BIC level. Additionally, it is connected to the SPS *Master Timing Generator* which allows the SIS to inhibit beam in the SPS injectors.
In the SIS, the various interlock conditions are combined in a tree-like structure by logic *AND* or *OR* operators. In this way, the SIS returns in total 14 logic *TRUE* or *FALSE* beam permit signals for the different operating processes.

2.4. Other Machine Protection Concepts

Especially the LHC needs a very sophisticated beam interlock system, since the nominal stored energy of its beams (which will be reached in the next years) is over two orders of magnitude higher than the stored beam energy in the SPS. Although

the layout of the machine protection system is in many aspects similar to the SPS, it utilizes some very advanced failure detection concepts, most of them developed and tested at high-energy particle accelerators worldwide.
Especially *Fast Magnet Current Change Monitors* (FMCMs) are intersting protection devices against fast equipment failures. The concept is explained in the following section.

Fast Magnet Current Change Monitors

The *HERA* accelerator at DESY suffered from a vulnerability to fast failures of the quadrupole power converters that led to beam incidents in 2003 [15]. Driven by this issue, FMCMs were developed and installed in 2004. An FMCM can detect a fast change of the magnet current by monitoring voltage changes over the magnet circuit [16]. Fast reaction times ($< 50\,\mu$s) are combined with a high relative sensitivity ($\approx 10^{-4}$), but FMCMs cannot detect slow current changes [17]. Thus, they must always be combined with other protection devices.
Followed by a good performance of the FMCMs at HERA, 12 FMCMs were installed in normal conducting LHC circuits [18, p. 42] and also some critical extraction magnets in the SPS are monitored by FMCMs[14].

[14] For the surveillance of the extraction magnets, the FMCMs work in a special operating mode called *Pulsed Beam Mode*. In this operating mode it is crucial to detect small current changes in a short time interval after ramping the extraction magnets quickly to the flat top [15].

3. Tune Resonance Phenomena

Tune resonances are a challenging machine protection problem that can lead to severe machine damage as was underlined by the 2008 incident in the SPS (cf. section 1.2). In this chapter, the results from distinct simulations and experimental studies in the SPS on tune resonance phenomena and the corresponding beam loss pattern are presented. The beam dynamics at different tune resonances are analyzed and compared and the question why especially integer tune resonances are so threatening is answered.
Among the tune resonance phenomena the focus is put on closed orbit divergence, resonant dispersion (and its influence on the chromaticity) and increased beta beating, which are the driving effects for fast beam losses.

3.1. Beam Dynamics at Tune Resonances

The SPS has a known vulnerability to fast beam losses as is discussed in chapter 4. Especially threatening in this sense are integer tune resonances as becomes obvious when looking at the case depicted in Fig. 3.1. The graph shows a measurement of the horizontal beam position at three particular beam position monitors (BPMs) close to the $Q_H = 26$ integer tune resonance and the corresponding beam intensity[1].

The horizontal tune is decreased linearly by about $-2 \cdot 10^{-3}/\,\text{turn}$.[2] The beam position starts to diverge about 40 turns before the resonance is reached, leading to a complete beam loss about 8 turns before the resonance peak would have been reached. Most challenging is the fact that it takes only 3 turns ($= 69\,\mu$s) to loose the complete beam after the first beam losses start. This leaves practically no reaction time for an adequate machine protection based on BLMs.

[1] To determine the beam intensity on a turn-by-turn base, the intensity measured by the BPMs is used. The beam current transformers (BCTs) are not suitable, since their time resolution is too slow.

[2] The slope of the tune can be determined on a turn-by-turn base from the betatron-frequency measured by the turn-by-turn position acquisition. An alternative is to approximate the tune from the current measurement of the quadrupole circuits (cf. section 3.3.2). In this case the first method is used. The normal tune measurement is not applicable for fast tune changes.

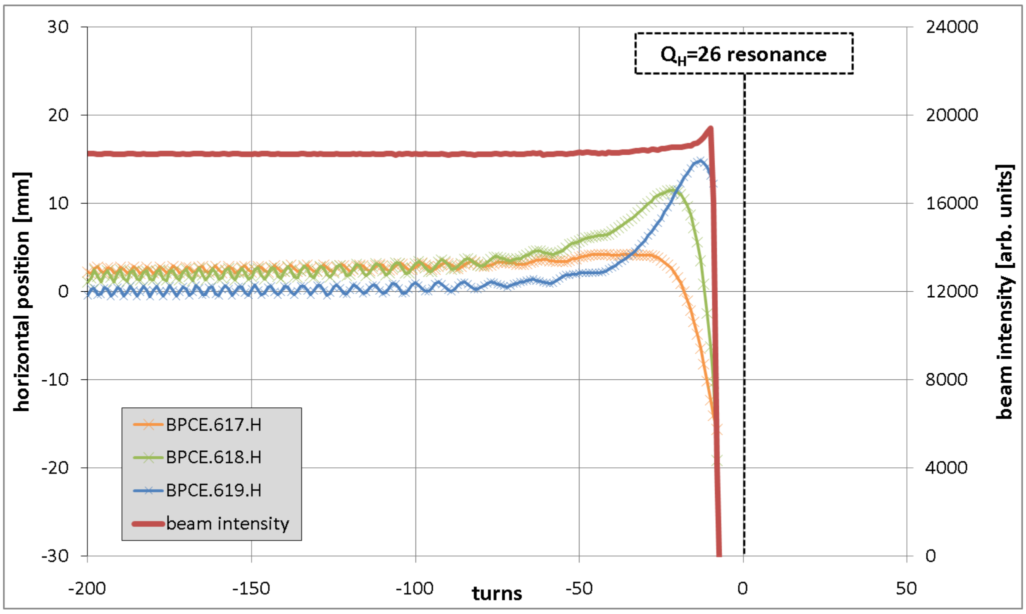

Figure 3.1.: Beam intensity and horizontal turn-by-turn beam position at three particular BPMs. The horizontal tune is decreased linearly by about $-2 \cdot 10^{-3}/turn$. The beam is lost at a tune of about $Q_H = 26.015$. **The complete beam is lost within 3 turns after the first beam losses start.**
Measurement conditions: cycle: LHCFAST2, beam energy: 450GeV, bunch intensity: $1.0 \cdot 10^{10}$ protons, 12 bunches.

Under certain conditions that are analyzed in section 3.3 crossing of an integer tune resonance is also possible. Figure 3.2 depicts a case where the $Q_H = 26$ integer resonance is crossed without a measurable decrease of beam intensity. The beam is strongly excited by the resonance, which leads to large beam oscillations of up to 20 mm amplitude, but without a significant decrease of beam intensity. Because of these strong excitations, integer tune resonance crossings are often accompanied by extreme emittance blow-ups. A beam wire scan before and after the resonance crossing (cf. Fig. 3.3) shows the drastic change of the transverse beam profile. In this case[3], the emittance increases by a factor of ≈ 60 due to the resonance crossing, filling essentially the entire machine aperture.

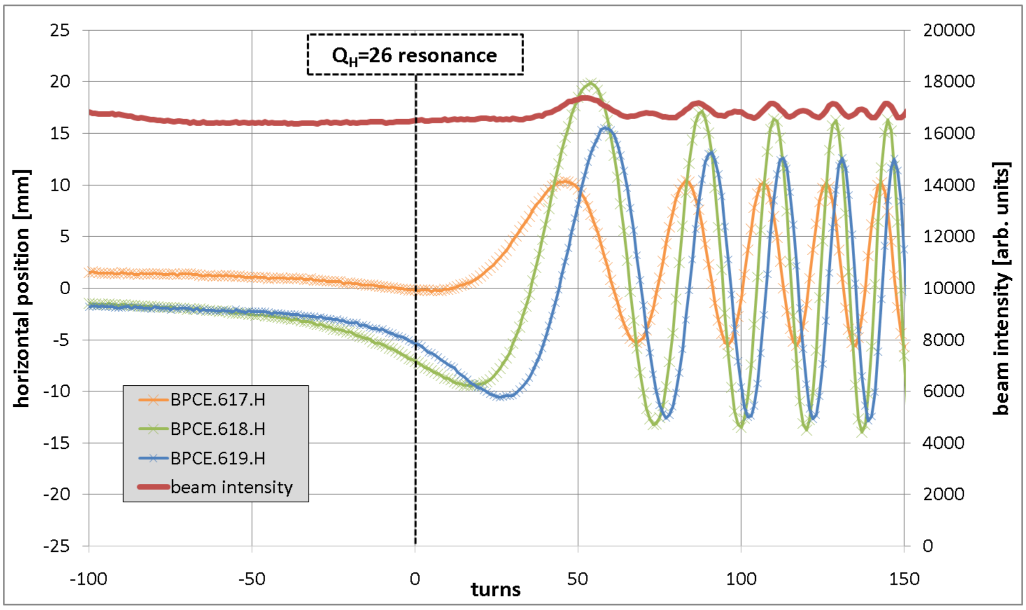

Figure 3.2.: Horizontal turn-by-turn beam position at three particular BPMs and beam intensity. The horizontal tune is decreased linearly by about $-4 \cdot 10^4/turn$. The beam crosses the $Q_H = 26$ integer resonance without measurable losses but is strongly excited.
Measurement conditions: cycle: LHCFAST2, beam energy: 200 GeV, bunch intensity: $1.0 \cdot 10^{10}$ protons, 12 bunches.

Besides these effects, tune resonances lead to a large variety of resonance phenomena, as is introduced in section 2.2. In the following, a closer look is taken on the resonance phenomena that dominate fast beam losses, i.e. the resonant behaviour of closed orbit, dispersion and beta beating.

[3] About 30% of the beam are lost while crossing the integer tune resonance.

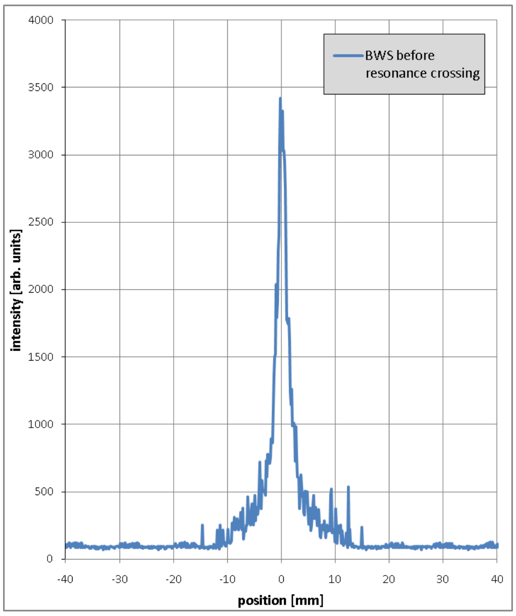

(a) Beam wire scan before resonance crossing

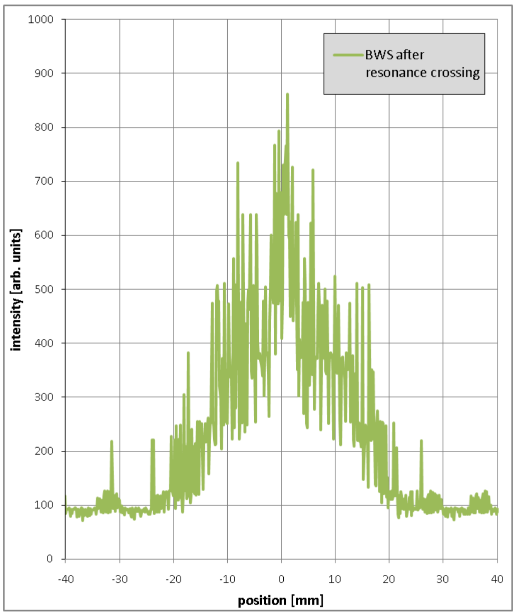

(b) Beam wire scan after resonance crossing

Figure 3.3.: Horizontal beam profile measured by a beam wire scanner before and after the crossing of the $Q_H = 26$ integer tune resonance. The normalized horizontal emittance increases from $\epsilon_H^{n,1\sigma} = 0.6\,\mu\text{m}\cdot\text{rad}$ to $\epsilon_H^{n,1\sigma} = 34.7\,\mu\text{m}\cdot\text{rad}$ during the resonance crossing.
Measurement conditions: cycle: MD1, beam energy: 26 GeV, bunch intensity: $1.0\cdot 10^{10}$ protons, 12 bunches.

3.1.1. Closed Orbit Resonances

As demonstrated by Eq. 2.12, the closed orbit diverges when the tune approaches an integer value. It is the main cause of the diverging beam positions shown in Fig. 3.1 and Fig. 3.2[4]. Measurements and simulations[5] of the rms closed orbit show a broad resonant behaviour for integer tune values (cf. Fig. 3.4). Especially the nominal tunes of LHC-type beam ($Q_H = 26.13$ and $Q_V = 26.18$) are particularly close to the $Q = 26$ integer tune resonance. An erroneous decrease of the tune will directly drive the closed orbit into resonance.

The different shapes of the closed orbit resonance for different integer tunes, especially in the horizontal plane, are due to symmetries of the accelerator that are discussed in section 3.2.

3.1.2. Dispersion Resonances

Like the closed orbit, the dispersion has a $\frac{1}{\sin(\pi Q)}$ resonant behaviour for integer tunes (cf. section 2.2.1). However, simulation[6] and measurement[7] reveal an enormous $Q_H = 24$ superperiodic tune resonance (cf. Fig. 3.5). The reason of the special beam dynamics at the $Q = 24$ tune resonance and the difference between dispersion and closed orbit resonances at $Q_H = 24$ is discussed in more detail in section 3.2. Due to the energy-spread, the enormous dispersion resonance leads to a diverging transverse beam size and related beam losses.

Noteworthy is also the behaviour of the dispersion function. Measurement and simulation are in good agreement and show major changes in the shape of the dispersion function in the vicinity of tune resonances (cf. Fig. 3.6). Whereas the horizontal dispersion (cf. Eq. 2.11) is mainly positive under nominal conditions (cf. Fig. 3.6a), the dispersion function starts to oscillate with diverging amplitudes when approaching an integer tune resonance. Thus, the dispersion turns to be negative for large parts of the accelerator. The $\frac{1}{\sin(\pi Q)}$ behaviour implies a change of sign of the dispersion function at the tune resonance. This behaviour leads to a breakdown of the chromaticity correction by sextupoles as is discussed in section 3.1.4.

[4] Nevertheless, it needs to be pointed out that other resonance phenomena like diverging beta beating (cf. section 3.1.3) increase the divergent behaviour of the transverse beam position.

[5] A detailed explanation about the simulations is given in Appendix A.

[6] cf. Appendix A for details on the simulation.

[7] Horizontal dispersion D_x and vertical dispersion D_y are determined by measuring the beam position for different RF frequencies as described in [19, p. 152 ff.]. It is crucial to take into account that second order dispersion (cf. Fig. 3.7) and momentum compaction factor also have a diverging behaviour for tune values around $Q_H = 24$. The latter results in a tune dependent relation between relative RF frequency trim and momentum offset.

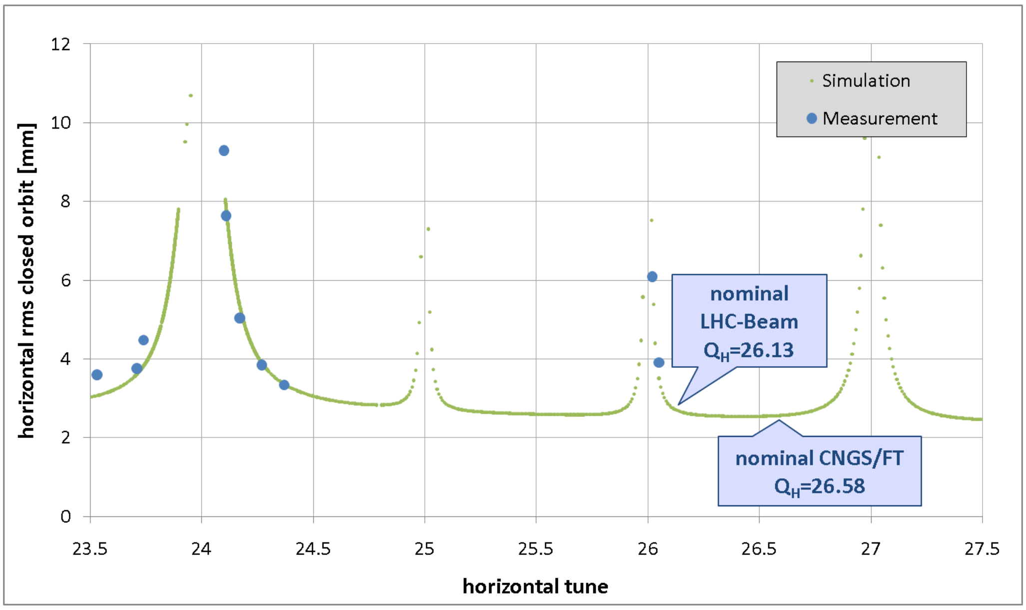

(a) Simulation and measurement of the horizontal rms closed orbit as a function of the horizontal tune.

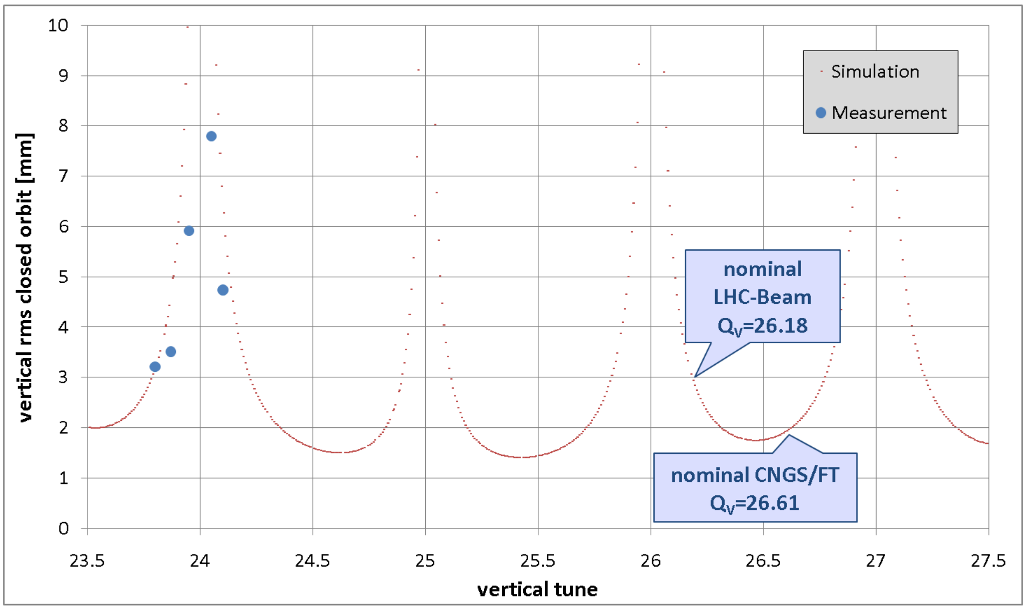

(b) Simulation and measurement of the vertical rms closed orbit as a function of the vertical tune.

Figure 3.4.: Rms closed orbit at tune resonances.
Measurement conditions: cycle: MD2, beam energy: 26 GeV, bunch intensity: $4 \cdot 10^{10}$ protons, 12 bunches.

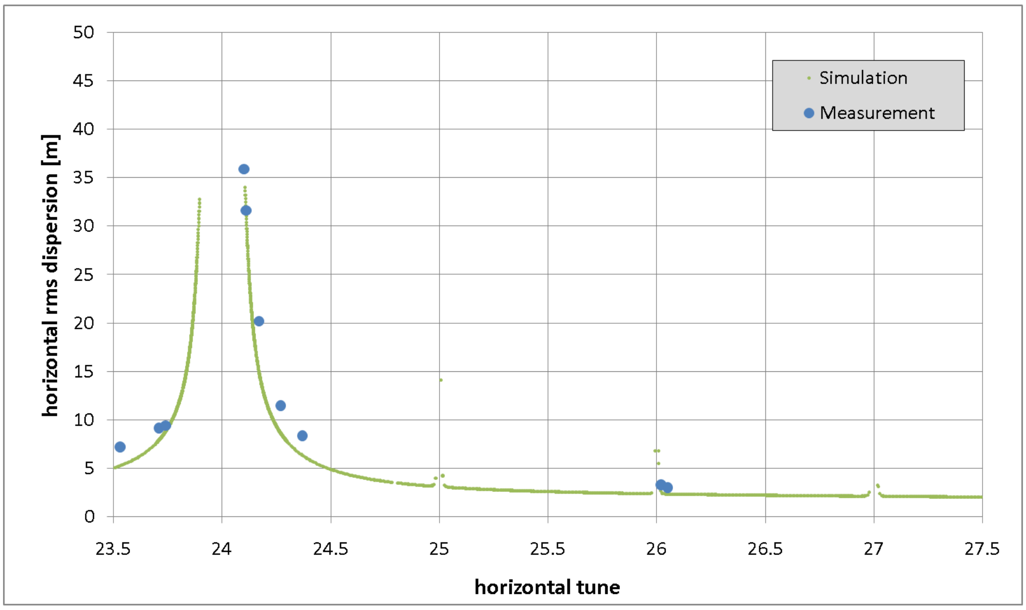

(a) Simulation and measurement of the horizontal rms dispersion as a function of the horizontal tune.

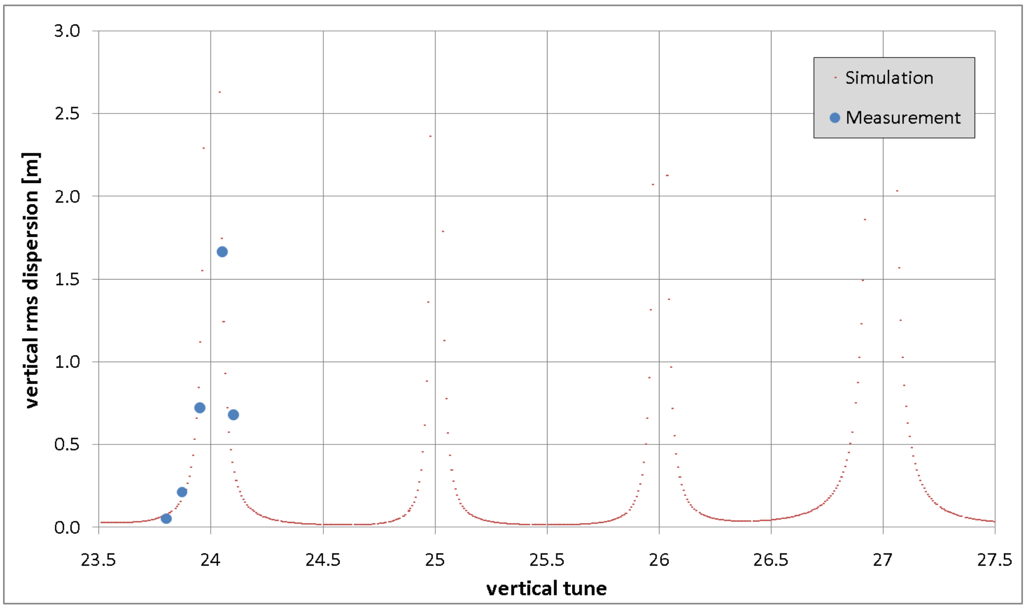

(b) Simulation and measurement of the vertical rms dispersion as a function of the vertical tune.

Figure 3.5.: The horizontal rms dispersion shows an enormous resonance at $Q_H = 24$.
Measurement conditions: cycle: MD2, beam energy: 26 GeV, bunch intensity: $4 \cdot 10^{10}$ protons, 12 bunches.

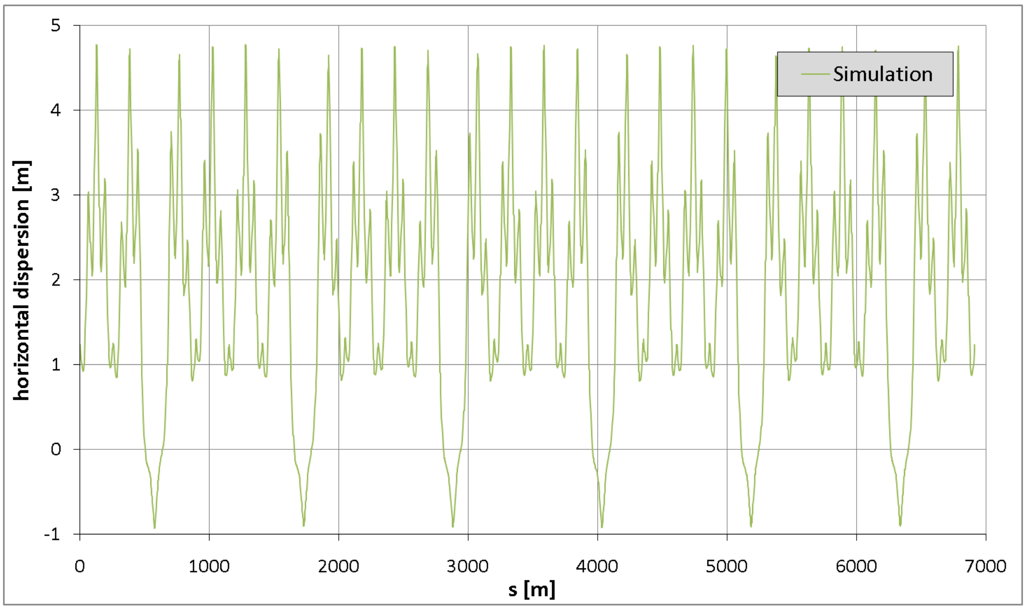

(a) Horizontal dispersion for nominal LHC-type beam ($Q_H = 26.13$).

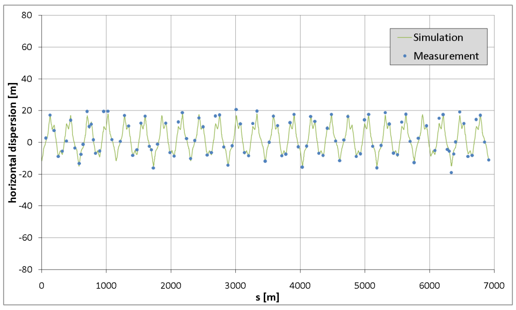

(b) $Q_H = 24.27$

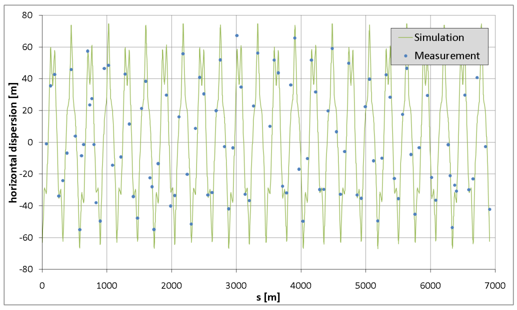

(c) $Q_H = 24.10$

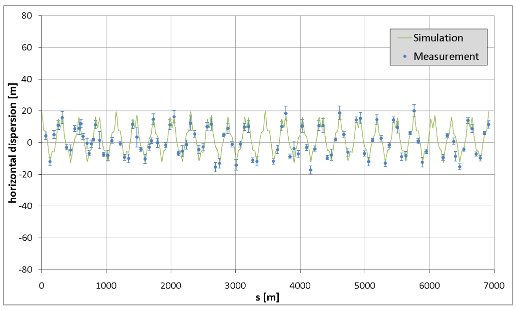

(d) $Q_H = 23.74$

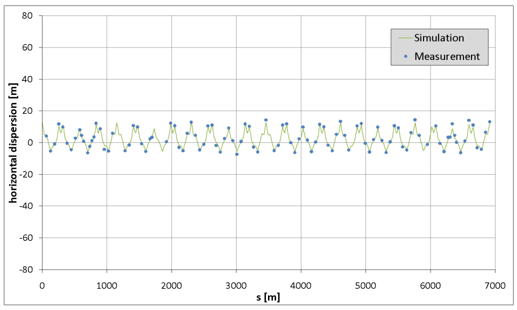

(e) $Q_H = 23.53$

Figure 3.6.: Horizontal dispersion for different horizontal tunes. In the vicinity of the $Q_H = 24$ tune resonance the dispersion is negative for large parts of the accelerator with a change of sign at $Q_H = 24$.
Measurement conditions: cycle: MD2, beam energy: 26 GeV, bunch intensity: $4 \cdot 10^{10}$ protons, 12 bunches.

The diverging behaviour is not limited to the linear part of the dispersion but higher order dispersion terms are resonant, too. Hence, the relevant terms need to be taken into account for the measurement of the linear dispersion[8]. Figure 3.7 shows the rms second order dispersion as function of horizontal and vertical tune.

3.1.3. Beta Beating Resonances

Quadrupolar field errors induce fluctuations of the beta function, so called beta beating (cf. section 2.2.3). The beta beating has a $\frac{1}{\sin(2\pi Q)}$ dependency (cf. Eq. 2.13) that leads to resonant behaviour for integer and half-integer tunes. A simulation of the dependency of the maximal beta functions on the tune is shown in Fig. 3.8. The resonant beta beating leads to an increased transverse beam size, which scales with $\sqrt{\beta}$ (cf. section 2.1). This dominates the beam losses at half-integer tune resonances. Since the closed orbit distortion (cf. Eq. 2.12) and the dispersion (cf. Eq. 2.11) also scale with $\sqrt{\beta}$, they are also influenced by the resonant beta beating.

3.1.4. Chromaticity Resonances

The negative natural chromaticity is corrected by sextupole magnets in order to reduce the tune spread and to avoid head-tail instabilities (cf. section 2.1.1). As calculated in [3, p. 297 ff.], the effect of the sextupoles on the tune Q is given by

$$\Delta Q_{H/V} = \left(\frac{1}{4\pi} \oint g_s(\bar{s}) \frac{\beta_{x/y}(\bar{s}) D_{x/y}(\bar{s})}{B\rho} \right) \frac{\Delta p}{p} = \xi_s \cdot \frac{\Delta p}{p} \tag{3.1}$$

where g_s denotes the second derivative of the sextupole magnetic field:

$$g_s = \frac{\partial^2 B_y}{\partial x^2}$$

β is the beta function (cf. section 2.1), D the dispersion, $\frac{\Delta p}{p}$ the momentum spread and $B\rho$ denotes the beam rigidity (cf. Eq. 2.2).

Since the chromaticity correction is proportional to the dispersion at the sextupoles (cf. Eq. 3.1), the resonant behaviour of the dispersion function (cf. section 3.1.2) at the tune resonance also implies a resonant behaviour of the chromaticity. The change of sign of the dispersion function at the resonance, given by $\frac{1}{\sin(\pi Q)}$ (cf. Fig. 3.6), leads to a negative chromaticity. This is reasonable, since a change of sign of the dispersion at a sextupole leads to an inversion of the dispersion orbit

[8] In this case the linear dispersion $D_x = D_x^1$ and the second order dispersion D_x^2 are determined from second order polynomial fits of the transverse beam position x as function of the momentum offset $\frac{\Delta p}{p}$. $x = x_0 + D_x^1 \cdot \frac{\Delta p}{p} + \frac{1}{2} D_x^2 \cdot \left(\frac{\Delta p}{p}\right)^2$.

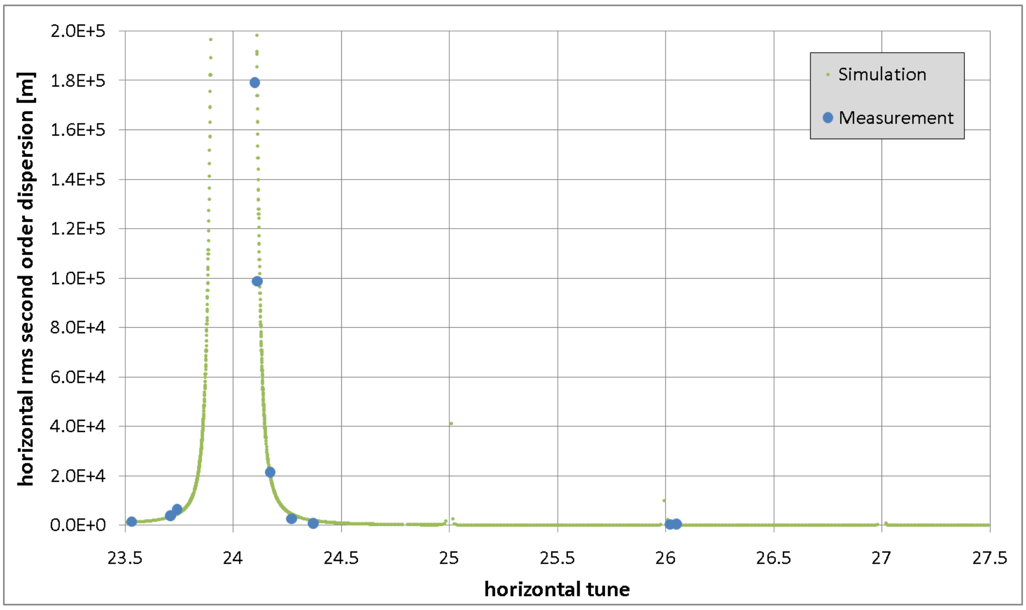

(a) Horizontal rms second order dispersion

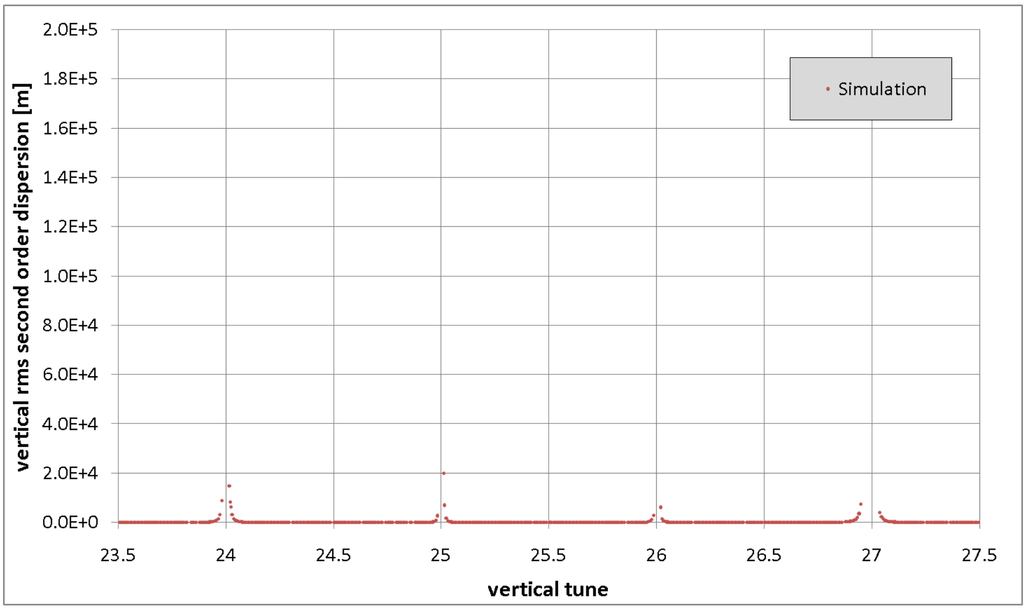

(b) Vertical rms second order dispersion

Figure 3.7.: Rms second order dispersion as function of the tune. Measurement conditions: cycle: MD2, beam energy: 26 GeV, bunch intensity: $4 \cdot 10^{9} - 4 \cdot 10^{10}$ protons, 12 bunches.

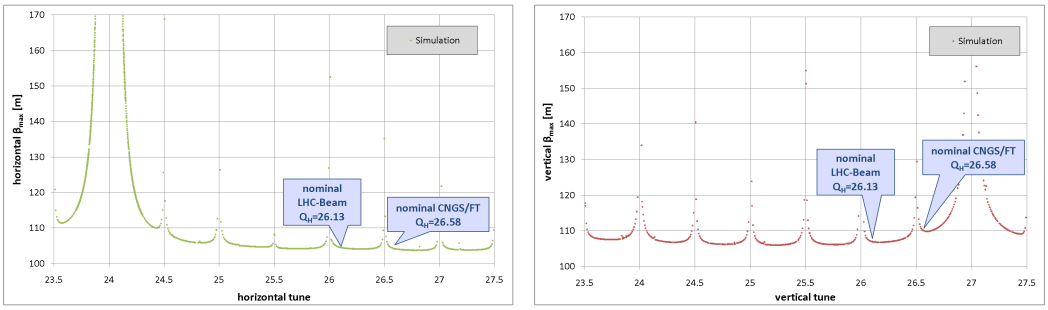

(a) Maximal horizontal beta function.

(b) Maximal vertical beta function.

Figure 3.8.: The beta functions diverge for integer and half-integer tunes.

and hence to an inverse effect of the chromaticity correction. Figure 3.9 shows the resonant behaviour of horizontal and vertical chromaticity[9]. The different behaviour of horizontal and vertical dispersion at the $Q = 24$ resonance (cf. Fig. 3.5) is well mirrored by the chromaticity.

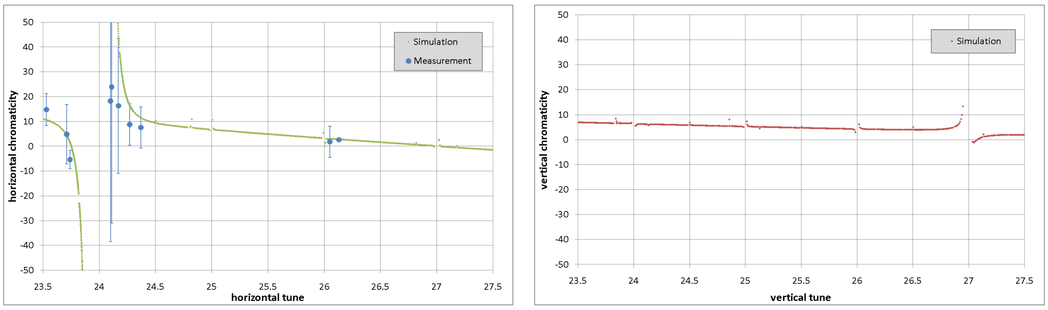

(a) Horizontal chromaticity as function of the horizontal tune.

(b) Vertical chromaticity as function of the vertical tune.

Figure 3.9.: Below the $Q_H = 24$ tune resonance the horizontal chromaticity is extremely negative due to the inverse effect of the chromaticity correction by sextupoles. This results in a large tune spread and beam instabilities. Measurement conditions: cycle: MD2, beam energy: 26 GeV, bunch intensity: $4 \cdot 10^9 - 4 \cdot 10^{10}$ protons, 12 bunches.

3.2. Superperiodic Resonances

The simulations and experiments on horizontal dispersion resonances (cf. section 3.1.2) and chromaticity resonances (cf. section 3.1.4) reveal extreme behaviour

[9] Like closed orbit and dispersion, also the natural chromaticity and sextupole chromaticity scale with the resonant beta function.

when the tune approaches the $Q = 24$ resonance. A similar behaviour can be observed for all superperiodic resonances, i.e. for integer tune values that are multiples of the sixfold symmetry of the SPS (cf. section 1.1). In contrast, the difference between superperiodic and normal integer tune resonances for closed orbit and vertical dispersion is much smaller.
How can the differences in the width of the resonances be understood? Especially, since closed orbit and dispersion have the same $\frac{1}{\sin(\pi Q)}$ resonance condition for all superperiodic and integer tune resonances (cf. section 2.1).

For the following explanation, the focus is put on the difference between superperiodic and normal integer tune resonances for dispersion and closed orbit. All other phenomena are similar to one of these cases.

3.2.1. Superperiodic Dispersion Resonance

Whereas the resonance condition for closed orbit distortion and dispersion are the same, the origins of both effects are different, accounting for the different resonance behaviour. The dispersion has its origin in *dipolar fields* that are dominated by the main bending fields that are distributed *periodically* around the accelerator. This leads to an extreme superperiodic dispersion resonance.

This can be analytically motivated by rewriting the integral in Eq. 2.11 as a sum over the superperiodic sectors:

$$\begin{aligned} D(s) &= \frac{\sqrt{\beta(s)}}{2\sin(\pi Q)} \oint_{s=0}^{C} \frac{1}{\rho(\bar{s})} \sqrt{\beta(\bar{s})} \cos\left(\psi(\bar{s}) - \psi(s) - \pi Q\right) d\bar{s} \\ &= \frac{\sqrt{\beta(s)}}{2\sin(\pi Q)} \sum_{i=0}^{p-1} \oint_{\frac{C}{p}i}^{\frac{C}{p}(i+1)} \frac{1}{\rho(\bar{s})} \sqrt{\beta(\bar{s})} \cos\left(\psi(\bar{s}) - \psi(s) - \pi Q\right) d\bar{s} \end{aligned} \tag{3.2}$$

where p is the number of superperiodic sectors ($p = 6$ for the SPS) and $\frac{C}{p}$ is the length of one sector.

Independent of the tune, $\rho(s)$ and $\beta(s)$ fulfill the superperiodic condition:

$$\begin{aligned} \rho(s) &= \rho(s + \frac{C}{p}i), \quad i = 0, \dots, p-1 \\ \beta(s) &= \beta(s + \frac{C}{p}i), \quad i = 0, \dots, p-1 \end{aligned} \tag{3.3}$$

At a superperiodic tune resonance, the betatron phase also fulfills the superperiodic condition (in case of the $Q = 24$ resonance, there are exactly 4 betatron oscillations per sector):

$$\psi(s) = \psi(s + \frac{C}{p}i), \quad i = 0, \dots, p-1$$

Consequently, the integral in Eq. 3.2 is the same for all sectors. And the dispersion can be expressed by

$$D(s) = p \cdot \frac{\sqrt{\beta(s)}}{2\sin(\pi Q)} \oint_{s=0}^{\frac{C}{p}} \frac{1}{\rho(\bar{s})} \sqrt{\beta(\bar{s})} \cos\left(\psi(\bar{s}) - \psi(s) - \pi Q\right) d\bar{s}. \tag{3.4}$$

This means that the contributions from each sector add up maximally and the total dispersion is p times the dispersion component from each sector.

In contrast, at normal integer tune resonances there is a phase advance of $2\pi \cdot \frac{i}{p}$, $i = 0, \ldots, p-1$ between the sectors. Thus, the integrals for the different sectors in Eq. 3.2 result in positive and negative values and mainly cancel out. As a result, a superperiodic dispersion resonance is much more pronounced than a normal integer tune resonance.

For $Q_H = 24$, there is an additional higher order symmetry: Since each sector of the SPS consists of 18 comparable FODO cells[10], there are exactly 2 complete betatron oscillations per 9 FODO cells. This even increases the strength of the $Q_H = 24$ tune resonance.

3.2.2. Superperiodic Closed Orbit Resonance

In contrast to the dispersion, the closed orbit distortion is generated by dipolar field *errors* (cf. Eq. 2.12). The dominant source for dipolar field errors in large particle accelerators are quadrupole misalignments [3, p. 292]. These misalignments are mainly distributed *randomly*, independent of the superperiodicity of the accelerator. Thus, for the closed orbit, the contributions from the different sectors are not the same at superperiodic resonances, since the dipolar field errors do not fulfill the superperiodic condition like the bending radius $\rho(s)$ (cf. Eq. 3.3). Consequently, there is to first approximation no special superperiodic behaviour of the closed orbit resonance.

In addition to randomly distributed dipolar field errors, there are systematic components. These result for example from internal magnet asymmetries due to the construction process. The systematic components lead (similar to the dispersion) to an enhanced superperiodic resonance.

As a result, the superperiodic $Q_H = 24$ closed orbit resonance, shown in Fig. 3.4a is broader than normal integer resonances, but far less pronounced than the superperiodic dispersion resonance shown in Fig. 3.5a.

[10] Apart from the long straight sections, there are 4 main bending magnets between two quadrupoles.

3.3. Chronological Distribution of Beam Losses

Experiments and MAD-X tracking studies have been done to understand the beam loss patterns of different equipment failure scenarios. A fast decrease of the quadrupole currents turned out to be especially threatening and is discussed in the following. Because of the very different beam dynamics for different tune resonances (cf. section 3.1), it is crucial to understand which tune resonances determine the beam losses.

3.3.1. MAD-X Tracking Studies

MAD-X tracking studies with a dynamic change of the quadrupole strengths were done. A detailed description of the tracking code is given in Appendix B.
Basically, three different types of loss patterns are observable for fast changes of the quadrupole strengths:

1. For tune changes of up to $\approx 3 \cdot 10^{-4}$ per turn (which corresponds to a relative decrease of the quadrupole strength of $\approx 1 \cdot 10^{-5}$ per turn) the beam is completely lost when reaching the $Q_H = 26$ integer resonance (cf. Fig. 3.10a).
2. When the tune decreases faster than $\approx 1.5 \cdot 10^{-3}$ per turn (which corresponds to a relative decay of all quadrupole strengths of $5 \cdot 10^{-5}$ per turn), the beam is able to partly cross the $Q_{H/V} = 26$ integer resonance with significant beam losses at integer and half integer tune resonances (cf. Fig. 3.10b).
3. For even faster tune decreases the beam losses are determined by the $Q = 24$ superperiodic tune resonance. Due to the extreme width of the superperiodic tune resonance (cf. section 3.2.1) the beam is lost well before the resonance maximum (cf. Fig. 3.10c).

3.3.2. Experimental Studies

In dedicated experiments, the tune was decreased with different slopes[11]. In an adiabatic approximation, i.e. the tunes are well defined and represent the particles motion at all times, the tunes can be deduced from the measured quadrupole

[11] The slopes of horizontal and vertical tune were the same. Since for LHC-type beam the nominal horizontal tune is lower and therefore reaches resonances earlier, the examples in the following discussion are only about the horizontal plane. It has to be kept in mind that the same effects also apply to the vertical plane.

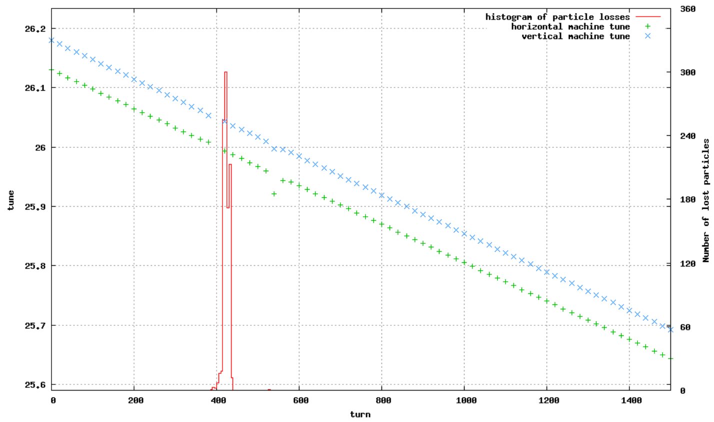

(a) relative decay of quadrupole strengths of $1 \cdot 10^{-5}$ per turn (tune slope $\approx 3 \cdot 10^{-4}$ per turn).

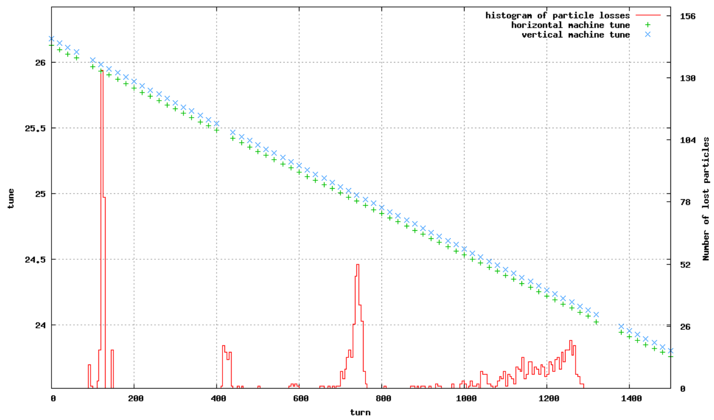

(b) relative decay of quadrupole strengths of $5 \cdot 10^{-5}$ per turn (tune slope $\approx 1.5 \cdot 10^{-3}$ per turn).

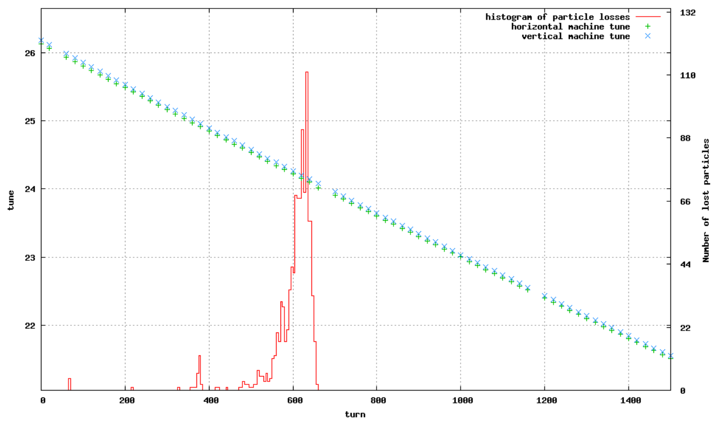

(c) relative decay of quadrupole strengths of $1 \cdot 10^{-4}$ per turn (tune slope $\approx 3 \cdot 10^{-3}$ per turn).

Figure 3.10.: Horizontal and vertical machine tune and a histogram of the particle losses. Depending on the slope of the tune, the integer tune resonances can be crossed. 1000 particles are tracked.

currents[12]. Figure 3.11 shows a typical loss pattern[13] for slow tune decreases. In accordance with the tracking studies (cf. Fig. 3.10a), the whole beam is lost within a few turns at the $Q_H = 26$ integer tune resonance.

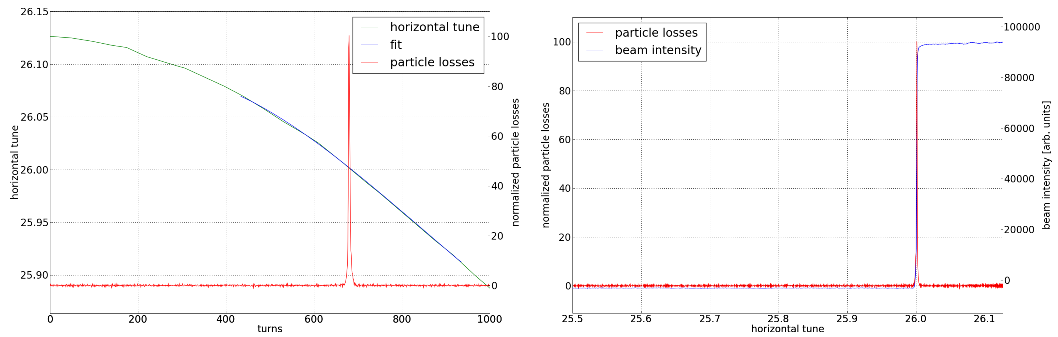

(a) (b)

Figure 3.11.: Typical beam loss pattern for a slow tune decrease. (a) shows the horizontal tune and particle losses as function of the turn after starting to decrease all quadrupole currents. The local 3rd-order polynomial fit is used to determine the slope of the tune at $Q_H = 26$. (b) shows the beam intensity and particle losses as function of the horizontal tune. The slope of the tune is $\approx 3.4 \cdot 10^{-4}$ per turn. The beam is lost within a few turns at the $Q_H = 26$ integer tune resonance.
Measurement conditions: cycle: MD1, beam energy: 26 GeV, bunch intensity: $\approx 1 \cdot 10^{10}$ protons, 12 bunches.

As predicted by the simulations (cf. section 3.3.1), the integer tune resonances can be crossed, when the tune slope exceeds a certain limit. Figure 3.12 shows the beam loss pattern for a tune slope of $\approx 1.4 \cdot 10^{-3}$ at the $Q_H = 26$ resonance. The loss spikes are clearly correlated with integer and half-integer tune values.

By measuring the tune at which the beam losses occur for different slopes of the tune at the $Q_H = 26$ resonance, a threshold slope beyond which resonance crossings become observable can be determined (cf. Fig. 3.13). At a beam energy of 26 GeV, the threshold slope for crossing the $Q_{H/V} = 26$ resonance is $1.0 \cdot 10^{-3} \pm 0.4 \cdot 10^{-3}$ which is in the predicted range of the tracking studies.

For higher beam energies, this threshold increases slightly. Experimental studies at 450 GeV showed that crossings of the $Q_H = 26$ resonance are not possible, even with a tune slope of up to $\approx 2.4 \cdot 10^{-3}$ per turn. Faster tune slopes are not achievable

[12] A linear calibration between tune and quadrupole currents yields sufficient results and gives an estimation of the tune with an absolute error < 0.1. Since the offset of the linear dependency is typically small, close to nominal tunes a proportional assumption is also reasonable.

[13] The particle losses are estimated from the turn-by-turn intensity data of the BPMs, since neither the BCTs nor the BLMs provide sufficient time resolution.

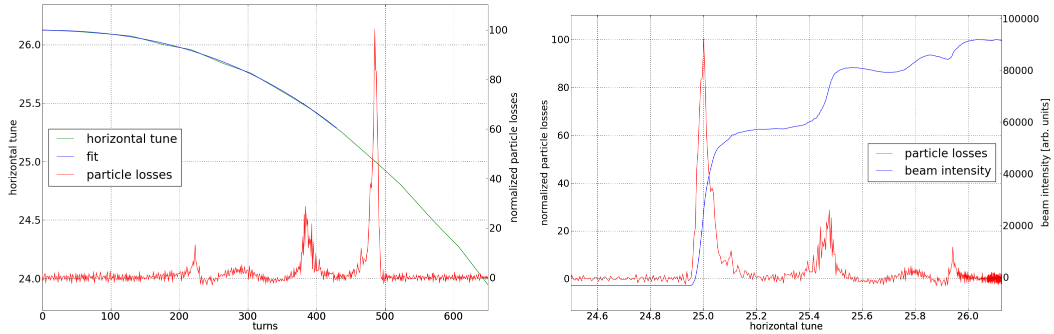

(a) (b)

Figure 3.12.: With a tune slope of $\approx 1.4 \cdot 10^{-3}$ per turn, the beam crosses the $Q = 26$ integer tune resonance. The beam losses occur at integer and half integer tunes.
Measurement conditions: cycle: MD1, beam energy: 26 GeV, bunch intensity: $\approx 1 \cdot 10^{10}$ protons, 12 bunches.

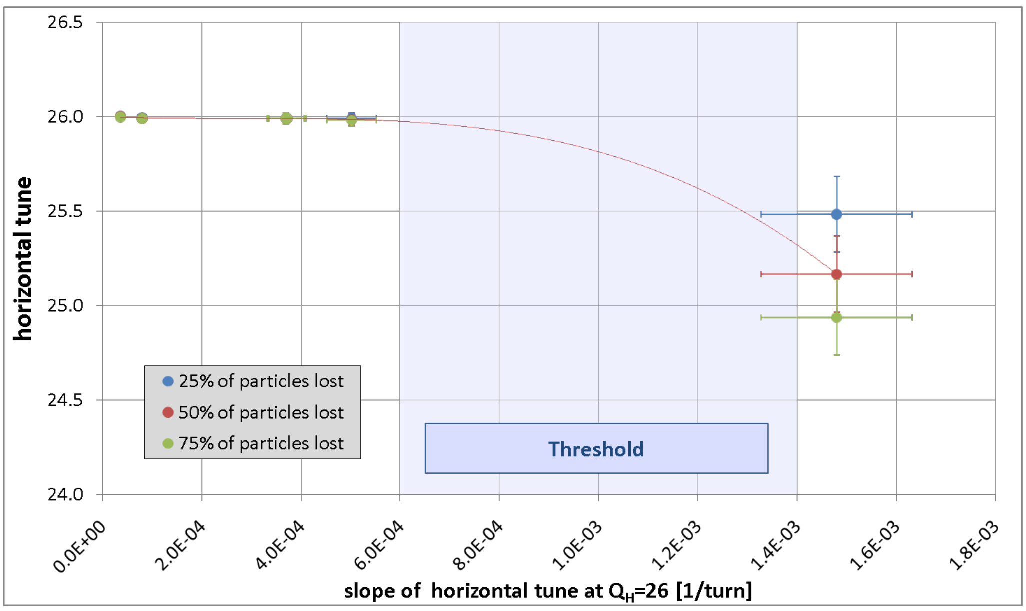

Figure 3.13.: The horizontal tune at which the beam intensity is decreased by 25%, 50% and 75% for different slopes of the horizontal tune at $Q_H = 26$. Above a threshold slope of about $1.0 \cdot 10^{-3} \pm 0.4 \cdot 10^{-3}$ a crossing of the $Q_{H/V} = 26$ resonance becomes possible. Below this threshold, the whole beam is lost at the $Q_{H/V} = 26$ integer resonance.
Measurement conditions: cycle: MD1, beam energy: 26 GeV, bunch intensity: $\approx 1 \cdot 10^{10}$ protons, 12 bunches.

due to the inductance of the circuits (cf. section 4.2).
It has also to be mentioned that the resonance crossings are very sensitive to small variations in the initial conditions, i.e. with same settings in the SPS there are large variations in the chronological distribution of the beam losses from one cycle to the other.

In any case, crossings of the $Q = 26$ integer tune resonance are always accompanied by extreme oscillations of the beam, as depicted in Fig. 3.2.

3.4. Spatial Beam Loss Pattern

The SPS has a non-uniform aperture. Focusing quadrupoles are enlarged in the horizontal plane, defocusing quadrupoles in the vertical plane. There are also two groups of main bending magnets (MBA and MBB) with different apertures, depending on the local beta functions. The global aperture is limited by special elements like collimators or the internal beam dumps. Table 3.1 gives an overview of the most important elements.

	Element	**Position**	**Half-Aperture HxV**	
		[m]	[mm] × [mm]	[σ] × [σ]
Main Elements	QF		76x19	21x12
	QD[14]		42x42	26x12
	MBA (close to QF)		71x17	21x8
	MBB (close to QD)		60x24	25x**7**
Special Elements	TIDP (Scraper)	456	41x15	**13**x8
	TIDH (Beam Dump)	573	55x27	16x16
	TIDV (Beam Dump)	603	43x20	24x**6**
	TCE (Collimator)	1692	65x24	37x7
	TPST (Collimator)[15]	1713	39x78	15x32
	TPSG (Collimator)[15]	4038	46x78	14x42
	TPSG (Collimator)[15]	6325	46x78	16x36

Table 3.1.: Half-aperture of the main elements and special aperture-limiting elements in mm and multiples of the beam size σ for nominal LHC-beam ($\epsilon_{H,V}^{n,1\sigma} = 3.5\mu m \cdot rad$) at injection energy (26 GeV).

[14] The defocusing quadrupoles in the injection and extraction region have an increased half-aperture of 76 mm in the horizontal and 46 mm in the vertical plane.

[15] The TPST and TPSG collimators are fixed to the septum girders and can be retracted together with the septum magnets if no extraction is needed.

3.4.1. MAD-X Tracking Studies

The MAD-X tracking studies on the chronological distribution of the beam losses (cf. section 3.3.1) also provide information on the spatial loss patterns. Figure 3.14 depicts a typical spatial beam loss pattern. Loss spikes can be seen at aperture limiting elements, but beam losses are also observable throughout the whole accelerator.

3.4.2. Experimental Studies

During the experimental studies on tune resonances the data from the beam loss monitors was constantly logged. Figure 3.15 shows the spatial beam loss pattern integrated over ≈ 700 accelerator cycles with tune changes towards and across different resonances. The beam loss pattern is dominated by a few special aperture limiting elements (cf. Table 3.1). For example the BLMs with the number 216-218 are in the long straight section 2, close to the TT20 slow extraction. Along with the extraction septum, the protection collimators (TCE.21695 and TPST.21759) limit the aperture and lead to increased beam losses.
Conspicuously high beam losses are observable at BLM 321-323 which were found to be related to an erroneous BPM[16].

Apart from the loss spikes, like predicted by the simulation (cf. Fig. 3.14), beam losses are observable throughout the whole accelerator. For example the beam loss pattern of the 2008 incident (cf. Fig. 1.5) is spread very wide with small peak beam losses. This is typical for beam losses that are restricted to the vertical plane (cf. Fig. 3.14b), because especially the B-type main bending magnets have a very small vertical aperture of only $7\,\sigma$ at injection (cf. Table 3.1). In accordance with that, the vacuum chamber of the B-type magnet MBB.12530 was damaged during the 2008 incident.

This shows that there is not always a clear beam loss hierarchy. The margin between aperture limit and protection devices is too small and not the whole phase space is covered, which underlines the need of an a priori protection against beam losses due to fast tune changes.

[16] The influence of a time dependent local three-corrector orbit bump on the beam losses and the beam current was investigated. It was found that the vertical beam position monitor (BPV.32108) close to the beam loss monitor BLM 321 is erroneous. The readout from this BPM does not react on the orbit bump in a significant way. A bad local orbit is expected to be accountable for the increased beam losses.

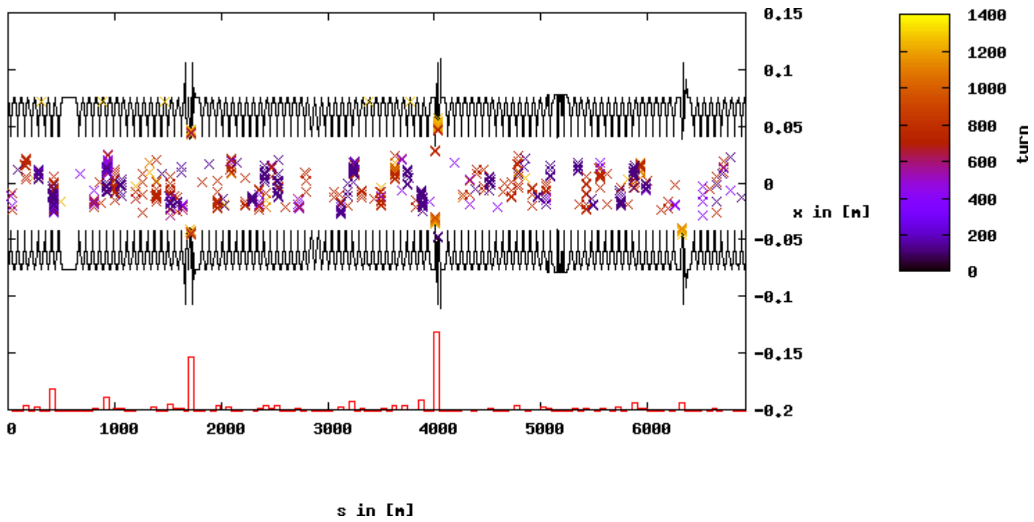

(a) horizontal plane

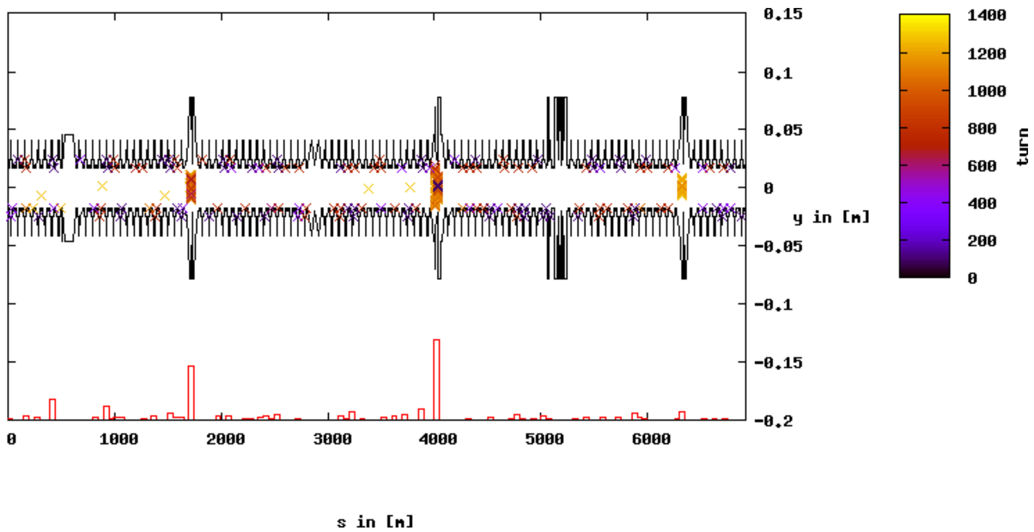

(b) vertical plane

Figure 3.14.: Spatial beam loss pattern of 1000 tracked particles. The crosses indicate the positions where the particles exceed the aperture (in black) for the first time. Crosses within the aperture limit are related to beam losses in the other plane. The color coding indicates the turn of the particle losses after the start of the simulation. A red histogram below the aperture indicates the amount of particles lost at the corresponding position.
The tracking conditions are the same as in Fig. 3.10b.

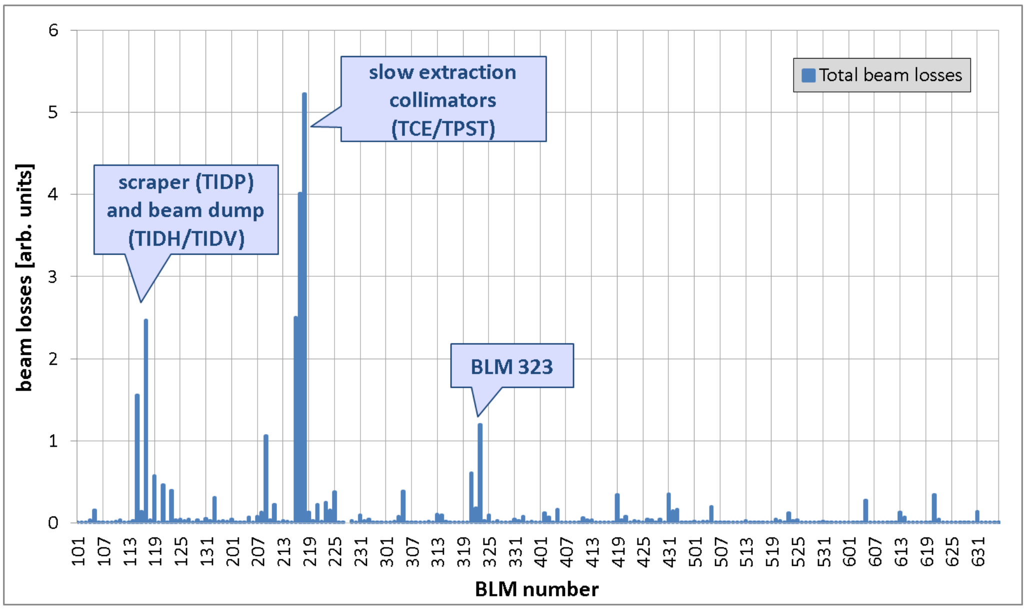

Figure 3.15.: Integrated beam loss pattern of ≈ 700 fast tune decrease failure scenarios. The aperture limiting scraper, collimators and beam dump dominate the spatial beam loss pattern.
Measurement conditions: cycle: LHCFAST2,
beam energy: $26 - 450\,\mathrm{GeV}$,
bunch intensity: $\approx 1 \cdot 10^{10}$ protons, 12 bunches.

4. Review of present Machine Protection Systems

Against the background of the studies on beam dynamics at tune resonances (cf. chapter 3), the machine protection systems (cf. section 2.3) of SPS and LHC were reviewed. In this chapter, the results of crucial tests are presented and vulnerabilities of the systems are discussed.

4.1. SPS BLM System

The ring-type BLMs (BLRING) with their reaction time of $\approx 20\,\text{ms} = 870\,\text{turns}$ (cf. section 2.3.2) are by orders of magnitude too slow to provide any protection against fast failures with complete beam losses in as little as 3 turns.
Only the very fast extraction type BLMs (BLD) have an adequate reaction time of less than one turn. Nevertheless, the complete beam dump procedure always takes at least one turn. For high energy beams, already the fraction of the beam that can be lost in this small time interval has a vast damage potential.
Furthermore, extraction type BLMs are only located in LSS1, LSS2, LSS4 and LSS6 (cf. section 2.3.2). For beam losses in the horizontal plane, these positions coincide with the peaks of the spatial beam loss pattern (cf. section 3.4). In contrast, beam losses that are limited to the vertical plane do not have this clear hierarchy but occur anywhere in the accelerator (cf. Fig. 3.14b). Therefore, the fast extraction type BLMs do not provide an adequate protection against beam losses in the vertical plane.

4.2. SPS Power Converter Interlock

As explained in chapter 3, fast tune shifts can lead to particularly dangerous beam loss scenarios. In the SPS, the main magnet circuits are protected by a fast interlock on internal failures of the power converters (cf. section 2.3.2). In October 2009,

dedicated experiments concerning the behaviour of the main bend and quadrupole currents and the reaction time of the power converter interlock in the case of a real failure were done. To simulate the worst case scenario, the power supply of the power converters was interrupted abruptly (without beam in the machine). This was done at currents corresponding to a particle momentum of 14 GeV/c and 400 GeV/c.
Figure 4.1 shows the current decay of a quadrupole circuit ramped to 400 GeV/c and the delay of the power converter interlock (cf. Appendix C for other circuits and test conditions).
Table 4.1 summarizes the total reaction time of the interlock system for the different circuits and the relative decays of the currents until the interlock. The data is totally consistent with data from similar experiments done in May 2007 and May 2008 ([20], [21]).

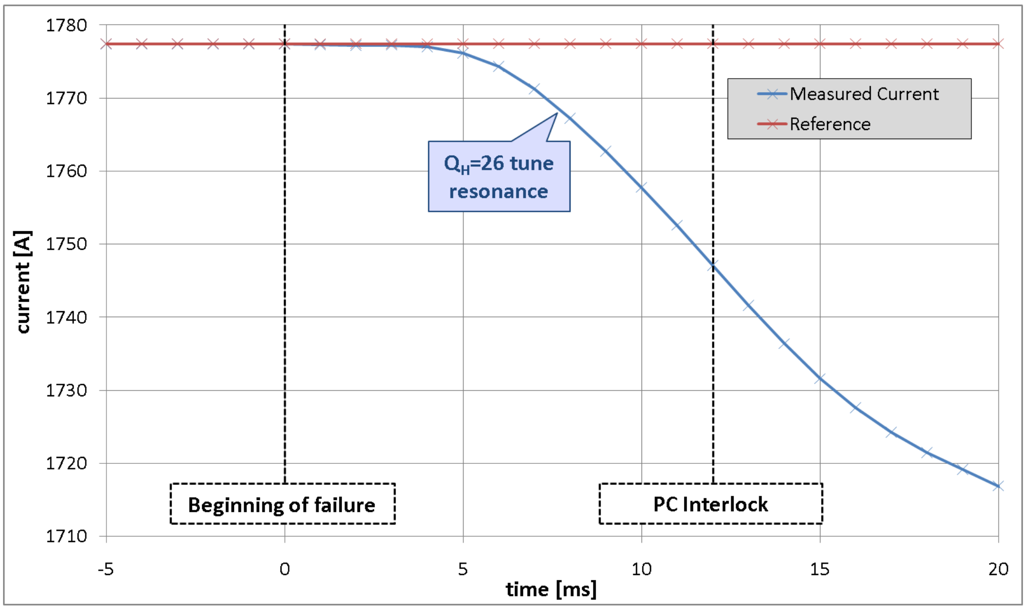

Figure 4.1.: Test of the power converter interlock of the focusing quadrupole circuit QF1[1]. The circuit is ramped to a current corresponding to a particle momentum of 400 GeV/c, then the power supply is abruptly interrupted. The beam dump signal is sent by the power converter interlock with 12 ms delay. The $Q_H = 26$ integer tune resonance would be reached after $7.7^{+0.4}_{-0.5}$ ms.

[1] For historical reasons, there are two independent main focusing quadrupole circuits (QF1, QF2) in the SPS, each powering the magnets in one half of the ring.

Circuit	**Momentum** [GeV/c]	**Interlock delay** [ms]	**Rel. current decay** [%]	**Tune shift**
Main Bend	400	8	0.527	-0.17 (Q_H)
QD	400	12	1.705	-0.45 (Q_V)
QF	400	12	1.718	-0.45 (Q_H)
Main Bend	14	7	0.782	-0.26 (Q_H)
QD	14	8	6.809	-1.78 (Q_V)
QF	14	8	6.944	-1.81 (Q_H)

Table 4.1.: Total reaction time of the SPS power converter interlock (cf. section 2.3.2) after fast failures of the power converters (abrupt interruption of the power supply), the relative decay of the currents until the interlock and the associated tune shift. For the main bend and the focusing quadrupole (QF) circuit, mainly the horizontal tune Q_H is shifted, for the defocusing quadrupole (QD) circuit, the vertical tune Q_V is shifted. The tune shift of the main bend circuit is calculated using the natural chromaticity of -33. Since the values for the two separate circuits QF1 and QF2 are very similar, only the mean values are given (QF).

The decay of the main bend current leads in general to a deceleration of the beam by the RF which keeps the orbit centered[2]. Due to the chromaticity, the decay of the main bend current results in a tune shift of up to $-33 \cdot 0.527\,\% = -0.17$ at 400 GeV and $-33 \cdot 0.782\,\% = -0.26$ at 14 GeV[3]. For nominal LHC-type beam, this leads to a tune shift towards the $Q_H = 26$ resonance and associated beam losses. For CNGS and fixed target beam an integer resonance cannot be reached, since the nominal tunes are further away (cf. Table 2.1).
The decay of the quadrupole currents leads to a horizontal and vertical tune shift. At 14 GeV the relative decay of up to 6.944 % leads to a large horizontal tune shift of up to $\approx 26.13 \cdot (-6.944\,\%) = -1.81$. The values of the vertical tune shift associated to the current decay of the quadrupole circuits are also shown in Table 4.1.

[2] In case of an RF failure or coasting beam, the decay of the main bend current leads to a horizontal orbit shift. With a maximal nominal dispersion of $D_x \approx 5\,\text{m}$, the orbit is shifted by maximal $5\,\text{m} \cdot 0.527\,\% = 26\,\text{mm}$ at 400 GeV and $5\,\text{m} \cdot 0.782\,\% = 39\,\text{mm}$ at 14 GeV. In all points, the closed orbit shift itself is still within the horizontal aperture of the SPS. The momentum aperture of the SPS is about 1 %.

[3] It is assumed that the chromaticity has its natural value of -33. This is the worst case scenario. During normal operation the chromaticity is corrected to be slightly positive, i.e. the associated tune shift is positive and about one order of magnitude smaller.

From the measured currents, the time till the $Q_{H/V} = 26$ resonance is reached and the slope of the tune at the integer tune resonance can be estimated[4]. The results (cf. Table 4.2) show that for every failure case the integer tune resonance is reached before the power converter interlock sends the beam dump signal. It is too slow to provide an adequate machine protection against fast equipment failures.

Circuit	**Momentum** [GeV/c]	**Interlock delay** [ms]	**Time till** $Q_{H/V} = 26$ [ms]	$Q'_{H/V}$ **at** $Q_{H/V} = 26$ [$1/turn$]
Main Bend	400	8	$6.8^{+0.2}_{-0.2}$	$(-8.7)^{+0.1}_{-0.1} \cdot 10^{-4}$
QD	400	12	$8.5^{+0.5}_{-0.6}$	$(-1.5)^{+0.2}_{-0.2} \cdot 10^{-3}$
QF	400	12	$7.7^{+0.4}_{-0.5}$	$(-1.4)^{+0.3}_{-0.2} \cdot 10^{-3}$
Main Bend	14	7	$3.7^{+0.4}_{-0.4}$	$(-8.6)^{+0.4}_{-0.1} \cdot 10^{-4}$
QD	14	8	$1.7^{+0.2}_{-0.2}$	$(-3.4)^{+1.6}_{-0.3} \cdot 10^{-3}$
QF	14	8	$1.3^{+0.2}_{-0.2}$	$(-3.2)^{+1.2}_{-0.7} \cdot 10^{-3}$

Table 4.2.: Total reaction time of the SPS power converter interlock, the time till the $Q_{H/V} = 26$ integer resonance is reached and the slope of the tune at the resonance. The data given for the main bend and the QF circuits correspond to the horizontal tune, the data for the QD circuit corresponds to the vertical tune. For the main bend circuit the tune is estimated from the current using the natural chromaticity of the SPS of -33. For the quadrupole circuits the tune is assumed to be proportional to the corresponding current. Since the values for the two separate circuits QF1 and QF2 are very similar, only the mean values are given (QF).

The large slopes of the tune at the $Q_{H/V} = 26$ integer resonance (especially in case of a quadrupole failure) are above the threshold of about $1 \cdot 10^{-3}$ per turn found in experiments and simulations (cf. section 3.3). This indicates that at least parts of the beam are able to cross the $Q_{H/V} = 26$ integer tune resonance and are lost at lower tune resonances. In any case the beam is strongly excited when crossing the integer resonance and significant orbit oscillations are observable.

4.3. LHC Failure Scenarios

In the LHC, the main circuits are superconducting, i.e. they have relatively long decay times. The related machine protection is ensured by the *Powering Interlock*

[4] A proportional relation between quadrupole currents and tunes is assumed.

System [22] and in case of beam losses by the BLM system.
Regarding fast failures, most critical are the normal conducting circuits. Particularly, a failure of the warm quadrupoles in the collimation region can lead to fast tune changes that are not intercepted by the normal powering interlocks. Against the background of dedicated failure studies ([23], [24]), FMCMs (cf. section 2.4) are installed to detect fast current changes of the circuits of the separation dipoles, the warm quadrupoles and the compensator dipoles for the Alice spectrometer [18, p. 42].
During the LHC commissioning phase, tests to verify the performance of the FMCMs have been done. The results are presented in the following section.
An analysis of similar failure scenarios revealed a vulnerability to an unsynchronized powering of the main dipole circuits. The issue and the implemented countermeasures are explained in section 4.3.2.

4.3.1. FMCM Tests

In the LHC, the main quadrupoles in the collimation regions are normal conducting. There are in total four normal conducting main quadrupole circuits, each monitored by a FMCM. In March 2010 the performance of the FMCM of the circuit RQ4.LR3 was tested.
With two low intensity beams ($\approx 6 \cdot 10^9$ protons) in the machine, the circuit was switched off manually. The failure was detected by the FMCM with a delay of 12 ms and the beam was dumped[5]. No beam losses or changes of the beam dynamics are measureable until the beam dump.
To illustrate the necessity of the FMCMs, the test was repeated with deactivated (masked) FMCM interlock channel (cf. Fig 4.2). Again, the failure was detected by the FMCM with a delay of 12 ms. From the post mortem data of the FMCM, the relative current change in this time interval is determined[6] to be about 0.11 %. Simulations show that the associated absolute tune change is only $-4.3 \cdot 10^{-4}$ for the horizontal tune and $-4.8 \cdot 10^{-4}$ for the vertical tune.
First beam losses are measureable 50 ms after the failure. Since the test is done with low beam intensity, the beam losses do not exceed the BLM thresholds. The beam is finally dumped with a delay of 662 ms by an interlock on the beam position[7].

[5] Post mortem timestamp: 10/03/2010 13:40:24.
[6] The calculated change of the magnetic field is given in the post mortem data with a time resolution of 50 μs. To determine the current, this data is linearly calibrated with the current measurement which has a time resolution of 20 ms.
[7] Post mortem timestamp: 10/03/2010 13:52:56.

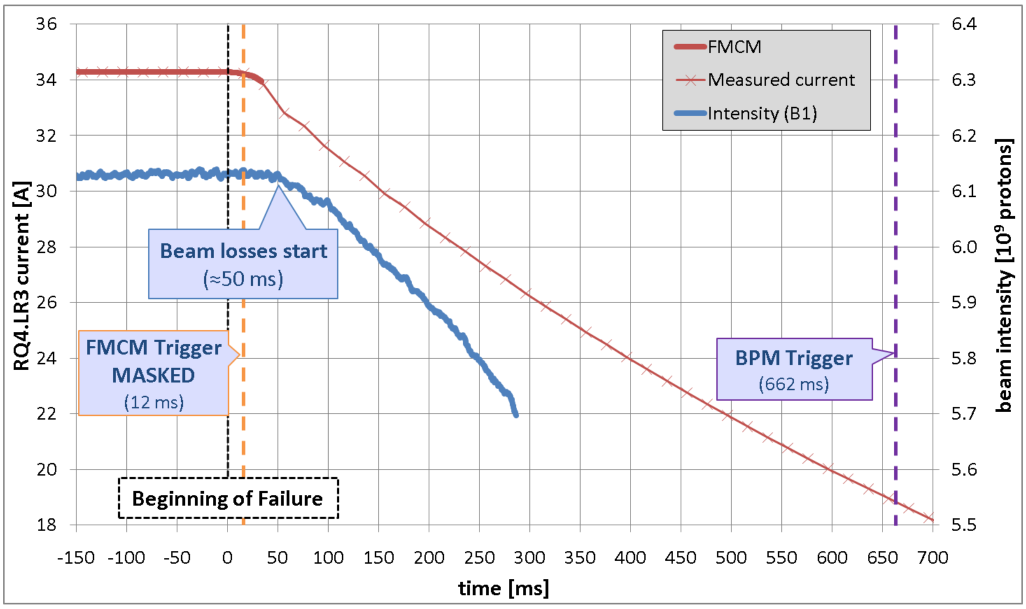

Figure 4.2.: Failure of normal conducting quadrupole circuit RQ4.LR3. The post mortem data from the FMCM is used to increase the time resolution of the current measurement to 50 μs. The (masked) FMCM detects the failure after 12.03 ms, beam losses start after $\approx$ 50 ms, the beam is finally dumped after 662 ms by the beam excursion interlock.
Measurement conditions: beam energy: 450 GeV,
bunch intensity B1: $\approx 6 \cdot 10^9$ protons, single bunch,
bunch intensity B2: $\approx 6 \cdot 10^9$ protons, single bunch.

The test shows the excellent performance of the FMCM. 38 ms (= 427 turns) before beam losses are measureable, the failure is detected and the beam is dumped. Similar tests with the FMCMs of the separation dipoles also yield very good results ([25], [26]).
Due to the FMCMs and the slow decay time of the superconducting circuits, the vulnerability of the SPS against fast power converter failures does not apply to the LHC.

4.3.2. Inconsistent Main Dipole Circuit Settings

The main dipole magnets in the LHC are powered by 8 independent superconducting circuits. The state of single circuits can be manually changed, e.g. the current of one of the main dipole circuits can be changed, the circuit can even be switched off. This operation is not interlocked by the Powering Interlock System.
The resulting effect of an inconsistently powered main dipole circuit is shown in Fig. 4.3. The current of the dipole circuit of sector 45 is reduced by 1 %. Consequently, the horizontal position has an offset of up to 21 mm (arc aperture = 22 mm). This powering failure can be treated as a momentum offset in this sector. Since the dispersion is suppressed to zero at the end of every sector (cf. Fig. 4.3), the effect is restricted to this particular sector. The beam excursion interlock in IR6 will not detect the failure and the beam loss hierarchy is not maintained. Tracking studies show that the beam losses occur in cold quadrupoles in the arc, and not in the collimation regions in IR3 and IR7 (cf. Fig. 4.4).

To counteract the vulnerability, two new interlocks are implemented in the Software Interlock System[8] that are processed with a frequency of 0.5 Hz:

1. **Energy interlock:** The calculated beam energy from the main dipole circuits is compared to the beam energy that is distributed via the Master Timing Generator. If the differences are larger than 0.2 % (1 % during the ramp) the beam is dumped [27].

2. **Position interlock:** If the position measurements of more than 10 BPMs exceed the individual thresholds of $\pm 1.5 - 2.0$ mm (depending on BPM location and beam mode) the interlock is triggered. The values correspond to an energy offset of ≈ 0.1 %.

[8] Under responsibility of J. Wenninger.

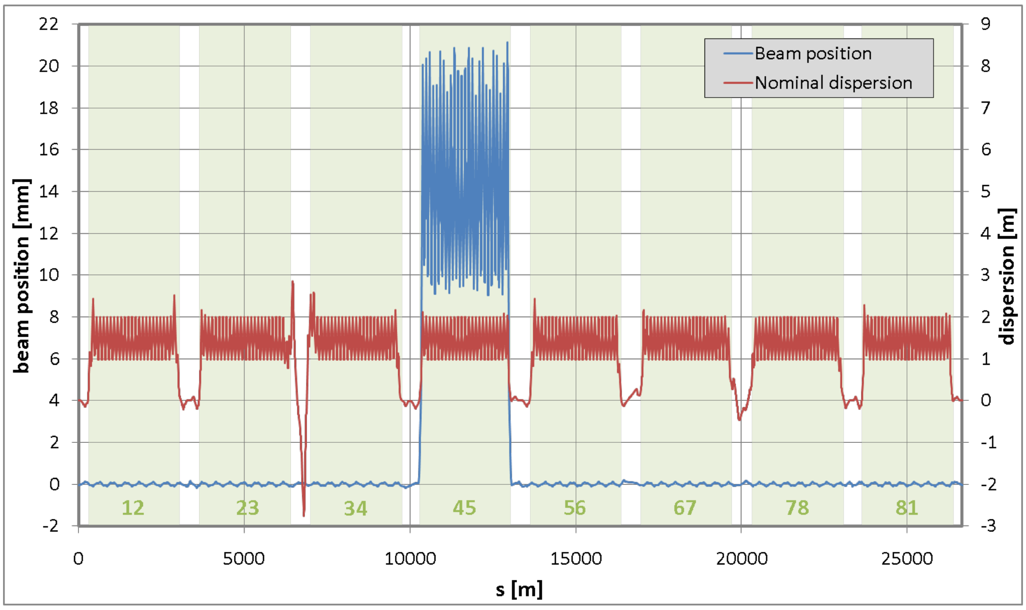

Figure 4.3.: Simulated beam position for a change of the current of the main dipole circuit of sector 45 by $-1\,\%$ and the nominal dispersion.

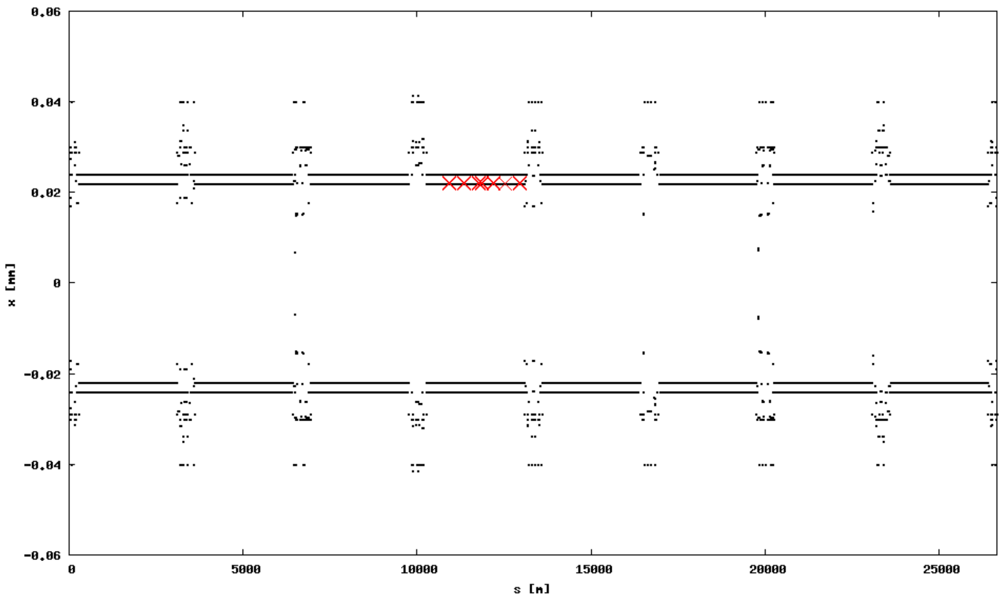

Figure 4.4.: Spatial beam loss pattern of 1000 tracked particles. The strength of the main dipole magnets in sector 45 is linearly reduced by $-2\,\%$ in 1000 turns. All particles are lost after 516 turns. The red crosses indicate the positions where the particles exceed the aperture (in black) for the first time. The loss positions coincide with the positions of the focusing quadrupoles.
The simulation is done at injection energy with $\epsilon^{n,1\sigma}_{H/V} = 3.5\,\mu\mathrm{m}\cdot\mathrm{rad}$.

5. New SPS Position Interlock System

The delay of the current interlock systems of the SPS is too large to provide an adequate machine protection against fast failures (cf. section 4.2). Therefore, a new beam position interlock system is designed to counteract the vulnerability of the SPS. It is based on a new position acquisition hardware to overcome the limitations given by the present MOPOS hardware (cf. section 2.3). The new interlock system combines a fast (turn-by-turn) position interlock and the beam position extraction interlock. The system is currently in the commissioning phase and is planned to become operational in the second half of 2010.

5.1. General Description

The experimental studies (cf. chapter 3) showed that in the vicinity of an integer tune resonance the beam position starts to oscillate typically 30 turns before beam losses are measurable. Based on this, a new fast beam position interlock system will counteract the vulnerability of the SPS. For the reaction time of the system, it has to be taken into account that during a fast power converter failure the tune can decrease about 2 times faster than what was achievable in beam based experiments (cf. Table 4.2 and Fig. 3.13). This sets an upper limit of the total reaction time to a few turns, i.e. the acquisition of the beam position and the interlock processing must be done directly in the hardware, preferably on a turn-by-turn base.
The system also provides a new robust extraction interlock on the beam position which replaces the old system (cf. section 2.3.3) to increase the operational flexibility.

The hardware of the new beam position acquisition and interlock system was designed in 2008 and 2009 by T. Bogey and J. Savioz et al ([28], [29]). The communication with the hardware is done by a middleware software class called *BPMINT* (under the responsibility of B. Araujo Meleiro), based on the *Front End System Architecture* (FESA) framework. For operational applications, the control room software *Moin Moin* was developed in the course of this thesis (cf. Appendix D).

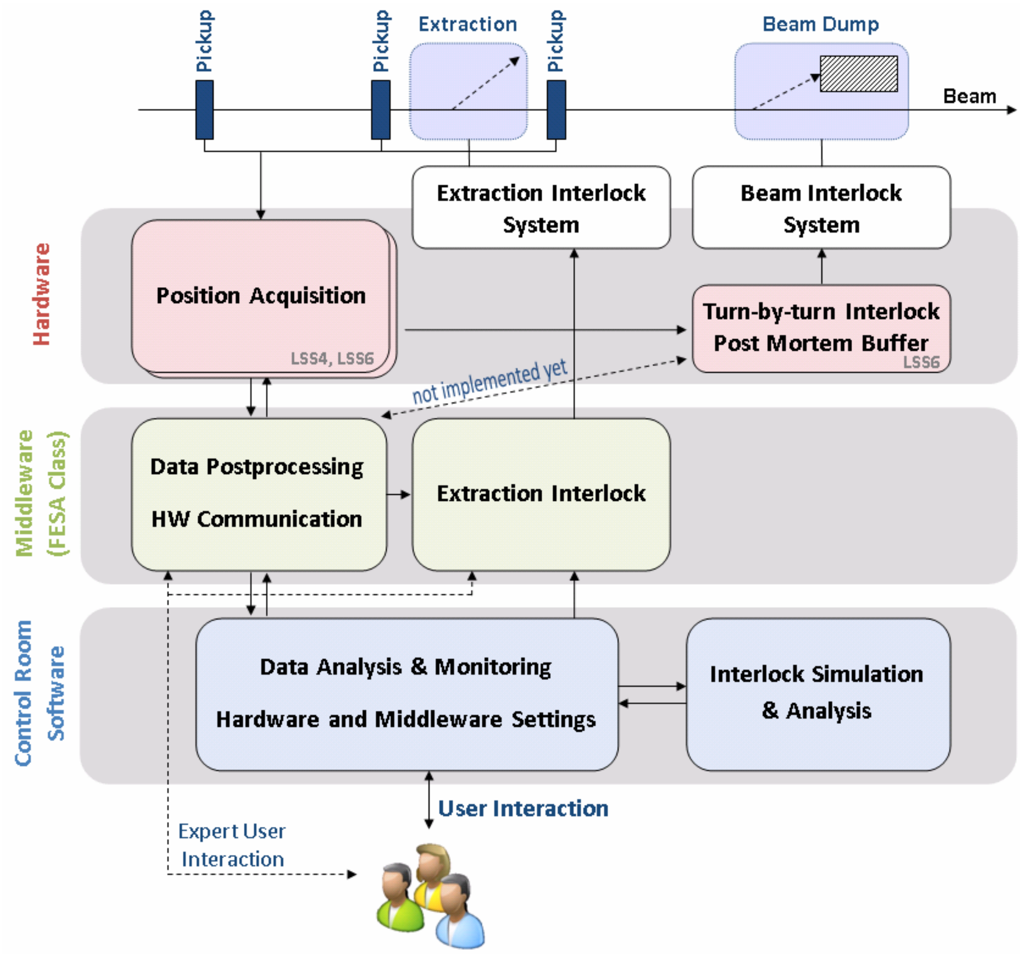

Figure 5.1.: Layout of the new position acquisition and position interlock system. The turn-by-turn position interlock is processed in the hardware, the extraction interlock by the middleware software. The control room software provides the user interface including an analysis module.

The layout of the complete system is illustrated in Fig. 5.1 and explained in the following sections.

5.1.1. Position Acquisition

In total six stripline coupler BPMs with a half-aperture of 110 mm in the extraction regions of LSS4 and LSS6 are used. With a phase advance of $\approx 45°$ between two BPMs, the whole phase space is covered (cf. Table 5.1).

The acquisition hardware is not gated by the RF signal but has an internal trigger on the bunch intensity. It utilizes logarithmic amplifiers that allow reliable measurements in a large intensity range, but are accompanied by increased nonlinearities when measuring large position offsets (cf. section 5.2). The hardware acquires position and intensity data on a turn-by-turn basis for about 1800 turns ($\approx$ 41 ms). An

	Name	Position in $[m]$	Betatron phase for $Q = 26$
LSS4	BPCE.417(05)	3998.8	0.0°
	BPCE.418(01)	4029.5	47.8°
	BPCE.419(31)	4067.7	100.2°
LSS6	BPCE.617(05)	6302.6	240.2°
	BPCE.618(05)	6334.6	288.1°
	BPCE.619(31)	6371.5	339.0°

Table 5.1.: Longitudinal position of the six pickups used for the new position interlock system. The position is chosen close to the quadrupoles in a way such that the betatron phase advance between two pickups is about 90° with one pickup in between. The betatron phase is calculated relative to BPCE.417 assuming a tune of $Q = 26$. Each BPM is capable of measuring horizontal and vertical beam position independently.

average closed orbit position is calculated via the hardware implementation of an *Infinite Impulse Response* (IIR) filter.
The acquisition is initiated, postprocessed (data calibration, etc.) and published by the BPMINT FESA class. The start time of the acquisition can be chosen relative to SPS timing events.
The control room java application provides an intuitive user interface for standard data analysis and monitoring as well as setting of acquisition hardware properties.

5.1.2. Turn-by-turn Interlock

Each turn ($23\,\mu$s) a *Field-Programmable Gate Array* (FPGA) does the interlock processing. It triggers the beam dump via a direct connection to a Beam Interlock Controller in case the beam position at a single BPM exceeds its threshold. The system uses the BPMs in LSS6. It is designed to replace the analog 30 mm-interlock (cf. section 2.3.2). The current interlock implementation has adjustable positive and negative thresholds for each of the three BPMs.
The control room software has an analysis module to simulate and analyze different interlock scenarios, especially in order to prove and optimize the efficiency of the interlock algorithm.
For post analysis, it is planned that a post mortem buffer stores the data of all three BPMs of the last 1000 turns. The buffer is frozen when a beam dump request is sent by the system. The data is automatically transfered and stored in the logging data base.

5.1.3. Extraction Interlock

The new position interlock for the extraction to LHC and CNGS target is processed by the middleware software. It inhibits the extraction, if the average orbit (calculated by the IRR filter) is for a single BPCE outside of its individual reference window. Optionally, the average orbit can be calculated from the turn-by-turn position data by the middleware software. The processing is done before each extraction. The total processing time for the extraction interlock is about 1.5 ms.

5.2. Commissioning of the Position Acquisition

The first in situ tests of the new system were available in beginning of October 2009. Dedicated experiments concerning the reliability of the position measurements were done and many issues encountered. Three important aspects are addressed in the following sections, an overview of the most important issues is given in Appendix E. A set of necessary tests and measurements for the final commissioning is defined in section 5.2.3.

5.2.1. New Hardware vs. MOPOS Hardware

The pickups used by the new system are also connected to the standard MOPOS hardware. For the horizontal position of the BPMs BPCE.617.H and BPCE.619.H and the vertical position of BPCE.618.V large discrepancies between the position measurements of the two systems were observed[1]. The differences are almost proportional to the measured positions with proportionality factors of about +30 %, −30 % and −40 %, respectively (cf. Appendix F). Errors of this size are absolutely unacceptable for an adequate position interlock.

3π orbit bumps showed that the MOPOS data of the corresponding BPMs is not consistent with the MOPOS data of other pickups. Conspicuously, inconsistencies are only observable for the pickups at low beta functions[2]. Since the MOPOS position measurements of the other pickups are consistent, the bump amplitude at the conspicuous BPMs can be fitted from the position measurement of the pickups at maximal beta function. Figure 5.2 shows a simulated horizontal 3π orbit bump with

[1] For the new hardware the average position over ≈ 1800 turns as calculated by the FESA class is used. The MOPOS data is acquired using the program *YASP* and the *orbit* acquisition option.

[2] Usually the horizontal and vertical pickups are separated in the SPS. The pickups are positioned at the corresponding positions of high beta functions. The BPCE coupler BPMs in the extraction regions also have pickups at low beta functions.

an amplitude of 1 mm at BPCE.617.

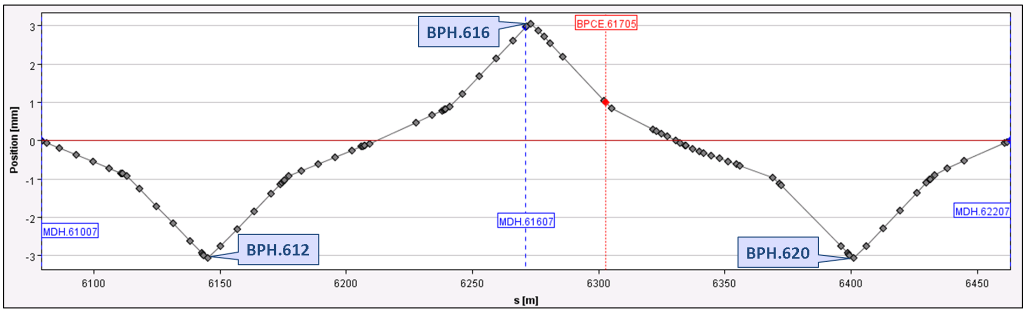

Figure 5.2.: A simulated horizontal 3π orbit bump with an amplitude of 1 mm at BPCE.617. The real amplitude can be fitted from the position measured by the BPMs BPH.612, BPH.616 and BPH.620.

In Fig. 5.3 the nominal trim, the position measured by the new hardware and the MOPOS hardware are compared. The difference to the fitted bump amplitude which is treated as reference is shown. The nominal trimmed amplitude is within an error of a few percent in all cases consistent with the fitted amplitude. The difference between the position measured by the new hardware and the fitted bump amplitudes is almost proportional to the fitted bump amplitude and does not exceed 11 %. In contrast to the new hardware, there is a huge difference between the single BPM position measurement by the MOPOS hardware and the fitted bump amplitude: $-14\,\%$, $+76\,\%$ and $+60\,\%$, respectively[3].

Since the fitted amplitude is also taken from MOPOS data, there is an obvious inconsistency in the MOPOS measurements. On the other hand, the nominal trimmed amplitudes, the fitted bump amplitudes and the positions measured by the new hardware are totally consistent. This underlines the reliability of the new hardware. From these measurements the systematic error of the new hardware can be estimated to be about 10 %. This is much more than the statistical error which is about $0.3\,\% + 50\,\mu$m for the turn-by-turn position measurement of nominal CNGS-type beam.
Due to radiation problems with the hardware, the tests have not been done for the BPMs in LSS4, yet.

5.2.2. 400Hz Oscillations

The new position acquisition hardware measures huge oscillations of the turn-by-turn beam position. The oscillations have a peak-to-peak amplitude of up to 20 mm

[3] These values are consistent with the measured differences between MOPOS and new hardware, given in Appendix F.

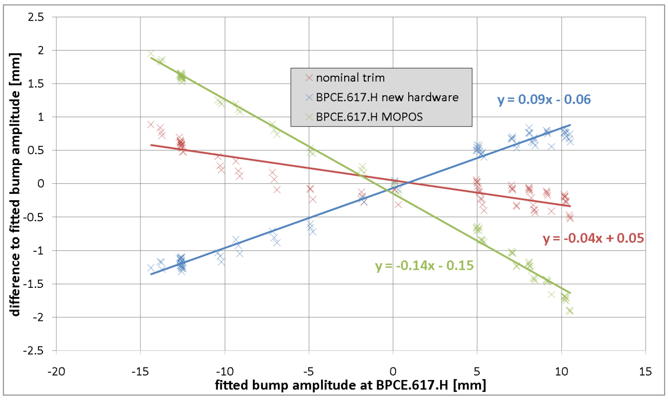

(a) Horizontal position measurement of BPCE.617.

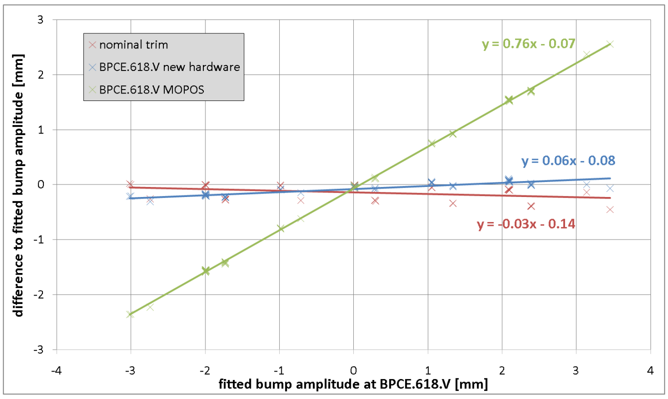

(b) Vertical position measurement of BPCE.618.

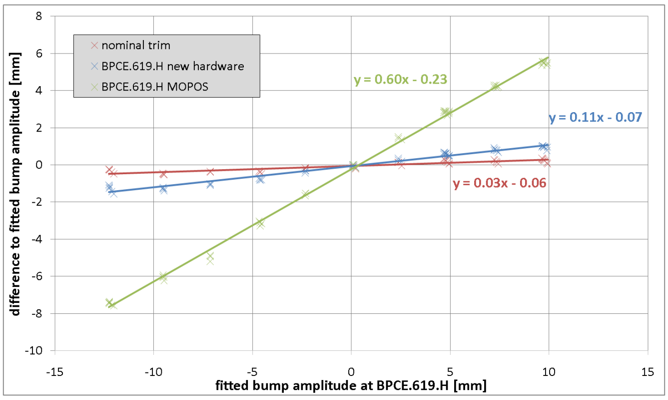

(c) Horizontal position measurement of BPCE.619.

Figure 5.3.: The difference to the fitted bump amplitude of the nominal trim, the position measured by the new hardware and the MOPOS hardware. 3π orbit bumps with different amplitudes are made. The measurements of the new hardware and the nominal trims are consistent with the fitted bump amplitudes. The single BPM MOPOS measurements are not in accordance with the other measurements.
Measurement conditions: cycle: CNGS1, beam energy: 14 GeV, bunch intensity: $3 - 6 \cdot 10^{10}$ protons, ≈ 400 bunches $\times$ 2.

at a frequency of 400 Hz (cf. Fig. 5.4a and [30]). Since the oscillations are extremely large and are not measured by the MOPOS hardware, it is assumed that they are an artifact of the electronics. The oscillations are observed by all BPMs and in all planes in LSS4 as well as in LSS6. They are only measured with sufficiently high bunch intensities ($\gtrsim 10^{10}$ protons) and only at the end of the cycle.
The observations lead to the assumption that the measured oscillations are due to a saturation of the acquisition hardware. In a dedicated test, the signal from one horizontal pickup was attenuated directly before the input to the acquisition card [30][4]. With a −10 db attenuation of the signal, the oscillations are significantly mitigated in both planes (cf. Fig 5.4b). With a −20 db attenuation no oscillation is measured anymore (cf. Fig 5.4c). Since only the signal from one pickup was attenuated during the test, the measured position also changes slightly.

The results support the hypothesis of a hardware saturation. Consequently, −16 db attenuators were installed for all pickups of all BPMs. Oscillations of the turn-by-turn position have not been measured ever since.
As expected, the attenuators worsen the performance for low intensity beams. In particular trigger problems that lead to outliers in the position measurement occur more often (cf. Appendix E.2) and the signal-to-noise ratio is worse (cf. Fig 5.4).

5.2.3. Tests for Final Commissioning

The revealed issues with the position acquisition system depict the necessity of certain tests and measurements for the final commissioning of the system. With regard to the purpose of the system, the following listing defines the minimal requirements of tests and measurements to ensure the correct performance of the system. An observation of other unexpected behaviour can make further tests necessary.

- **Intensity dependency:** The dependency of the position measurement on the bunch intensity must be known in the operational intensity range ($10^8 - 10^{11}$ protons). It must be well controlled for bunch intensities above 10^{10} protons (which corresponds to a stored beam energy of over 0.5 MJ for CNGS-type beam).
  For the horizontal plane, tests with different amplitudes of the extraction bumps are recommended. Additional tests with vertical orbit bumps are crucial, especially for the turn-by-turn position interlock.
  In 2009, tests with bunch intensities below $5 \cdot 10^9$ protons were done and revealed a large intensity dependency (cf. Appendix E.5).

[4] These test were done in close collaboration with T. Bogey from CERN BE-BI.

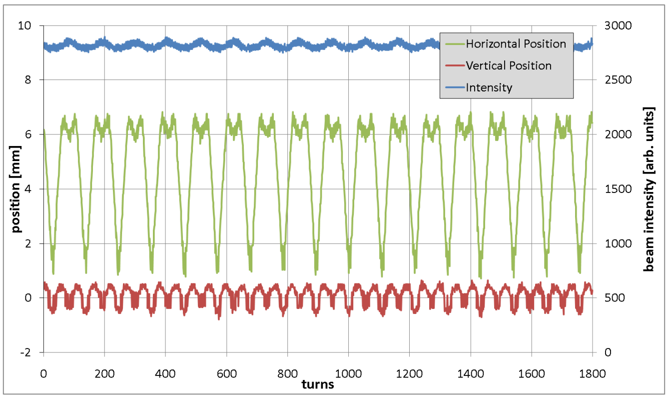

(a) No attenuation of signals. Large oscillations.

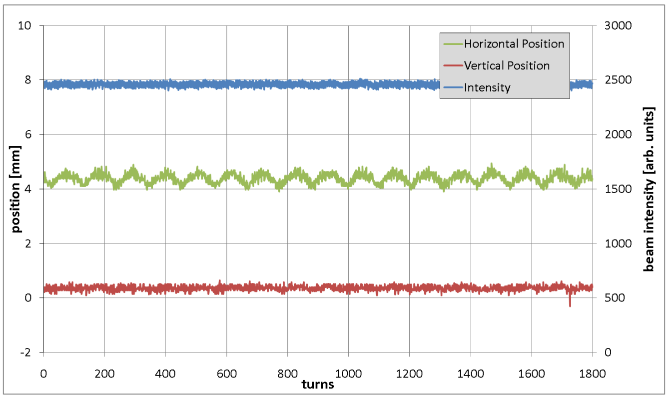

(b) One signal of BPCE.418.H is attenuated by −10 db. Reduced oscillations in both planes.

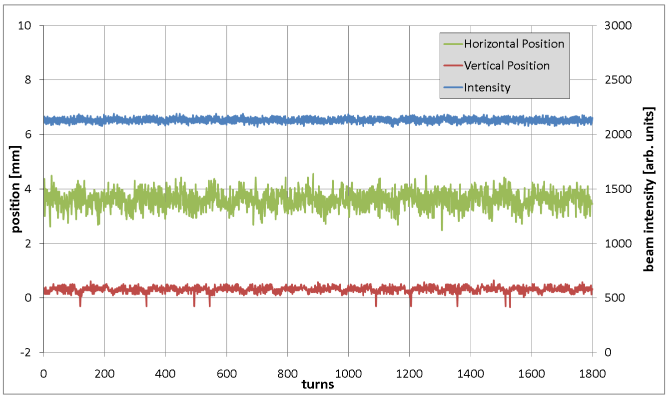

(c) One signal of BPCE.418.H is attenuated by −20 db. No oscillation.

Figure 5.4.: Measured beam position at BPCE.418 by the new position acquisition system. The oscillations have a frequency of ≈ 400 Hz and are not measured by MOPOS hardware. The plotted intensity refers to the logarithmic quantification of the beam intensity as it is measured by the new position acquisiton system (based on logarithmic amplifiers). Measurement conditions: cycle: LHCFAST2, beam energy: 450 GeV, bunch intensity: $\approx 1 \cdot 10^{11}$ protons, single bunch.

- **Position measurement verification LSS4:** The systematic error of the position measurement needs to be determined for all BPMs. The tests done with the BPMs in LSS6 (cf. section 5.2.1 and Appendix F) need to be done for the BPMs in LSS4 also. It is recommended to verify the position by using horizontal and vertical 3π orbit bumps. A good orbit correction prior to the test is crucial.
  The systematic error should not exceed $\approx 10\,\%$. The results can be used for a beam based calibration of the system[5].
- **Long term stability:** The long term stability of the system is particularly important to ensure a good performance of the extraction interlock system. During a 24 hour test with CNGS-type beam in May 2010, the average position measurement drifted by up to $300\,\mu$m at BPCE.618.H. Similar tests for LHC-type beam are recommended, as soon as there are no more modifications to the acquisition hardware. It needs to be assured that the orbit corrector and acquisition hardware settings are constant during the test.

5.3. Turn-by-turn Position Interlock Algorithm

The turn-by-turn position interlock is designed to replace the existing analog 30 mm interlock. It sends a beam dump signal if a single measured position at one of the BPMs in LSS6 exceeds a fixed tolerance window (e.g. ± 30 mm). The control room software *Moin moin* (cf. Appendix D) provides an interface for interlock algorithms which allows to verify the performance of the algorithms offline, using saved turn-by-turn position datasets. During the experiments on tune resonance phenomena in 2009, many datasets of different integer tune resonance crossings were acquired.
An analysis of the simple design interlock algorithm revealed that with nominal thresholds at ± 30 mm the turn-by-turn interlock system would only detect 193 out of 427 tune resonance crossings early enough to dump the beam before significant beam losses occur. Even with reduced thresholds at ± 10 mm, not all failures are detected in time. Such tight thresholds do not only limit the operational flexibility to an unacceptable level, but also cause problems with injection oscillations that can have peak-to-peak amplitudes of more than 20 mm during transients of setup periods [31].

[5] The new position acquisition hardware is calibrated via an internal calibration unit. A beam based calibration of the system also takes into account the pickups and the cables.

Novel Interlock Algorithm

With the aim to keep the interlock algorithm as simple as possible but as differentiated as necessary, alternative interlock algorithms were developed and optimized. The best performing algorithm is characterized by three basic features:

1. In order to be sensitive to fast position changes, the tolerance window is dynamically centered around the average position which allows for a much tighter width $2 \cdot T$ of the tolerance window. The average position is calculated as a running mean with the parameter n_{orbit} defining the number of turns that are taken into account.

2. For LHC-type beam, up to four injections during the cycle are foreseen [4]. The injections are accompanied by oscillations with peak-to-peak amplitudes of up to several mm [31]. The frequency of the oscillations is defined by the tune. In order to ensure that the turn-by-turn interlock does not trigger on injection oscillations, a (time dependent[6]) low-pass filter is implemented. A simple averaging filter is used, i.e. the interlock algorithm is not applied on the last turn only, but on the average position of the last few turns[7]. The parameter n_{pos} defines the number of turns that are taken into account.
   This does not influence the detection of integer tune resonances, since the frequency of the position oscillations close to an integer tune value is below the cutoff frequency of the low-pass filter.

3. The turn-by-turn measurement has sometimes outliers. Hence, a simple outlier detection is implemented. A position measurement $pos(t)$ for turn t is neglected if

$$\begin{aligned} pos(t) &> \max\left[pos(t-1), pos(t+1)\right] + T_{outlier} \quad \text{or} \\ pos(t) &< \min\left[pos(t-1), pos(t+1)\right] - T_{outlier}. \end{aligned} \tag{5.1}$$

   with $T_{outlier}$ being a fixed threshold for the outlier detection.

The novel interlock algorithm triggers an interlock at turn t_0 if the following condition is fulfilled:

$$\left| \frac{1}{n_{pos}} \left(\sum_{t=t_0-1}^{t_0-1-n_{pos}} pos(t) \right) - \frac{1}{n_{orbit}} \left(\sum_{t=t_0-1-n_{pos}}^{t_0-1-n_{pos}-n_{orbit}} pos(t) \right) \right| > T. \tag{5.2}$$

If $pos(t)$ is detected to be an outlier, the corresponding sum neglects the outlier, but takes into account an additional previous turn instead.

[6] The low-pass filter is only needed during the injection and can be disabled after the last injection.

[7] For nominal LHC-type beam, the oscillations have a period of $\frac{1}{0.13} = 7.7$ turns in the horizontal plane and $\frac{1}{0.18} = 5.6$ turns in the vertical plane. For CNGS-type beam the oscillation periods are $\frac{1}{1-0.58} = 2.4$ turns and $\frac{1}{1-0.61} = 2.6$ turns, respectively.

With the optimized parameters given in Table 5.2 this interlock algorithm yields excellent results in the offline analysis: All 427 integer tune resonance crossings are detected, typically at least 30 turns before beam losses are observable. For 898 randomly selected datasets, taken during normal operation, no interlock is triggered. Figure 5.5 shows the performance of the new interlock algorithm and the simple threshold algorithm (with tight thresholds at ±10 mm) for the case which is also presented in Fig. 3.1. The new interlock algorithms detects the failure 38 turns before the first beam losses are measurable.

Parameter	**Value**
n_{orbit}	150 turns
n_{pos}	7 turns
T	3 mm
$T_{outlier}$	0.2 mm

Table 5.2.: Optimized parameters for the novel turn-by-turn interlock algorithm (LHC-type beam).

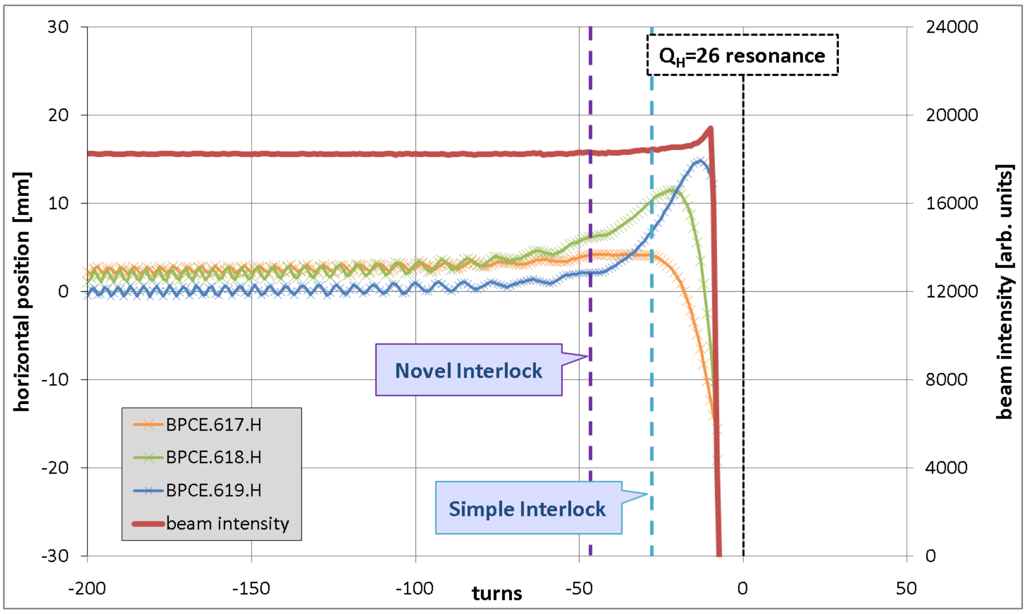

Figure 5.5.: Tune shift towards the $Q_H = 26$ integer tune resonance (cf. Fig. 3.1). The vertical lines indicate the turns at which the novel interlock algorithm (design parameter given in Table 5.2) and the simple design interlock algorithm (threshold at ±10 mm) would trigger an interlock. Measurement conditions: cycle: LHCFAST2, beam energy: 450 GeV, bunch intensity: $1.0 \cdot 10^{10}$ protons, 12 bunches.

5.4. Commissioning of the Extraction Interlock

Systematic commissioning tests have been done to prove the correct performance of the complete logic of the new extraction interlock. The tests verified the correct behaviour of the output signal of the new system, with the system fully connected to the Extraction Interlock System. The input to the Beam Interlock Controller was disabled to allow for comprehensive tests without provoking unnecessary beam dumps.
Especially the correct timing of the interlock system is important. For CNGS-type beam, the second batch is extracted 50 ms after the extraction of the first batch. The timing events and the data processing had to be optimized to allow for an independent interlock processing for each extraction[8].
Figure 5.6 shows the logical signal of the new extraction interlock for a case where the interlock tests are passed for both extractions.

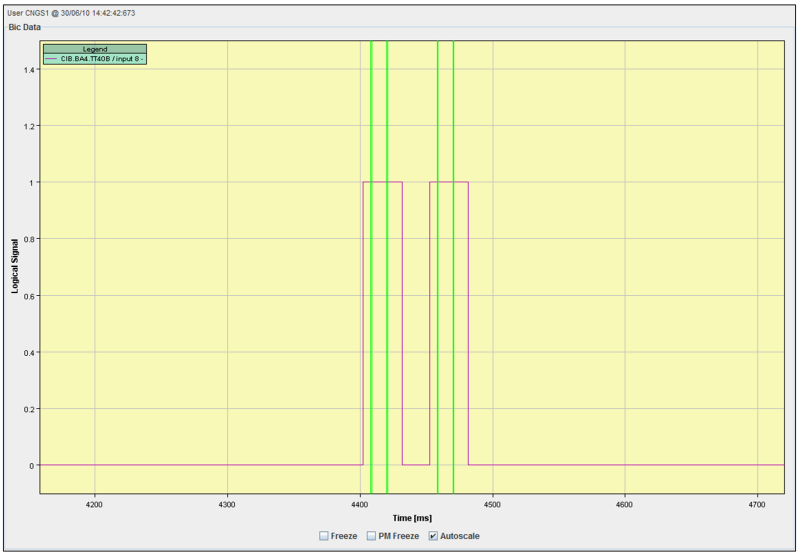

Figure 5.6.: Logical signal of the new extraction interlock (red). The signal needs to be 1 at the green lines to allow the beam extraction. The two peaks correspond to the first and second extraction, respectively.
Measurement conditions: cycle: CNGS1, beam energy: 400 GeV, bunch intensity: $5 \cdot 10^{10}$ protons, ≈ 400 bunches $\times$ 2.

The extraction interlock is very dependent on a stable performance of the position acquisition system. Especially, a batch dependency of the position measurement (cf. Appendix E.3) enforces unacceptably large tolerance windows. A solution to this issue is crucial to reach the desired performance.

[8] For example, the average beam position was changed to be calculated by the IIR filter in the hardware to improve the runtime performance.

5.5. Outlook

The commissioning revealed many issues, in particular related to the position acquisition. Further commissioning tests are essential to understand the underlying effects and improve the performance of the acquisition system to an acceptable level (cf. Appendix E and section 5.2.3).
Nevertheless, the extraction interlock has a reasonable performance for nominal CNGS-type beam (apart from the batch dependency explained in Appendix E.3). It is recommended to put it into full operation for this beam type as soon as possible. In the early stage, the tolerance windows must be set wide enough not to constrain the routine operation.
The turn-by-turn position interlock and the post mortem acquisition feature will be implemented in the FESA class, soon. It is recommended to change the turn-by-turn interlock algorithm in the hardware also as soon as possible. First in situ tests with the turn-by-turn interlock are expected in the third quarter of 2010.

Out of the three pickups used for the turn-by-turn position interlock, the pickups BPCE.617 and BPCE.619 are positioned close to a defocusing quadrupole and BPCE.618 is located close to a focusing quadrupole. Thus, there is an increased accuracy to detect vertical orbit oscillations[9].
The horizontal position at the three BPMs may have large offsets due to the extraction bump. A significant negative effect of the extraction bump on the performance of the turn-by-turn position interlock system is expected.
Hence, it is recommended to reposition the hardware for the turn-by-turn interlock system and to use standard pickups in the arcs instead. Two pickups per plane with $\approx 90^\circ$ betatron phase difference are a minimal requirement for a full phase space coverage. Taking into account the performance of the acquisition system, the use of additional (redundant) pickups can be necessary to provide an adequate machine protection.
Pickups of the same type that are not influenced by the extraction bumps should be used. The beta function should be maximal at the pickups. The hardware sensitivity to radiation exposure needs to be taken into account, thus, a positioning upstream of the extraction can be advantageous. Considering these requirements, the following set of BPMs is suitable: (BPH.606), BPH.608, BPH.610, (BPV.605), BPV.607, BPV.609.

[9] With the values of the beta functions given in Table 2.1, the amplitude of horizontal position oscillations at defocusing quadrupoles is reduced by a factor $\sqrt{\beta_{x,QD}}/\sqrt{\beta_{x,QF}} = 0.45$ with respect to the amplitude at focusing quadrupoles. Similarly, vertical position oscillations are suppressed by the same factor at focusing quadrupoles.

6. Discussion and Comments on SPS Machine Protection

The machine protection against beam based incidents is done on three levels:

1. **Detection of failure source:** The source of the failure, e.g. a hardware equipment failure is detected and interlocked directly. An example is the SPS power converter interlock (cf. section 2.3.2) or a FMCM interlock (cf. section 2.4). By detecting the failure at the source, the beam can principally be dumped before it is affected by the failure. On the other hand, such a machine protection system is always limited to a very specific failure scenario and does not provide protection against unexpected failure modes.
2. **Beam based interlock:** The failure has an effect on the beam. The abnormal beam behaviour is detected and interlocked. The position interlock works on this level. The erroneous behaviour can be detected early enough to prevent beam losses. Furthermore the detection is not limited to one specific hardware failure scenario, but protection is provided against all failures that lead to the same abnormal beam dynamics, e.g. the position interlock can also protect against certain operational errors.
3. **Interlock on beam losses:** As soon as the failure leads to beam losses, BLMs dump the beam. They provide an unspecific protection against a wide range of failure scenarios that lead to slow beam losses (slower than the reaction time of the BLMs). No protection is provided against fast failures (faster than the reaction time of the BLMs). A protection against failures that lead to significant beam losses in less than one turn is not possible, since the complete beam dump takes at least one turn.

In the SPS, the BLMs and the interlock on the power converters are too slow to provide a protection against fast failures (cf. section 4.1 and section 4.2). Only the turn-by-turn position interlock has an adequate reaction time. It will protect the SPS against all failure scenarios that lead to orbit oscillations. No protection against other fast failure scenarios is provided.
Nevertheless, to ensure an adequate machine protection, a redundancy in the ma-

chine protection systems is needed, especially for high intensity high energy accelerators. For the SPS, this is not the case at present. The reaction times of the protection systems on the 1^{st} and 2^{nd} level should also be improved. Two upgrade scenarios are addressed in the following sections.

6.1. FMCMs for the SPS

The FMCMs in the LHC and at HERA have an outstanding performance (cf. section 4.3). FMCMs for the main SPS circuits would significantly improve the SPS machine protection against fast failures. Since a decay of the quadrupole magnets is the most critical failure scenario (cf. section 4.2), the design performance of FMCMs must be defined by the decay time of the quadrupole magnets. Considering the failure tests (cf. section 4.2 and Appendix C) and allowing a maximal tune change of 0.05 , the FMCMs must have a relative tolerance of less than $3 \cdot 10^{-2}\,\%$ with a reaction time of less than 0.3 ms[1]. The design tolerance of the LHC FMCMs is also $3 \cdot 10^{-2}\,\%$ with a reaction time of 0.7 ms [15, p. 2].

6.2. New SPS BLM System

In order to improve the reaction time of ≈ 20 ms (= 870 turns) an upgrade of the SPS ring BLM system is foreseen. In the view of the good performance of the LHC BLM system [32], the design of the LHC BLM system will be used and modified as required. The LHC BLM system integrates beam losses over 9 different time intervals between 40 μs and 1.3 s.
For the SPS, a reaction time of less than one turn (= 23 μs) is reasonable. In order to be sensitive to slow beam losses also, different integration times are also needed.

The BLM upgrade will significantly improve the SPS machine protection. Nevertheless, it must always be complemented by machine protection systems against very fast failures that lead to significant beam losses in less than one turn.

[1] For the failure of the main focusing quadrupole circuits at CNGS injection energy (cf. Table 4.1 and Table 4.2), the upper limit of the tune change ΔQ is estimated by $\Delta Q \leq \frac{3.2 \cdot 10^{-3}}{0.023} t_r + 26.61 \cdot T_C$, with T_C being the relative tolerance and t_r being the reaction time in ms.

7. Conclusion

The main goal of this work is to understand the beam dynamics and beam loss pattern at different SPS tune resonances. The results are used to advance the new position interlock and to ensure that it provides an adequate machine protection, against the background of the 2008 incident.

The first three months of the thesis work were dedicated to simulations, tracking studies and experiments to identify and analyze the relevant tune resonance phenomena. In the fourth quarter of 2009, the SPS machine protection systems were reviewed and many tests with the new position acquisition system were made. The technical stop of the accelerators in the beginning of 2010 was used to analyze the experimental studies in detail and to develop and optimize the control room software and the turn-by-turn interlock algorithm. The second quarter of 2010 was dominated by the commissioning of the position acquisition system and the extraction interlock system and the preparation of this document.
This organization ensured a good balance between experiments, simulations, design of the new interlock system and its commissioning. The topics defined in the thesis description are fully covered [33].

The tune resonance studies reveal and explain unexpected behaviour, e.g. the strength of the superperiodic dispersion resonance (cf. section 3.1.2) or the complete beam loss in as little as 3 turns at the $Q_H = 26$ tune resonance (cf. Fig. 3.1). The analysis of the beam losses provides a well understanding of the beam loss patterns (cf. section 3.3 and section 3.4). The data is consistent with expectations and data from the 2008 incident.
These results are crucial information for the development (e.g. of the turn-by-turn position interlock algorithm) and commissioning of the new interlock system. The necessity of the new system is proved by the review of the related SPS machine protection systems, which shows that the present systems are much too slow to protect the machine against fast failures (cf. chapter 4).
The commissioning of the new interlock systems revealed many unexpected issues. Especially the problems with the position acquisition hardware are critical for the performance of the new interlock systems and retard the commissioning phase.
In the retrospective, earlier dedicated in situ tests of the new interlock systems could

have improved the efficiency of the commissioning.

The results provide clear understanding of the specified failure scenarios and their effects, the performance of the related SPS machine protection systems and the performance of the new interlock systems. This work is a major step on the way towards an adequate machine protection against fast equipment failures.

The results of the work were presented and published in the course of the *Joint DESY and University of Hamburg Accelerator Physics Seminar* (February 2010, Hamburg) [25], at the *74. Annual Conference of the DPG* (March 2010, Bonn) [31] and at the *International Particle Accelerator Conference* (May 2010, Kyoto) [34]. A further publication at the *Advanced Beam Dynamics Workshop on High-Intensity and High-Brightness Hadron Beams* (September 2010, Moorschach) is foreseen.

Bibliography

[1] "Convention for the Establishment of a European Organization for Nuclear Research," Paris, July 1953.

[2] N. Agafonova *et al.*, "Observation of a First ν_τ Candidate in the OPERA Experiment in the CNGS Beam," *arXiv 1006.1623*, June 2010.

[3] F. Hinterberger, *Physik der Teilchenbeschleuniger und Ionenoptik.* Springer-Verlag, 2 ed., 2008.

[4] M. Benedikt, P. Collier, V. Mertens, J. Poole, and K. Schindl, *LHC Design Report - The LHC Injector Chain*, vol. 3. CERN, 2004.

[5] J. Wenninger, "SPS Machine Protection Incident in 2008," *CERN-BE-2009-003-OP*, January 2009.

[6] H. Wiedemann, *Particle Accelerator Physics.* Springer-Verlag, 1 ed., 1993.

[7] K. Wille, *The Physics of Particle Accelerators.* Oxford University Press, 1 ed., 2000.

[8] G. W. Hill, "On the part of the motion of the lunar perigee which is a function of the mean motions of the sun and moon," *Acta Mathematica*, vol. 8, pp. 1–36, December 1886.

[9] D. W. Kerst, "The Acceleration of Electrons by Magnetic Induction," *Phys. Rev.*, vol. 60, pp. 47–53, July 1941.

[10] V. Kain, *Machine Protection and Beam Quality during the LHC Injection Process.* PhD thesis, Tech. Univ. Wien/CERN, October 2005.

[11] R. Giachino, B. Puccio, R. Schmidt, and J. Wenninger, "Architecture of the SPS Beam and Extraction Interlock Systems," *CERN-AB-2003-010-OP*, April 2003.

[12] A. H. Dinius, J. C. L. Brazier, and P. Semanaz, "Evolution of the SPS Power Converter Controls towards the LHC Era," *CERN-SL-2001-066-PO*, December 2001.

[13] J. de Vries, C. Boccard, and T. Bogey, "MOPOS Acquisition System Design Study," *CERN-SL-97-00-BI*, 1997.

[14] J. Wenninger, "Software Interlocks & Timing System." Manual, CERN, Mai 2008.

[15] M. Werner, M. Zerlauth, R. Schmidt, V. Kain, and B. Goddard, "A Fast Magnet Current Change Monitor for Machine Protection in HERA and the LHC," in *Proceedings of Int. Conf. on Accelerator & Large Expt. Physics Control Systems*, October 2005.

[16] M. Werner, "Einrichtung zur Bestimmung der Stärke des Magnetfeldes eines Elektromagneten." Patent DE102005045537B3 28.12.2006, September 2005.

[17] M. Zerlauth, "Machine Protection Systems for CNGS." Presentation, CERN, June 2006.

[18] A. Gomez Alonso and R. Schmidt, *Redundancy of the LHC Machine Protection Systems in case of Magnet Failures.* PhD thesis, Universitat Politècnica de Catalunya/CERN, April 2009.

[19] M. G. Minty and F. Zimmermann, *Measurement and Control of Charged Particle Beams.* Springer-Verlag, 1 ed., 2003.

[20] J. Wenninger and K. Fischer, "HW Interlock Test Sheet (SPS Main Power Converters)." CERN, May 2007.

[21] J. Wenninger and K. Fischer, "HW Interlock Test Sheet (SPS Main Power Converters)." CERN, May 2008.

[22] M. Zerlauth and R. Schmidt, *Powering and Machine Protection of the Superconducting LHC Accelerator.* PhD thesis, Tech. Univ. Graz/CERN, June 2004.

[23] V. Kain, "Power Converter Failure of the Normal Conducting D1 Magnet at Experiment Insertions IR1 and IR5," *CERN-LHC-Project-note-322*, September 2003.

[24] A. Gomez Alonso, "Most Probable Failures in LHC Magnets and Time Constants of their Effects on the Beam," *CERN-LHC-Project-note-389*, November 2006.

[25] T. Baer, "Operational Experience with the LHC and SPS Tune Resonance Phenomena." Presentation at DESY Accelerator Physics Seminar, Hamburg, February 2010.

[26] R. Schmidt and J. Wenninger, "Analysis of a Few Beam Dumps – Functionality of Protection Systems." Presentation at LHC Machine Protection Panel, CERN,

December 2009.

[27] J. Wenninger, "Software Interlock System." Presentation at MPS Internal Review, CERN, June 2010.

[28] T. Bogey and R. Jones, "Interlock Beam Position Monitors for the SPS," *CERN BE/BI*, December 2008.

[29] J.-J. Savioz, "Digital Acquisition Firmware for the SPS Beam Position Monitors," *CERN BE/BI*, May 2009.

[30] T. Baer and T. Bogey, "SPS BPCE LSS4 Test Sheet," *CERN BE*, March 2010.

[31] T. Baer, "Tune Resonance Phenomena in the SPS and Related Machine Protection." Presentation at 74. Jahrestagung der DPG, Bonn, March 2010.

[32] O. S. Brüning, P. Collier, P. Lebrun, S. Myers, R. Ostojic, J. Poole, and P. Proudlock, *LHC Design Report - The LHC Main Ring*, vol. 1. CERN, 2004.

[33] J. Wenninger, "Thesis Description T. Baer." Technical Student Thesis Description, CERN, April 2009.

[34] T. Baer *et al.*, "Tune Resonance Phenomena in the SPS and Machine Protection via Fast Position Interlocking," in *Proceedings of IPAC'10, Kyoto*, pp. 1602–1604, May 2010.

Appendix

A. Static MAD-X Simulations

Distinct simulations to understand the beam dynamics at SPS tune resonances have been done. The simulations are done by a script package called *DispersionSim* based on MAD-X[1]. The optics for LHC-type beam are used. The relevant parameters like closed orbit, dispersion or beta function are calculated using the *twiss* command. The *match* command is used on the quadrupole strengths to adjust the tunes. As is discussed in section 2.2, small field errors play an important role for tune resonance phenomena. The main cause of these small field errors are misaligned magnets [3, p. 292]. The simulation accounts for field errors by three different kinds of misalignments.

1. **Statistical Error:** A statistical horizontal and vertical misalignment is added to all elements of the accelerator. The misalignments follow a gaussian distribution with a cutoff at 3σ. The statistical misalignments account for fluctuations (within the error margin) in the positioning of the elements.

2. **Systematic Sextant Quadrupole Misalignment:** For the first quadrupoles of every sextant the same misalignment is added. For focusing quadrupoles a misalignment is added only in the horizontal plane, for defocusing quadrupoles only in the vertical plane. The systematic sextant quadrupole misalignment is crucial for superperiodic resonances (cf. section 3.2). It represents all dipolar field error components that are similar in every sextant, e.g. systematic errors in the long straight sections.

3. **Systematic Quadrupole Misalignment:** For all quadrupoles, the same systematic misalignment is added. For focusing quadrupoles a misalignment is added only in the horizontal plane, for defocusing quadrupoles only in the vertical plane. The systematic quadrupole misalignment accounts for systematic dipolar field errors, e.g. additional dipolar field components in the magnets, which are likely to have a systematic character. These errors are among other crucial for higher order superperiodic behaviour, i.e. superperiodic behaviour

[1] MAD-X is a free program for the simulation of particle accelerators and their design. MAD-X is developed and maintained by CERN BE-ABP and was released for the first time in 2002. http://mad.web.cern.ch/mad.

which is due to higher order symmetries that have their origin in the periodic FODO cell structure.

Since the exact amount of all these misalignments cannot be known, they are treated as free parameters of the model. The misalignments are chosen in a way that the results, i.e. rms closed orbit and vertical dispersion, are in best agreement with the measurements (cf. section 3.1.1 and section 3.1.2). The dispersion has its origin in dipolar fields which are in the horizontal plane dominated by the main dipole magnets (cf. section 2.2). Thus, the horizontal dispersion is in first order approximation independent of field errors. This leads to especially reliable simulations of the horizontal dispersion.

B. MAD-X Tracking Studies

A script controlled simulation environment for MAD-X tracking studies is used for analysis of the beam loss pattern of different tune resonances. Main purpose is the tracking of an ensemble of simulated particles for about 1000 turns in the SPS with time dependent currents (mainly a fast decay of the quadrupole currents) and recording the loss times and places of particles exceeding the aperture[1].
In general, LHC-type beam optics are used and the particle distribution is calculated from the nominal LHC beam parameters[2]. The **thin tracking** algorithm is utilized which offers via the (undocumented) *update* option an easy possibility to apply discrete changes to the quadrupole strengths after each revolution. The algorithm requires a thin representation (i.e. elements with zero length) of the accelerator which makes it necessary to convert all elements of the SPS to thin elements using the *makethin* command. Comparison studies (also with *ptc-track*) showed that a deseperation of each thick element into 5 thin elements yields good results at reasonable processing times. The simulation takes into account a random misalignment of the elements.

[1]The turn and position at which a particle exceeds the aperture for the first time is saved and the particle is removed from the particle ensemble.
[2]Normalized emittance: $\epsilon_{H/V}^{n,1\sigma} = 3.5\mu m \cdot rad$.

C. Power Converter Interlock Test

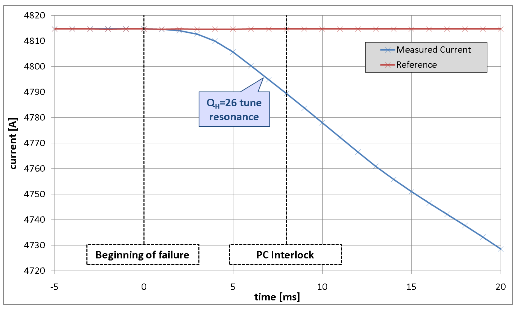

(a) Main bend circuit at 400 GeV/c.

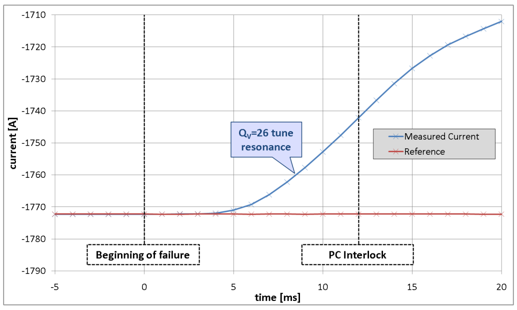

(b) Defocusing quadrupole circuit at 400 GeV/c.

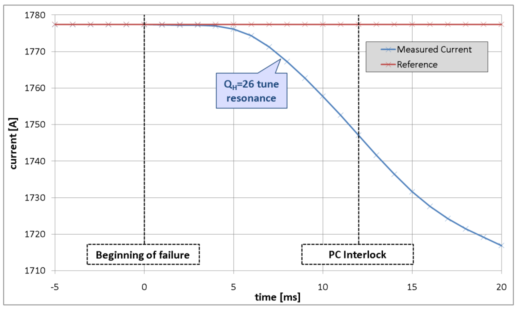

(c) Focusing quadrupole circuit QF1 at 400 GeV/c.

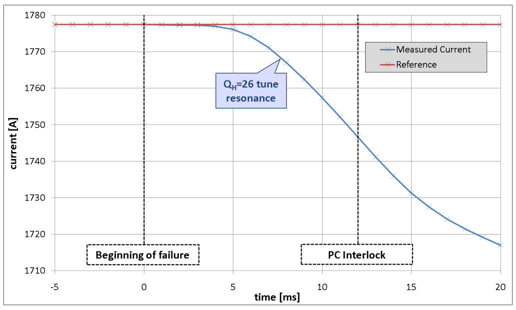

(d) Focusing quadrupole circuit QF2 at 400 GeV/c.

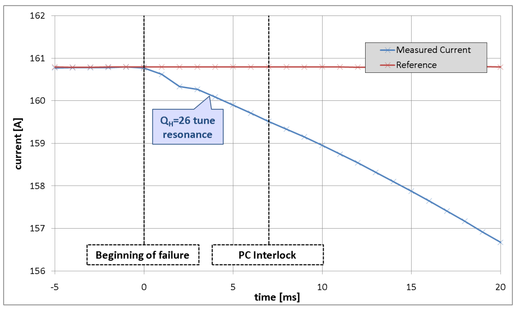

(e) Main bend circuit at 14 GeV/c.

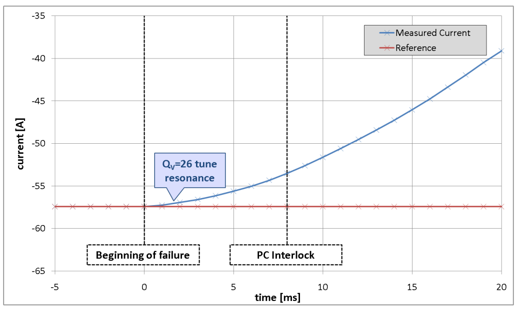

(f) Defocusing quadrupole circuit at 14 GeV/c.

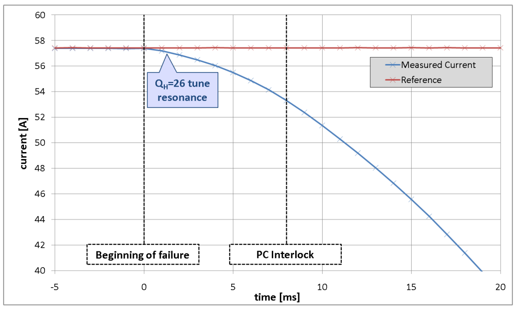

(g) Focusing quadrupole circuit QF1 at 14 GeV/c.

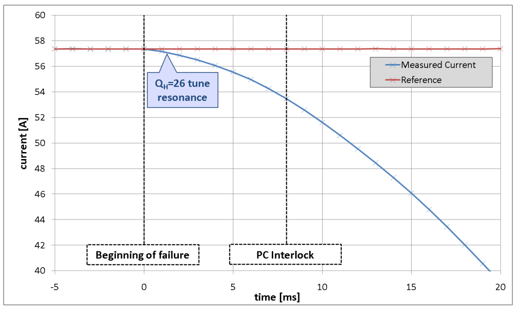

(h) Focusing quadrupole circuit QF2 at 14 GeV/c.

Figure C.1.: Test of the power converter interlock of the main magnet circuits in the SPS. The power supply of the power converters is abruptly interrupted.

D. The Control Room Software Moin Moin

The java application *Moin Moin*[1] provides an user interface to the new SPS position interlock system for the use in the *Cern Control Centre* (cf. section 5.1). The software is the standard tool to display and analyze the measured data from the six interlock BPMs and to control the settings for the extraction interlock. A dedicated analysis module is implemented for data and interlock analysis.
The functionality of the software is explained in the following sections. The sections correspond to the software menu items.

D.1. Acquisition

The control room software acquires data directly from the BPMINT FESA class via the *japc* API. Two independent acquisition modules are implemented to acquire closed orbit data (cf. Fig. D.1) and turn-by-turn position data (cf. Fig. D.2). Once an acquisition is started, it is continued in the background until it is stopped.

D.2. Interlock

The extraction interlock is processed by the BPMINT FESA class. Moin Moin provides an user interface to control the basic settings of the extraction interlock (cf. Fig. D.3). Different tolerance windows can be defined for LHC-type beam and CNGS-type beam. The extraction is inhibited if the measured position exceeds the window defined by position $\pm$ tolerance for one active[2] BPM. One of the two different

[1] The application is found in the SPS control room consoles menu under *SPS Control/SPS Beam Interlocks/SPS BPM Interlock Monitor*. From the CERN intranet it is started by executing http://abwww.cern.ch/ap/dist/sps/sps-bpmint/PRO/SPS_BPMINT.jnlp.
[2] Horizontal and vertical channel of each BPM are combined and are activated or deactivated together.

Figure D.1.: Screenshot of the Moin Moin position acquisition module.
1: Selection of SPS cycle. 2: Start of acquisition. 3: Stop of acquisition. 4: Save data as (zipped) sdds file. 5: Switch between display for LSS4 and LSS6. 6, 7: Position display. 8, 9: Tables with values of last acquisition.

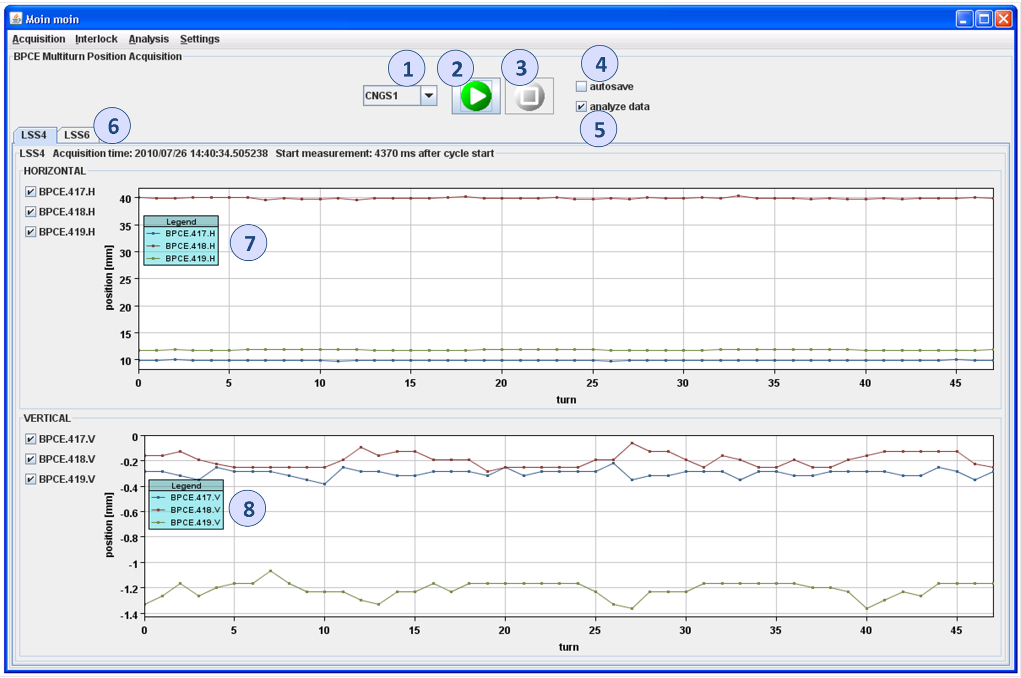

Figure D.2.: Screenshot of the Moin Moin turn-by-turn position acquisition module. 1: Selection of SPS cycle. 2: Start of acquisition. 3: Stop of acquisition. 4: Check to automatically save new datasets (cf. section D.4). 5: Check to automatically add new datasets to the analysis module (cf. section D.3). 6: Switch between display for LSS4 and LSS6. 7, 8: Position display.

interlock settings (LHC or CNGS) is allocated to each cycle. The mapping is defined directly in the FESA class and can be configured via the FESA Navigation Tool[3].

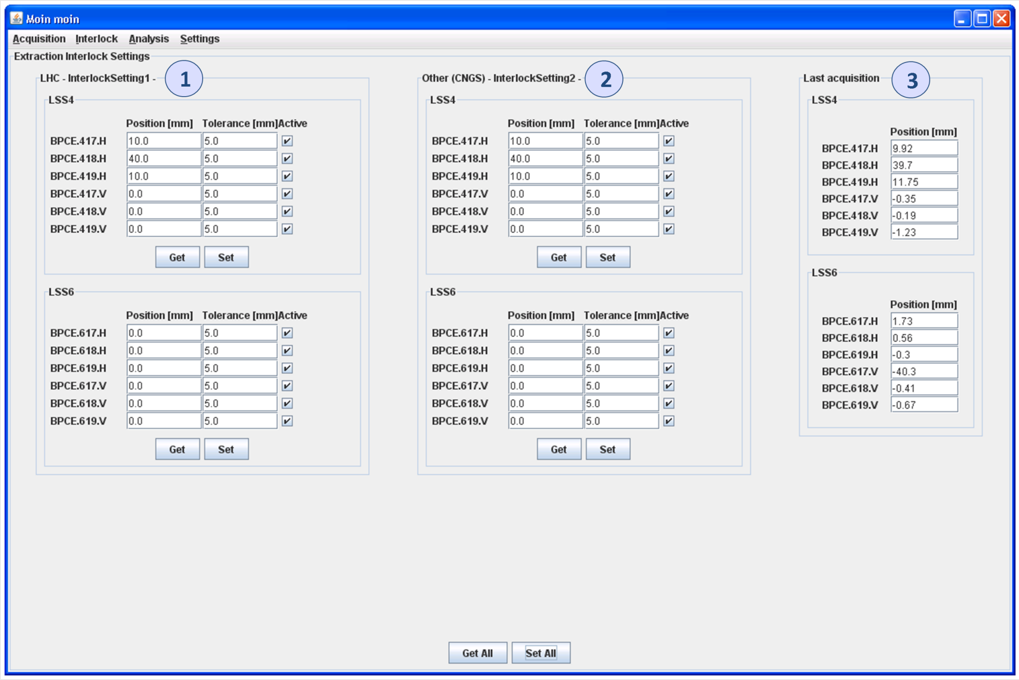

Figure D.3.: Screenshot of the Moin Moin extraction interlock configuration screen. 1: Settings for LHC-type beam. 2: Settings for CNGS-type beam. 3: Tables with values of last position acquisition.

D.3. Analysis

The analysis module is used for post analysis of turn-by-turn position data (cf. Fig. D.4). It can handle Moin Moin-type sdds files as well as SPS Multiturn files. Different turn-by-turn interlock and analysis algorithms are implemented to test and optimize their performance. Well defined interfaces ensure an easy implementation of additional interlock algorithms. After an analysis, a comprehensive summary is displayed.
The implemented algorithms are explained in the following sections.

Standard Interlock Model

The interlock algorithm described in section 5.3 is used. The following parameters can be configured:

[3]http://wwwpsco.cern.ch/private/java/fesa/2.10/FNT.jnlp.

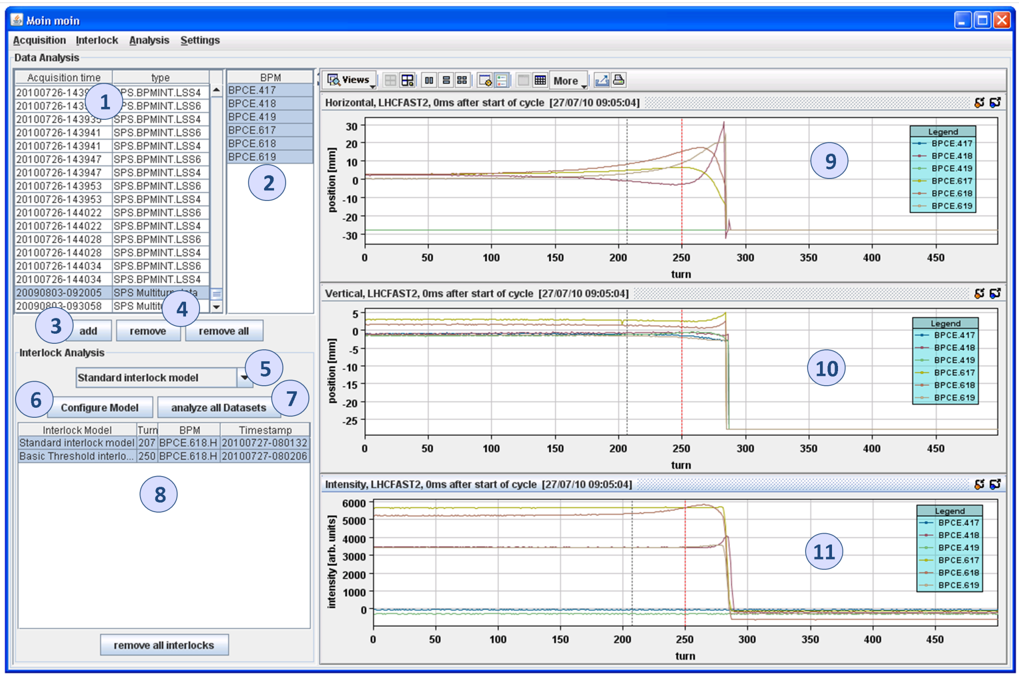

Figure D.4.: Screenshot of the Moin Moin analysis module.
1: List of datasets. 2: Available BPM data for selected dataset. 3: Load dataset from sdds file (Moin Moin data or SPS Multiturn data). 4: Remove selected or all datasets from analysis module. 5: Select turn-by-turn interlock algorithm for analysis. 6: Configure selected algorithm. 7: Start turn-by-turn interlock analysis. 8: List of turn-by-turn interlock analyses. 9, 10, 11: Horizontal position, vertical position and BPM intensity. Vertical lines indicate the turn of the first turn-by-turn interlock trigger for the interlock analyses selected in 8.

- **Interval for closed orbit mean [turns]:** The parameter n_{orbit} as described in section 5.3.
- **Interval for mean of current position [turns]:** The parameter n_{pos} as described in section 5.3.
- **Maximal allowed difference [mm]:** The threshold T as described in section 5.3.
- **Threshold for outliers [mm]:** The threshold $T_{outlier}$ for the outlier detection as described in section 5.3.

LHC-like Interlock Model

A modified version of the turn-by-turn interlock algorithm of the LHC is used. The tolerance window is centered around the closed orbit. If the measured position is outside of the tolerance window more than n_{exceed} times in the last n_{turns} turns at a single BPM, an interlock is triggered. The following parameters can be configured:

- **Minimum valid values for mean calculations [1]:** The minimum number of valid positions to calculate the closed orbit position. If not enough valid data is available (e.g. in the beginning of the cycle), the interlock is not triggered.
- **Maximal number of allowed threshold exceedings [1]:** The parameter n_{exceed}.
- **Turn interval width for threshold exceedings [turns]:** The parameter n_{turns}.
- **Position threshold [mm]:** The half width of the tolerance window.

Basic Threshold Interlock Model

The simple interlock model implemented in the hardware. An interlock is triggered if the measured position at a single BPM exceeds the threshold. Only one parameter is needed:

- **Position Threshold [mm]:** The half width of the tolerance window (centered around zero).

Outlier Detection

An algorithm to search for outliers in the turn-by-turn position data. The outlier detection is explained in section 5.3. The following parameter can be configured:

- **Threshold for outliers [mm]:** The parameter $T_{outlier}$ as described in section 5.3.

D.4. Settings

The settings menu item allows to change the autosave path of the turn-by-turn position acquisition.
Two settings for the closed orbit position acquisition can be configured:

- **Position calculation method:** Changes the calculation method of the closed orbit position. It can be either calculated directly in the hardware by the IIR filter or by averaging the turn-by-turn position data in the BPMINT FESA class (cf. section 5.1.1).
- **First or second acquisition:** In order to allow for independent processing of the extraction interlock for the two CNGS extractions of first and second batch, the closed orbit position is determined before both extractions. The acquisition that is used by Moin Moin is selected via this option.

E. Issues with the New Position Acquisition System

E.1. 8kHz Oscillation

On top of the 400 Hz oscillations (cf. section 5.2.2) a 8 kHz sawtooth oscillation is measured by all BPMs in all planes (cf. Fig. E.1). The peak-to-peak amplitude is up to 2 mm. Like the 400 Hz oscillations, the 8 kHz oscillations have not been observed after the installation of the signal attenuators (cf. section 5.2.2).

E.2. Outliers

The turn-by-turn position measurement has in certain cases many outliers that can even affect significantly the average position measurement (cf. Fig. E.2). In particular for low bunch intensities ($\lesssim 10^{10}$ protons), many outliers are observed. The attenuators, installed to increase the intensity limit for the hardware saturation, worsen the problem. It is assumed that an incorrect triggering behaviour (e.g. on satellite bunches) of the internal trigger accounts for many of the outliers.

E.3. Batch and Integrator Length Dependent Position Measurement

For CNGS beam, two batches of about 400 bunches each are injected and extracted separately. The measured positions change by about 5 mm after the extraction of the first CNGS batch (cf. Fig. E.3). This behaviour is not measured by the MOPOS hardware and is not expected to be beam related, since the optics and orbit stay constant.
A dependency of similar size on the integrator length is observable (cf. Fig. E.3). For CNGS beam with $\approx 10\,\mu$s long batches the systematic dependency should be

much smaller.
Especially the extraction interlock relies on a good performance of the acquisition system around the extraction times.

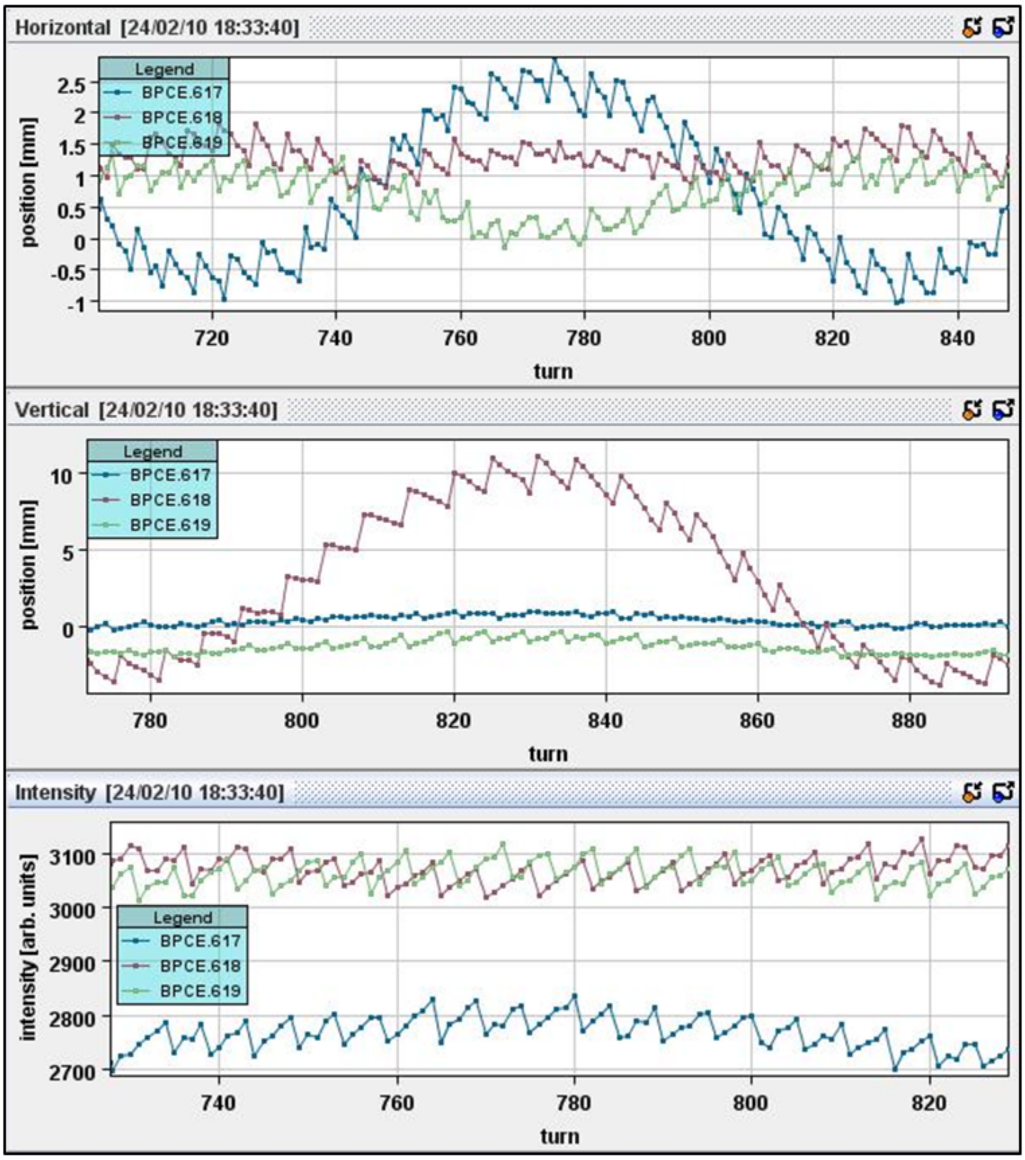

Figure E.1.: The fine structure of the 400 Hz oscillation shows a superimposed 8 kHz sawtooth oscillation.
Measurement conditions: cycle: LHCFAST2, beam energy: 450 GeV, bunch intensity: $1.3 \cdot 10^{11}$ protons, single bunch.

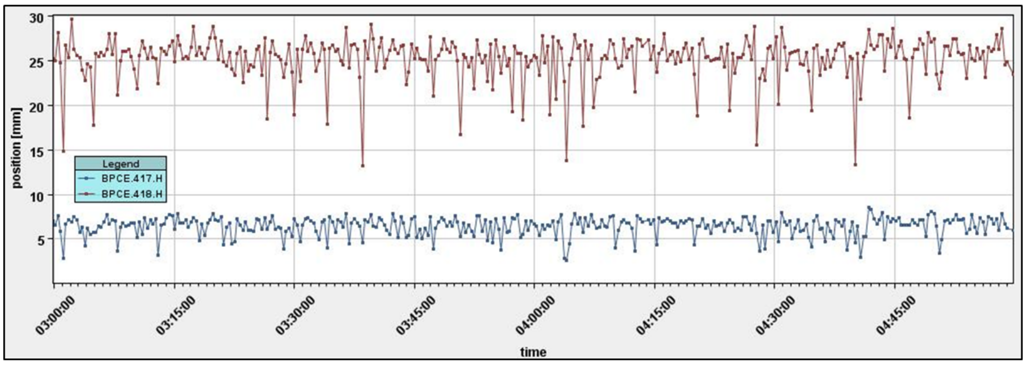

Figure E.2.: Average position measurement for the horizontal position of BPCE.416 and BPCE.417. The origin for the excursions are outliers in the turn-by-turn position measurement.
Measurement conditions: cycle: LHCFAST1, beam energy: 450 GeV, bunch intensity: $\approx 10^9 - 10^{10}$ protons, single bunch.

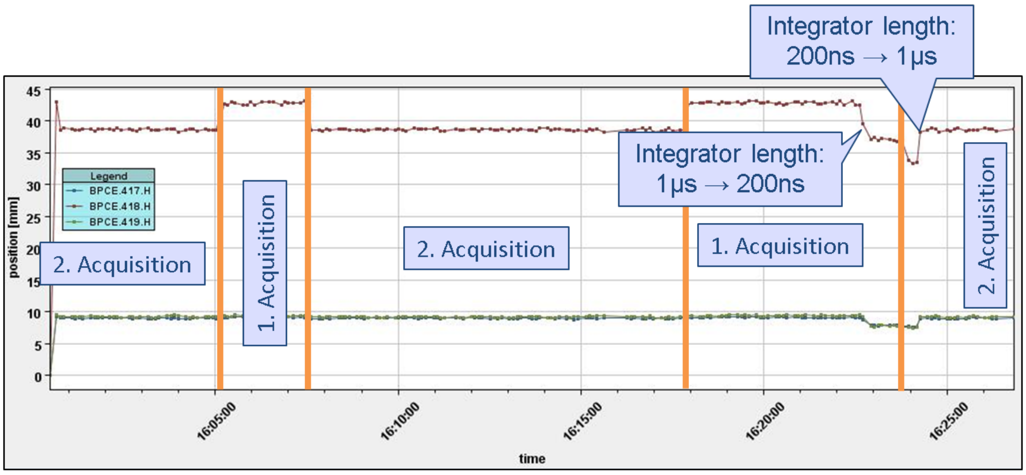

Figure E.3.: The measured position by BPCE.418.H before the extraction of the first batch (1. Acquisition) and after the extraction (2. Acquisition) differs by about 5 mm. Also a change of the integrator length affects the measurement.
Measurement conditions: cycle: CNGS2, beam energy: 400 GeV, bunch intensity: $3 - 6 \cdot 10^{10}$ protons, ≈ 400 bunches $\times$ 2.

E.4. H/V Correlation of BPCE.618

For BPCE.618 the vertical position measurement is correlated to the horizontal position measurement. Tests with different amplitudes of the horizontal LSS6 extraction bump show that about 15 % of the absolute value of the bump amplitude are measured in the vertical plane (cf. Fig. E.4 and Appendix F).
The BPM also measures large offsets of ≈ 8 mm in the vertical beam position that are not physical.
Both effects are not observed for high intensity CNGS-type beam at low energies and for no other BPM in LSS4 or LSS6. The correct cabling was confirmed during an additional inspection. Further tests to separate intensity, energy and cycle dependency are recommended.

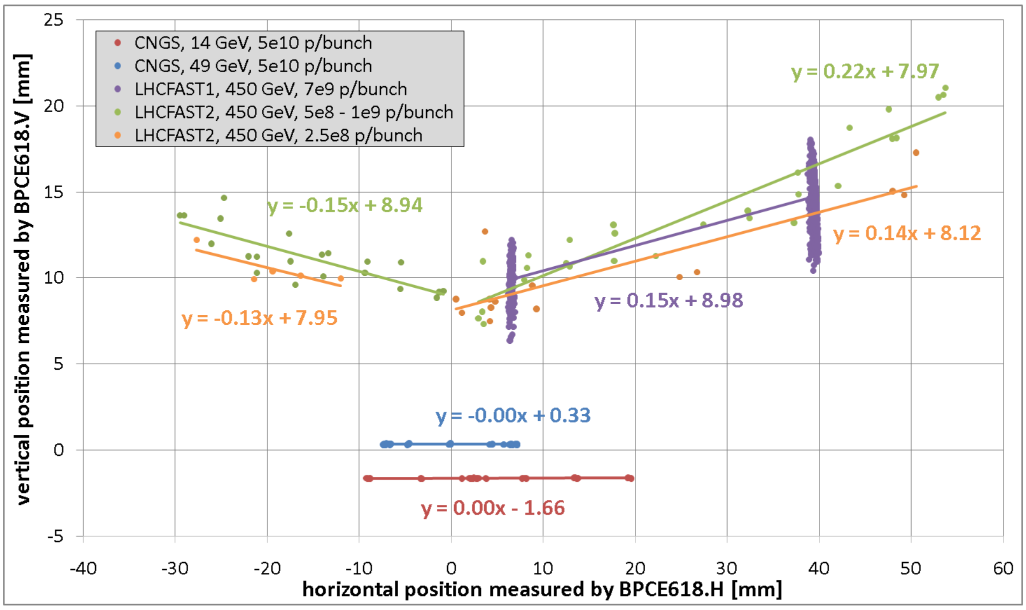

Figure E.4.: Horizontal and vertical position measured by BPCE.618. The amplitude of the horizontal extraction bump is changed. The measured vertical position is significantly correlated to the horizontal position. The correlation is not measured for high intensity CNGS beams.
Cf. legend for measurement conditions.

E.5. Intensity Dependency

A dependency of the measured positions on the bunch intensity is observable. Figure E.5 depicts the intensity dependency for the horizontal BPMs in LSS6 for low bunch intensities ($<5 \cdot 10^9$ protons). To make the measurements for different amplitudes of the horizontal extraction bump comparable, the values are normalized:

the linearly extrapolated values at zero intensity are chosen as reference. The bunch intensity is modified by a horizontal and/or vertical scraping of the beam.
In the measured intensity range, the measured beam position changes by up to $\approx 50\,\%$ due to the intensity change (cf. Fig. E.5c). A simple extrapolation to high intensities is not possible, since the (linear) fits do not provide a satisfactory description of the intensity dependency. The slope decreases significantly at bunch intensities above $\approx 2.5 \cdot 10^9$ protons. Further tests with a larger intensity range are highly recommended.
This test was done without the -16 db signal attenuators installed.

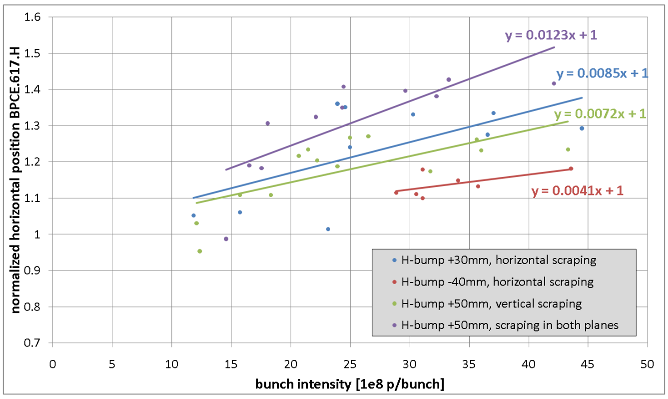

(a) BPCE.617.H

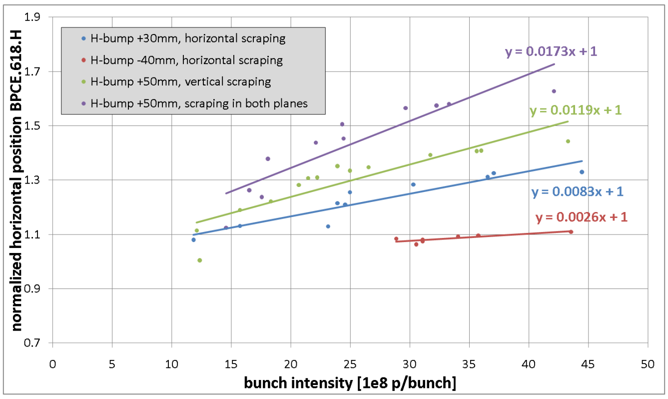

(b) BPCE.618.H

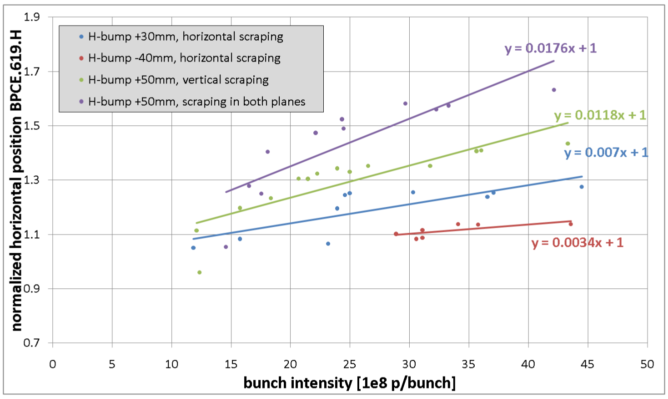

(c) BPCE.619.H

Figure E.5.: Intensity dependency of the horizontal BPMs in LSS6 for different amplitudes of the extraction bump. The positions are normalized to the linearly extrapolated positions at zero intensity.
Measurement conditions: cycle: LHCFAST2, beam energy: 450 GeV, bunch intensity: $1 - 5 \cdot 10^9$ protons, single bunch.

F. SPS BPCE LSS6 Test Sheet

Short Description:	Test of BPCE.617, BPCE.618, BPCE.619
Date:	07.11.2009
Responsible:	T. Baer, J. Wenninger

Test Conditions

Cycle:	3xCNGS1
Cycle time:	0 ms and 1740 ms after injection
Beam intensity:	$2 \cdot 10^{13} - 4 \cdot 10^{13}$ protons
Beam energy:	14 GeV and 49 GeV, respectively

Test description

After a previous test of the LSS6 Interlock BPCEs with low intensity ($\leq 1 \cdot 10^9$ protons), high energy beam (450 GeV) (LHCFAST2, 15.10.2009), this time, especially the position published by the BPMINT FESA class is tested with high intensity beam ($2 \cdot 10^{13} - 4 \cdot 10^{13}$ protons) and at beam energies of 14 GeV and 49 GeV.

Correlation of Horizontal and Vertical Measurement

In the previous test, a coupling between the vertical position measurement and the horizontal position measurement of about $\approx 15\,\% - 20\,\%$ was observed for BPCE.618. In the current test for all BPCEs in LSS6, the correlation between horizontal and vertical measurement is investigated for horizontal and vertical orbit bumps at beam energies of 14 GeV and 49 GeV, corresponding to beam intensities of $2 \cdot 10^{13}$ and $4 \cdot 10^{13}$ protons respectively. **In no case is a significant coupling of horizontal and vertical position measurement observable for CNGS-type beam.** Figure F.1 shows the coupling measured for BPCE.618 with horizontal orbit bumps of different amplitudes and the data measured during the previous test.

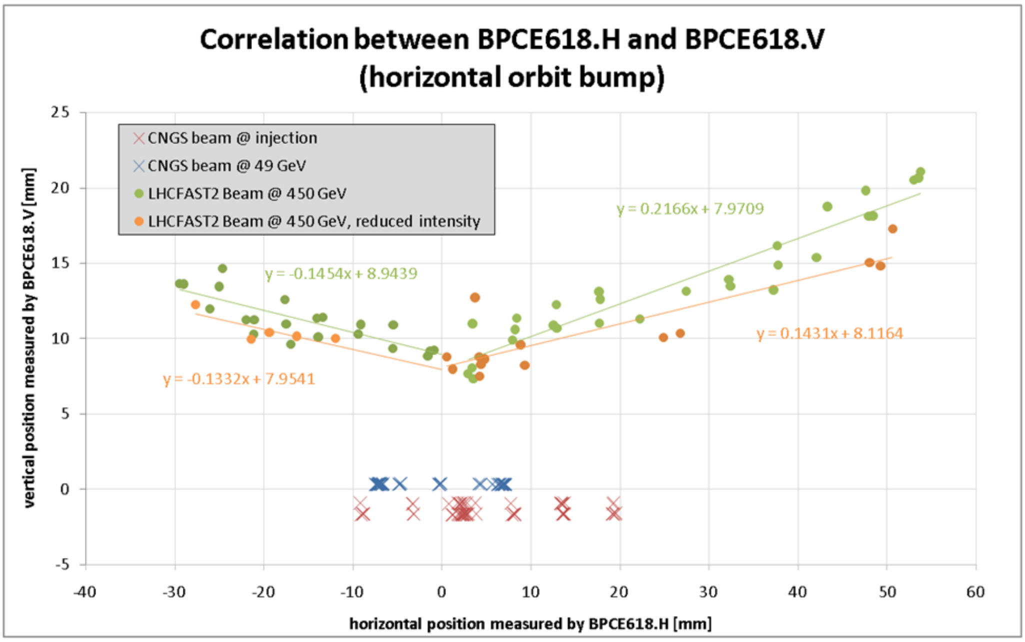

Figure F.1.: Correlation of vertical and horizontal position published by new BPMINT FESA class for BPCE.618. The data is measured for different horizontal orbit bumps with different amplitudes. There is a slight systematic position difference between the three CNGS cycles. The coupling observed with LHCFAST2 is not present with CNGS beam. Beam intensities: CNGS @ injection: $2 \cdot 10^{13}$ p; CNGS @ 49 GeV: $4 \cdot 10^{13}$ p; LHCFAST2: $0.5 - 1 \cdot 10^{9}$ p; LHCFAST2 reduced intensity: $0.25 \cdot 10^{9}$ p.

Comparison of new Hardware Data Processing and MOPOS Data

The data published by the BPMINT FESA class is processed by a different hardware than the traditional MOPOS data (used for example by YASP). During the previous test, large offsets ($> 10\,\text{mm}$) and extensive linear discrepancies ($< -30\,\%$) were observed. For CNGS-type beam, all offsets between new hardware and MOPOS processed data are smaller than $\approx 1\,\text{mm}$. Albeit, also for CNGS beam, **extensive linear discrepancies are observed for BPCE.617.H ($\approx +30\,\%$), BPCE.618.V ($\approx -40\,\%$) and BPCE.619.H ($\approx -30\,\%$).** In Figs. F.2 - F.7, the data processed by the new hardware and the MOPOS data is compared.

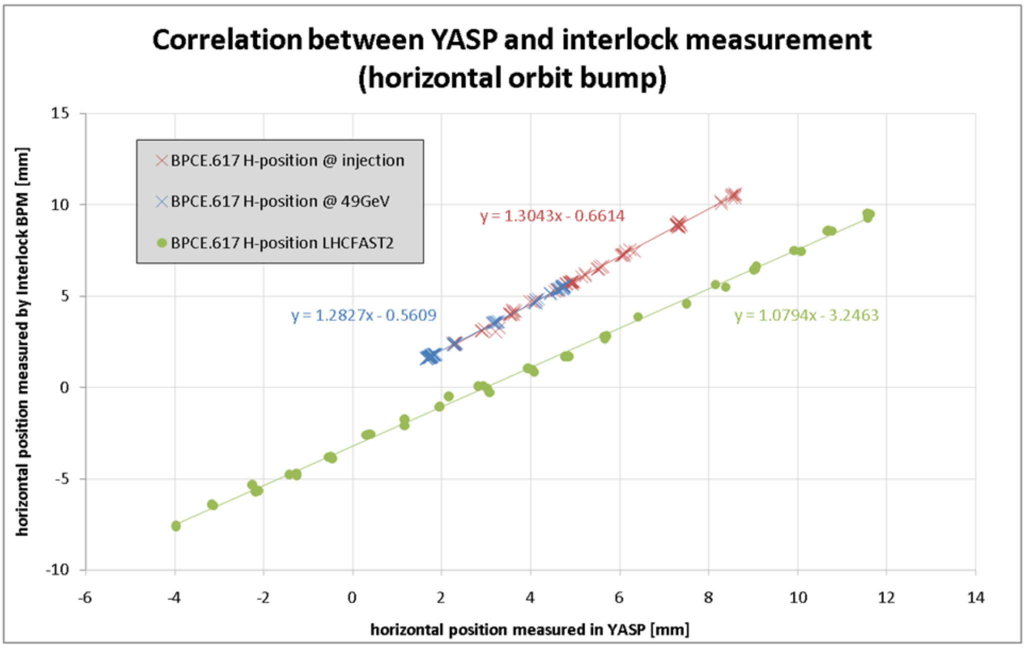

Figure F.2.: Correlation of horizontal position processed by MOPOS (YASP) and new hardware (interlock) for BPCE.617. The data is measured for different horizontal orbit bumps with different amplitudes.
Beam intensities, MOPOS gains: CNGS @ injection: $2 \cdot 10^{13}$ p, 30 db; CNGS @ 49 GeV: $4 \cdot 10^{13}$ p, 20 db, LHCFAST2: $0.5 - 1 \cdot 10^{9}$ p.

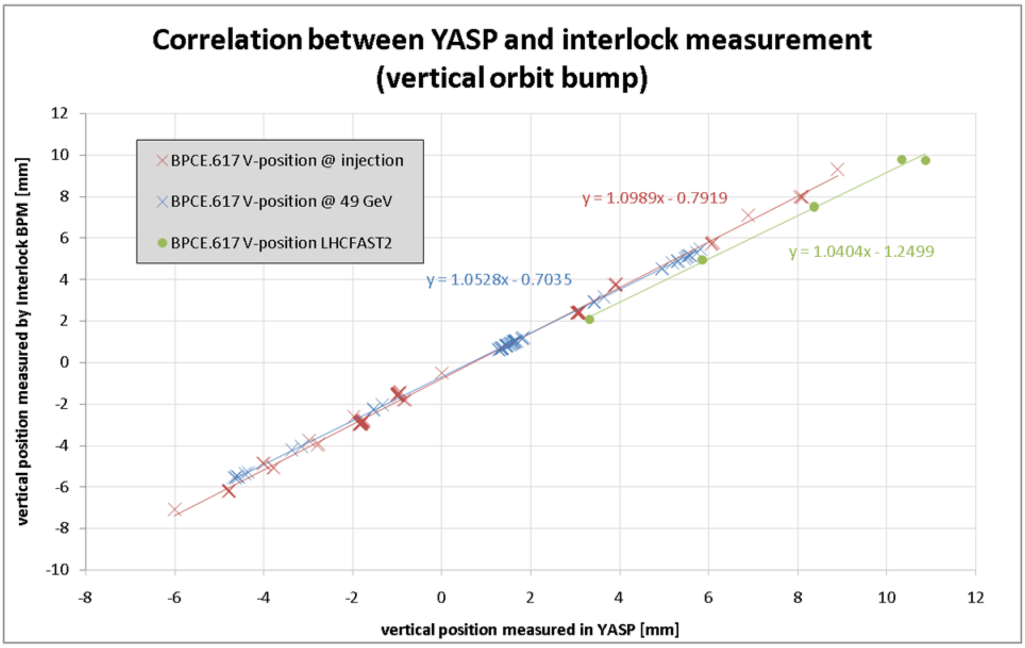

Figure F.3.: Correlation of vertical position processed by MOPOS (YASP) and new hardware (interlock) for BPCE.617. The data is measured for different vertical orbit bumps with different amplitudes.
Beam intensities, MOPOS gains: CNGS @ injection: $2 \cdot 10^{13}$ p, 30 db; CNGS @ 49 GeV: $4 \cdot 10^{13}$ p, 20 db, LHCFAST2: $0.5 - 1 \cdot 10^{9}$ p.

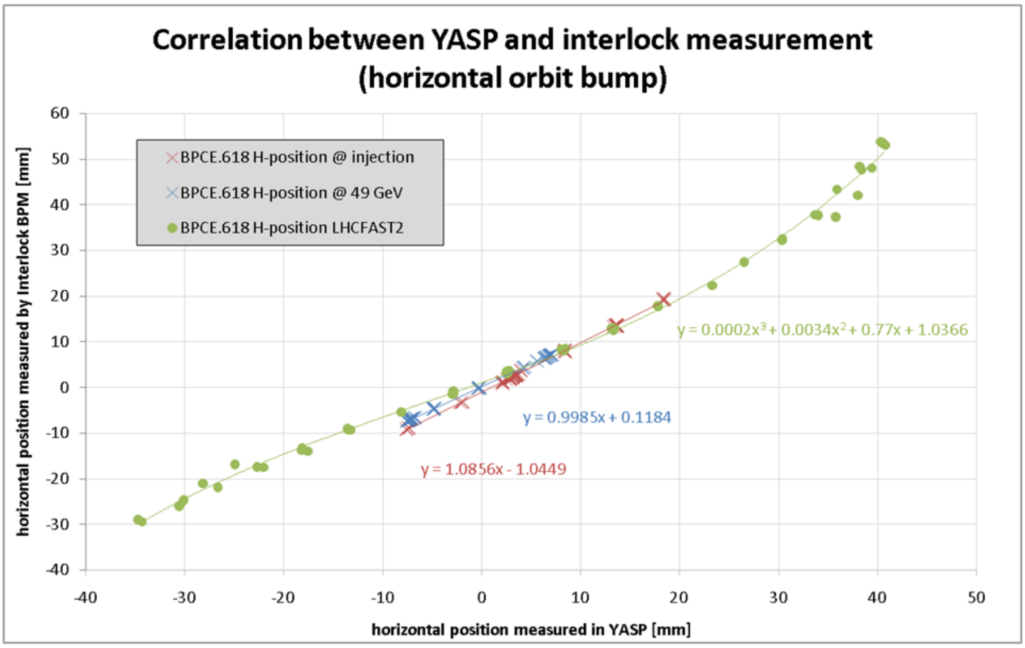

Figure F.4.: Correlation of horizontal position processed by MOPOS (YASP) and new hardware (interlock) for BPCE.618. The data is measured for different horizontal orbit bumps with different amplitudes.
Beam intensities, MOPOS gains: CNGS @ injection: $2 \cdot 10^{13}$ p, 30 db; CNGS @ 49 GeV: $4 \cdot 10^{13}$ p, 20 db, LHCFAST2: $0.5 - 1 \cdot 10^{9}$ p.

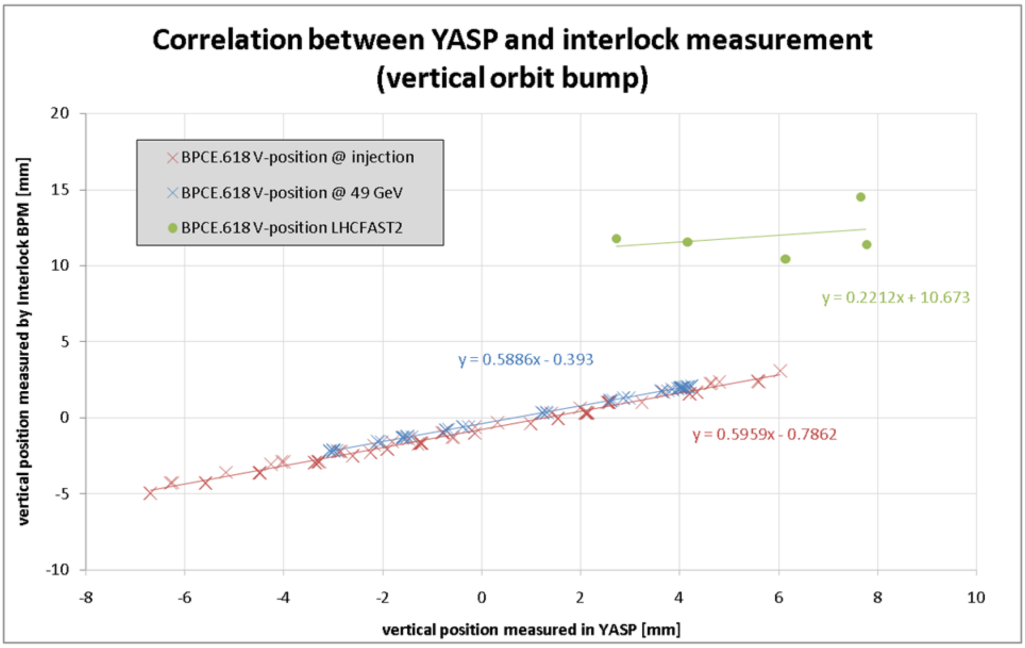

Figure F.5.: Correlation of vertical position processed by MOPOS (YASP) and new hardware (interlock) for BPCE.618. The data is measured for different vertical orbit bumps with different amplitudes.
Beam intensities, MOPOS gains: CNGS @ injection: $2 \cdot 10^{13}$ p, 30 db; CNGS @ 49 GeV: $4 \cdot 10^{13}$ p, 20 db, LHCFAST2: $0.5 - 1 \cdot 10^{9}$ p.

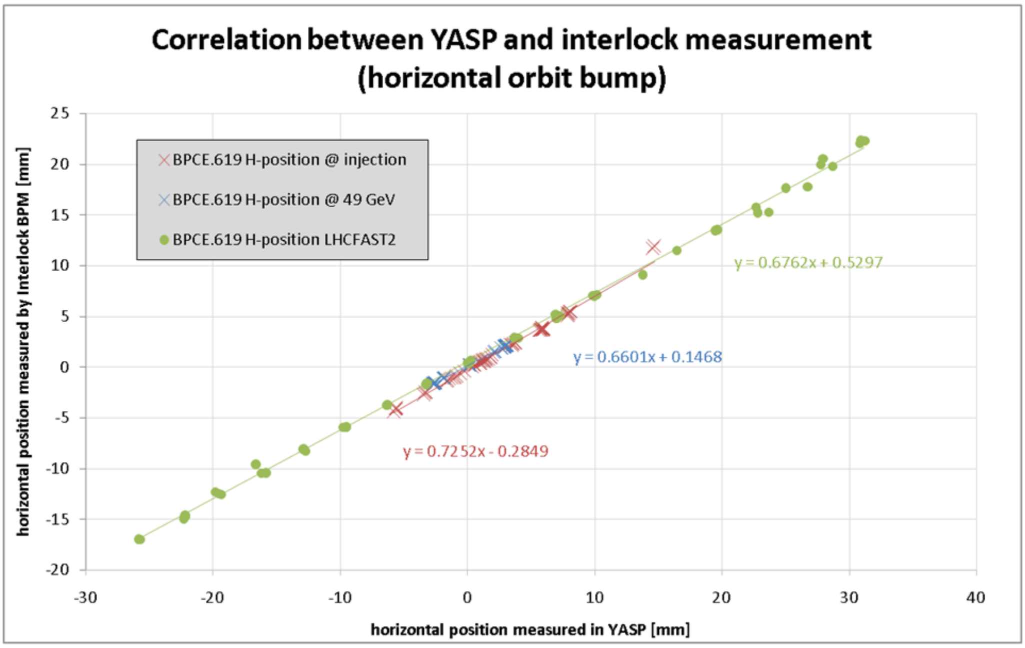

Figure F.6.: Correlation of horizontal position processed by MOPOS (YASP) and new hardware (interlock) for BPCE.619. The data is measured for different horizontal orbit bumps with different amplitudes.
Beam intensities, MOPOS gains: CNGS @ injection: $2 \cdot 10^{13}$ p, 30 db; CNGS @ 49 GeV: $4 \cdot 10^{13}$ p, 20 db, LHCFAST2: $0.5 - 1 \cdot 10^{9}$ p.

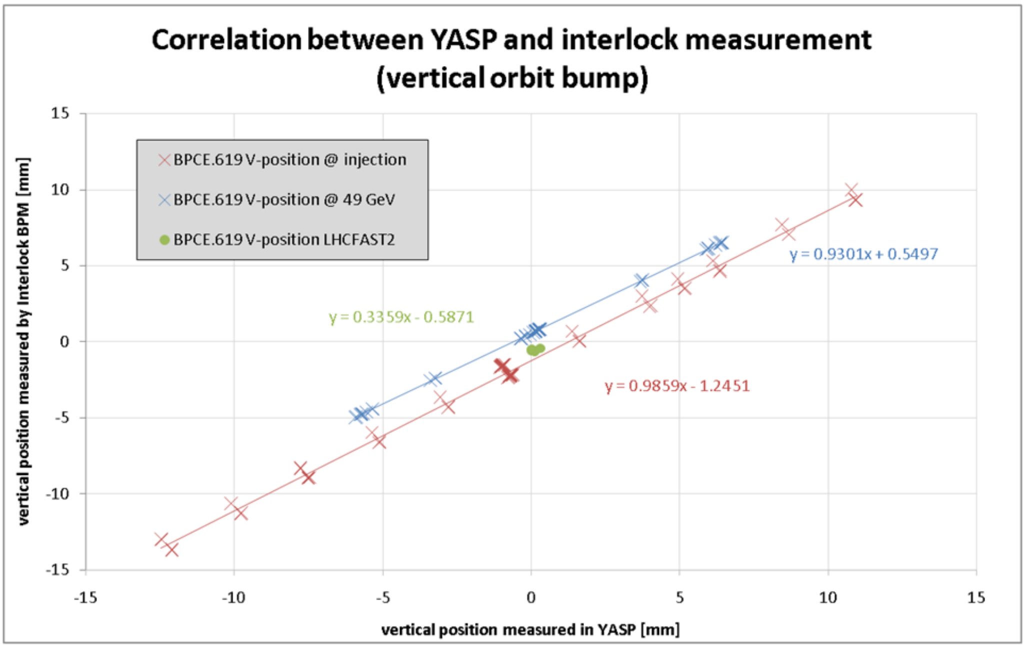

Figure F.7.: Correlation of vertical position processed by MOPOS (YASP) and new hardware (interlock) for BPCE.619. The data is measured for different vertical orbit bumps with different amplitudes.
Beam intensities, MOPOS gains: CNGS @ injection: $2 \cdot 10^{13}$ p, 30 db; CNGS @ 49 GeV: $4 \cdot 10^{13}$ p, 20 db, LHCFAST2: $0.5 - 1 \cdot 10^{9}$ p.

Erklärung

Hiermit versichere ich, dass ich diese Arbeit selbstständig und unter ausschließlicher Verwendung der angegebenen Quellen angefertigt habe.

Genf, den 29. Juli 2010

Tobias Baer

Ich erkläre mich mit der Veröffentlichung dieser Diplomarbeit einverstanden.